Seismic full-waveform inversion of the crust-mantle structure beneath China and adjacent regions

Jincheng Ma

München 2023

Seismic full-waveform inversion of the crust-mantle structure beneath China and adjacent regions

Jincheng Ma

Dissertation zur Erlangung des Doktorgrades
an der Fakultät für Geowissenschaften
der Ludwig-Maximilians-Universität München

vorgelegt von
Jincheng Ma
aus Shangqiu (V.R. China)

München, den 30 Oktober 2022

Erstgutachter: Prof. Dr. Hans-Peter Bunge
Zweitgutachter: Prof. Dr. Andreas Fichtner
Tag der mündlichen Prüfung: 22.02.2023

Der Meister sprach: »In der Frühe die Wahrheit vernehmen
und des Abends sterben: das ist nicht schlimm.«

[Kung-Futse: Gespräche (Lun Yü),
Aus dem Chinesischen von Richard Wilhelm, 1910]

Noch schlimmer sind wir dran in der Geologie, die ihrer Natur nach sich hauptsächlich mit Vorgängen beschäftigt, bei denen nicht nur nicht wir, sondern überhaupt kein Mensch dabei gewesen ist. Die Ausbeute an endgültigen Wahrheiten letzter Instanz ist daher hier mit sehr vieler Mühe verknüpft und dabei äußerst sparsam.

[F. Engels, Anti-Dühring, 1878]

Contents

List of Figures

Summary

Since the late 1970s, seismic tomography has been emerging as the pre-eminent tool for imaging the Earth's interior from the meter to the global scale. Significant recent advances in seismic data acquisition, high-performance computing, and modern numerical methods have drastically progressed tomographic methods. Today it is technically feasible to accurately simulate seismic wave propagation through realistically heterogeneous Earth models across a range of scales. When seismic waves propagate inside the Earth and encounter structural heterogeneities with a certain scale, wave propagation speed changes, reflection, and scattering phenomena occur, and interconversions between compressional and shear waves happen. The combined effect of multiple heterogeneities produces a highly complicated wavefield recorded in the form of three-component (vertical, radial, transverse) seismograms. The ultimate objective of seismic imaging is to utilize the full information from waveforms recorded at seismic stations distributed around the globe in a broad frequency range to characterize detailed tomographic images of Earth's interior by fitting synthetic seismograms to recorded seismograms. The full-waveform inversion technique based on adjoint and spectral-element methods can be employed to maximumly exploit the information contained in these seismic wavefield complexities to determine the fine-scale structural heterogeneities from which they originated across various orders of magnitude in frequency and wavelength.

Over the past two decades, the three-dimensional crust and mantle structure beneath the broad Asian region has attracted much attention in seismic studies due to its complicated and unique geological setting involving active lithospheric deformation, intracontinental rifting, intraplate seismotectonics, volcanism and magmatism, continent-continent collision, oceanic plate deep subduction, and mantle dynamics. To enhance our understanding of the subsurface behavior of cold subducting slabs and hot mantle flows and their dynamic relation to the tectonic evolution of the overriding plates as mentioned above, we construct the first-generation full-waveform tomographic model (***SinoScope 1.0***) for the crust-mantle structure beneath China and adjacent regions. The three-component seismograms from 410 earthquakes recorded at 2,427 seismographic stations are employed in iterative gradient-based inversions for three successively broadened period bands of 70 - 120 s, 50 - 120 s, and 30 - 120 s. Synthetic seismograms were computed using GPU-accelerated spectral-element simulations of seismic wave propagation in 3-D anelastic models, and Fréchet derivatives were calculated based on an adjoint-state method facilitated by a checkpointing algorithm. The inversion involved 352 iterations, which required 18,600 wavefield

simulations. The simulations were performed on the Xeon Platinum 'SuperMUC-NG' at the Leibniz Supercomputing Center and the Xeon E5 'Piz Daint' at the Swiss National Supercomputing Center with a total cost of ∼8 million CPU hours. ***SinoScope 1.0*** is described in terms of isotropic P-wave velocity (V_P), horizontally and vertically polarized S-wave velocities (V_{SH} and V_{SV}), and mass density (ρ) variations, which are independently constrained with the same data set coupled with a stochastic L-BFGS quasi-Newton optimization scheme. It systematically reduced differences between observed and synthetic full-length seismograms. We performed a detailed resolution analysis by repairing input random parametric perturbations, indicating that resolution lengths can approach the half-propagated wavelength within the well-covered areas.

SinoScope 1.0 exhibits strong lateral heterogeneities in the crust and uppermost mantle, and features correlate well with geological observations, such as sedimentary basins, Holocene volcanoes, Tibetan Plateau, Philippine Sea Plate, orogenic belts, and subduction zones. Estimating lithospheric thickness from seismic velocity reductions at depth reveals significant variations underneath the different tectonic units: ∼50 km in Northeast and North China, ∼70 km in South China, ∼90 km in the South China Sea, Philippine Sea Plate, and Caroline Plate, and 150-250 km in the Indian Plate. The thickest (200-250 km) cratonic roots are present beneath the Sichuan, Ordos, and Tarim basins. The large-scale lithospheric deformation is imaged as low-velocity zones from the Himalayan orogen to the Baikal rift system in central Asia. A thin horizontal layer of ∼100-200 km depth extent below the lithosphere points toward the existence of the asthenosphere beneath East and Southeast Asia, with heterogeneous anisotropy indicative of channel flows. This provides independent, high-resolution evidence for the low-viscosity asthenosphere that partially decouples plates from mantle flow beneath and allows plate tectonics to work above. Beneath the Indo-Australian Plate, we observe distinct low-velocity anomalies from a depth of ∼200 km to the bottom of the mantle transition zone (MTZ), continuously extending northward below western China from the lower MTZ down to the top of the lower mantle. Furthermore, we observe an enhanced image of well-known slabs along strongly curved subduction zones, including Kurile, Japan, Izu-Bonin, Mariana, Ryukyu, Philippines, Indonesia, and Burma. Broad high-velocity bodies persist from the lower MTZ to 1000 km depth or deeper beneath the north of the Indo-Australian Plate. They might be pieces of the ancient Tethyan slab sinking down to the lower mantle before the Indo-Australian Plate and Eurasian Plate collision.

The deep geodynamic processes controlling the large-scale tectonic activity of the broad Asian region are very complicated and not yet well understood, which is a source of much debate. In this thesis, the main focus is on deciphering the three-dimensional seismic structure and dynamics of the lithosphere and mantle beneath China and adjacent regions with the help of the high-resolution full-waveform tomographic model. More importantly, in the subsequent works of geodynamic inversion, it provides the improved seismological basis for a sequential reconstruction of the late Mesozoic and Cenozoic plate motion history of the broad Asian region and the present-day mantle heterogeneity state estimates that, in turn, allow one to track material back in time from any given sampling location through retrodicting past mantle states.

Chapter 1

Introduction

Once a seismic event, such as a natural earthquake or a seismic explosion, takes place, seismic waves are excited, which propagate through the Earth's interior and finally reach the Earth's surface, where they are recorded by seismometers installed at seismic stations in different parts of the world. Seismic waves carry rich information about the Earth's interior structure. By analyzing the observed three-component seismograms, seismologists can obtain information on the causal mechanism of earthquakes and the physical properties of materials along the trajectories of the seismic waves. Large parts of our current knowledge of Earth's deep interior come mainly from seismological investigations. The first-order features of the Earth were established in the first half of the 20th century: Oldham (1906) correctly inferred the existence of the Earth's outer core, the radius of which was accurately determined by Gutenberg (1913), and later Lehmann (1936) discovered the solid inner core; Zoeppritz (1907) compiled accurate traveltime tables and assembled them into one-dimensional models of the Earth's mantle; Mohorovičić (1910) studied regional earthquakes and discovered the interface between crust and mantle – the Mohorovičić discontinuity. In the following decades, complete radially symmetric Earth models have been continually refined, starting with the famous travel timetables by Jeffreys and Bullen (1940) and the associated velocity model (Dziewonski and Anderson, 1981; Kennett and Engdahl, 1991; Kennett et al., 1995), which has had far-reaching and profound impacts on building global three-dimensional (3-D) Earth models.

In the early 1970s, the discovery of the laterally heterogeneous nature of the Earth's interior led to a new generation of three-dimensional Earth models motivated by a new field of seismology - seismic tomography (Aki and Lee, 1976; Aki et al., 1977; Dziewonski et al., 1977). Benefiting from increasing computer power and greater quality and quantity of seismic data, the significant improvement in the resolution of tomographic images enabled the link with mantle convection models (e.g., Van der Hilst et al., 1997; Ritsema and Van Heijst, 2000; Bunge and Grand, 2000) and the tectonic evolution of continents (e.g., Zielhuis and Nolet, 1994; Zielhuis and van der Hilst, 1996). Most seismological inferences about the structure of the Earth are based on the infinite-frequency assumption of seismic wave propagation, as described by infinitely thin rays (ray theory). Although the intensive use of ray theory (e.g., Červený, 2001) primarily stems from its simplicity

and intuitive interpretation, in the late 90s, ray theory in the context of seismic tomography had reached its limitations. The fact that ray theory is only valid when the length scales of 3-D heterogeneities are small compared to the dominant wavelength imposed an upper limit on the resolution of tomographic images. Efforts to improve the resolution of tomographic images include wave equation-based full-waveform tomography (e.g., Bamberger et al., 1982; Tarantola, 1988; Igel et al., 1996) and Fresnel-zone finite-frequency tomography (e.g., Yomogida, 1992; Dahlen et al., 2000). Finite-frequency tomography is an improvement of ray-based tomography using the Born approximation for accounting for the finite frequency effect of the sensitivity of seismic waves to Earth structure. Despite its advantages over traditional ray-based traveltime tomography, this approach still has limitations (e.g., it does not take into account the full physics of the wave equation. Full waveform inversion goes beyond the previously mentioned tomographic methods in terms of physical rigorousness: replace semi-analytical solutions to the wave equation with fully numerical solutions, accurately account for 3-D heterogeneous Earth structure, and iterate a non-linear optimization scheme to minimize the misfit between synthetic and observed waveforms.

No place on Earth displays more diverse and more complex patterns of tectonic configurations than Asia. The broad Asian region thus provides a natural laboratory for testing and validating major geological and geophysical hypotheses regarding continental convergence, oceanic subduction, intracontinental deformation, intraplate volcanism and magmatism, and the interactions among them. Consequently, the crust and mantle structure in the Asian region has attracted much attention in seismic studies due to its complicated and unique geological setting in the past two decades. The large-scale mantle structure is now well agreed upon; however, the fine-scale 3-D structure of the crust and mantle beneath China and adjacent regions has not been well established because of the limitations in the methodology, seismic observation data, and computer powers then available. In the past two decades, the dense deployment of temporary and permanent broadband seismic stations in mainland China and adjacent regions (e.g., ChinArray project, China Digital Seismic Network, Korea National Seismograph Network, F-net Broadband Seismograph Network), and theoretical progress in wave-propagation and tomography together with a rise in computational power provide notable advantages to construct a reference seismic model (***SinoScope 1.0***) of the crust-mantle structure beneath the broad Asian region using the state-of-the-art full-waveform inversion method. ***SinoScope 1.0*** will be employed to estimate the present-day mantle heterogeneity state to retrodict the history of mantle flow and dynamic topography in the subsequent works through the adjoint method introduced by Bunge et al. (2003), building upon our previous works presented by Colli et al. (2018) and Ghelichkhan et al. (2021).

In chapter 2, we present the first-generation full-waveform tomographic model (***SinoScope 1.0***) for the crust-mantle structure beneath China and adjacent regions. The three-component seismograms from 410 earthquakes recorded at 2,427 stations are employed in iterative gradient-based inversions for three successively broadened period bands of 70–120 s, 50–120 s, and 30–120 s. Synthetic seismograms were computed using GPU-accelerated spectral-element simulations of seismic wave propagation in 3-D anelastic models, and

Fréchet derivatives were calculated based on an adjoint-state method facilitated by a checkpointing algorithm. The inversion involved 352 iterations, which required 18,600 wavefield simulations. We performed a detailed resolution analysis by repairing input random parametric perturbations, indicating that resolution lengths can approach the half-propagated wavelength within the well-covered areas. SinoScope 1.0 reveals strong lateral heterogeneities in the lithosphere, and features correlate well with geological observations, such as sedimentary basins, Holocene volcanoes, Tibetan Plateau, Philippine Sea Plate, and various tectonic units. The asthenosphere lies below the lithosphere beneath East and Southeast Asia, bounded by subduction trenches and cratonic blocks. Furthermore, we observe an enhanced image of well-known slabs along strongly curved subduction zones, which do not exist in the initial model.

In chapter 3, we discuss the structure and dynamics of the lithosphere and asthenosphere in Asia from a seismological perspective. Estimating lithospheric thickness from seismic velocity reductions at depth reveals large variations underneath various geological units and cratonic blocks. The thickest cratonic roots are present beneath Sichuan, Ordos, and Tarim basins and central India. The radial anisotropy signatures of eleven representative tectonic provinces uncover the different nature and geodynamic processes of their respective past and present deformation. The large-scale continental lithospheric deformation is characterized by low-velocity zones from the Himalayan Orogen to the Baikal rift zone in central Asia, coupled with the post-collision thickening of the crust. The horizontal low-velocity layer of ∼100-300 km depth extent below the lithosphere points toward the existence of the asthenosphere beneath East and Southeast Asia, with heterogeneous anisotropy indicative of channel flows.

Reference

Aki, K., Christoffersson, A. and Husebye, E. S. (1977). Determination of the three-dimensional seismic structure of the lithosphere, *Journal of Geophysical Research* **82**(2): 277–296.

Aki, K. and Lee, W. (1976). Determination of three-dimensional velocity anomalies under a seismic array using first p arrival times from local earthquakes: 1. a homogeneous initial model, *Journal of Geophysical research* **81**(23): 4381–4399.

Bamberger, A., Chavent, G., Hemon, C. and Lailly, P. (1982). Inversion of normal incidence seismograms, *Geophysics* **47**(5): 757–770.

Bunge, H.-P. and Grand, S. P. (2000). Mesozoic plate-motion history below the northeast pacific ocean from seismic images of the subducted farallon slab, *Nature* **405**(6784): 337–340.

Bunge, H.-P., Hagelberg, C. and Travis, B. (2003). Mantle circulation models with variational data assimilation: inferring past mantle flow and structure from plate motion histories and seismic tomography, *Geophysical Journal International* **152**(2): 280–301.

Colli, L., Ghelichkhan, S., Bunge, H.-P. and Oeser, J. (2018). Retrodictions of mid paleogene mantle flow and dynamic topography in the atlantic region from compressible high resolution adjoint mantle convection models: Sensitivity to deep mantle viscosity and tomographic input model, *Gondwana Research* **53**: 252–272.

Dahlen, F., Hung, S.-H. and Nolet, G. (2000). Fréchet kernels for finite-frequency traveltimes—i. theory, *Geophysical Journal International* **141**(1): 157–174.

Dziewonski, A. M. and Anderson, D. L. (1981). Preliminary reference earth model, *Physics of the earth and planetary interiors* **25**(4): 297–356.

Dziewonski, A. M., Hager, B. H. and O'Connell, R. J. (1977). Large-scale heterogeneities in the lower mantle, *Journal of Geophysical Research* **82**(2): 239–255.

Ghelichkhan, S., Bunge, H. and Oeser, J. (2021). Global mantle flow retrodictions for the early cenozoic using an adjoint method: evolving dynamic topographies, deep mantle structures, flow trajectories and sublithospheric stresses, *Geophysical Journal International* **226**(2): 1432–1460.

Gutenberg, B. (1913). Uber die konstitution des erdinnern, erschlossen aus erdbebenbeobachtungen, *Phys. Z* **14**: 1217–1218.

Igel, H., Djikpéssé, H. and Tarantola, A. (1996). Waveform inversion of marine reflection seismograms for p impedance and poisson's ratio, *Geophysical Journal International* **124**(2): 363–371.

Jeffreys, H. and Bullen, K. (1940). Seismological tables, british association for the advancement of science, london.

Kennett, B. and Engdahl, E. (1991). Traveltimes for global earthquake location and phase identification, *Geophysical Journal International* **105**(2): 429–465.

Kennett, B. L., Engdahl, E. and Buland, R. (1995). Constraints on seismic velocities in the earth from traveltimes, *Geophysical Journal International* **122**(1): 108–124.

Lehmann, I. (1936). P', *Bureau Central Sismologique International, Travaux Scientifiques* **14**: 87–115.

Mohorovičić, A. (1910). Das beben vom 8. oktober 1909, *Jahrbuch des meteorologischen Observatoriums in Zagreb für* **4**(1): 1–67.

Oldham, R. (1906). The constitution of the earth: Quarterly journal of the geological society of london.

Ritsema, J. and Van Heijst, H.-J. (2000). Seismic imaging of structural heterogeneity in earth's mantle: evidence for large-scale mantle flow, *Science Progress (1933-)* pp. 243–259.

Tarantola, A. (1988). Theoretical background for the inversion of seismic waveforms, including elasticity and attenuation, *Scattering and attenuations of seismic waves, part i*, Springer, pp. 365–399.

Van der Hilst, R. D., Widiyantoro, S. and Engdahl, E. (1997). Evidence for deep mantle circulation from global tomography, *Nature* **386**(6625): 578–584.

Yomogida, K. (1992). Fresnel zone inversion for lateral heterogeneities in the earth, *Pure and Applied Geophysics* **138**(3): 391–406.

Zielhuis, A. and Nolet, G. (1994). Shear-wave velocity variations in the upper mantle beneath central europe, *Geophysical Journal International* **117**(3): 695–715.

Zielhuis, A. and van der Hilst, R. D. (1996). Upper-mantle shear velocity beneath eastern australia from inversion of waveforms from skippy portable arrays, *Geophysical Journal International* **127**(1): 1–16.

Zoeppritz, K. (1907). Über erdbebenwellen ii, *Laufzeitkurven. Nachrichten der Königlichen Gesellschaft der Wissenschaften zu Göttingen, Mathematisch-physikalische Klasse* pp. 529–549.

Červený, V. (2001). Seismic ray theory, cambridge university press, cambridge,(2001).

Chapter 2

Seismic full-waveform inversion of the crust-mantle structure beneath China and adjacent regions

This chapter was published as a paper entitled "Seismic full-waveform inversion of the crust-mantle structure beneath China and adjacent regions" in *Journal of Geophysical Research: Solid Earth*, 2022, https://doi.org/10.1029/2022JB024957

Seismic full-waveform inversion of the crust-mantle structure beneath China and adjacent regions

Jincheng Ma[1†], Hans-Peter Bunge[1], Solvi Thrastarson[2], Andreas Fichtner[2], Dirk-Philip van Herwaarden[2], You Tian[4], Sung-Joon Chang[4], and Tingting Liu[5]

[1] Department of Earth and Environmental Sciences, Ludwig-Maximilians-Universität München, Munich, Germany
[2] Department of Earth Sciences, ETH Zürich, Zurich, Switzerland
[3] College of Geoexploration Science and Technology, Jilin University, Changchun, China
[4] Department of Geophysics, Kangwon National University, Chuncheon, South Korea
[5] Geophysical Institute, Karlsruhe Institute of Technology (KIT), Karlsruhe, Germany

Key Points:

- We construct a new full-waveform tomographic model of the broad Asian region for 30-120 s period via adjoint and spectral-element methods
- The resolution analysis shows reasonably good resolution in the frequency band of interest and limited trade-offs between model parameters
- Our model shed new light on the subsurface behavior of cold subducting slabs & hot mantle flows and their relation to the overriding plates

2.1 Abstract

We present the first-generation full-waveform tomographic model (***SinoScope 1.0***) for the crust-mantle structure beneath China and adjacent regions. The three-component seismograms from 410 earthquakes recorded at 2,427 stations are employed in iterative gradient-based inversions for three successively broadened period bands of 70 - 120 s, 50 - 120 s, and 30 - 120 s. Synthetic seismograms were computed using GPU-accelerated spectral-element simulations of seismic wave propagation in 3-D anelastic models, and Fréchet derivatives were calculated based on an adjoint-state method facilitated by a check-pointing algorithm. The inversion involved 352 iterations, which required 18,600 wavefield simulations. ***SinoScope 1.0*** is described in terms of isotropic P-wave (V_P), horizontally and vertically polarized S-wave velocities (V_{SH} and V_{SV}), and mass density (ρ), which are independently constrained with the same data set coupled with a stochastic L-BFGS quasi-Newton optimization scheme. It systematically reduced differences between observed and

synthetic full-length seismograms. We performed a detailed resolution analysis by repairing input random parametric perturbations, indicating that resolution lengths can approach the half propagated wavelength within the well-covered areas. ***SinoScope 1.0*** reveals strong lateral heterogeneities in the lithosphere, and features correlate well with geological observations, such as sedimentary basins, Holocene volcanoes, Tibetan Plateau, Philippine Sea Plate, and various tectonic units. The asthenosphere lies below the lithosphere beneath East and Southeast Asia, bounded by subduction trenches and cratonic blocks. Furthermore, we observe an enhanced image of well-known slabs along strongly curved subduction zones, which does not exist in the initial model.

Plain Language Summary

Subduction (a geological process where the oceanic lithosphere descends into the Earth's mantle at convergent boundaries) has been the dominant plate-tectonic process in the broad Asian region since the Mesozoic (252-66 million years ago). The nature of cold subducting slabs and hot mantle flows can record and affect the tectonic evolution of the overriding lithospheric plates. In this study, we conduct the full waveform inversion on a large data set to image the crust-mantle structure of this region. The computationally demanding simulations were performed on two of the world's fastest supercomputing facilities. Our new model delivers seismic illumination of the region at unprecedented resolution and exhibits sharper and more detailed shear wave velocity structure in the lithosphere with greatly improved correlations with surface tectonic units compared to previous tomographic models. The narrow low-velocity layer (generally referred to as asthenosphere) below the lithosphere is present beneath East and Southeast Asia, bounded by subduction trenches and cratonic blocks. The continuous and intense subduction processes are responsible for high-velocity anomalous bodies in the mantle and the formation of the asthenosphere mentioned above.

2.2 Introduction

The late Mesozoic and Cenozoic plate tectonic evolution of the broad Asian region is associated with the northwestward subductions of the Pacific and Philippine Sea plates in the east and the collision and convergence of the Indo-Australian Plate with the Eurasian Plate along the Tethys tectonic belt in the southwest (e.g., Yin, 2010; Jolivet et al., 2018; Ma et al., 2020). The western Pacific Plate began to intersect the East Asian continental margin between 55 and 50 Ma, marked by the demise of the Izanagi Plate. It then started to subduct beneath the Okhotsk and Eurasian plates at a rate of ∼8-9 cm/yr along the Kuril and Japan trenches in the north and to descend beneath the Philippine Sea Plate at ∼6 cm/yr along the Izu-Bonin-Mariana Trench in the south (Figure 2.1; e.g., DeMets et al., 1994; Bird, 2003; Hayes et al., 2018). At ca. 20 Ma, it has been suggested that the northwestern margin of the Philippine Sea Plate could have collided with the continental

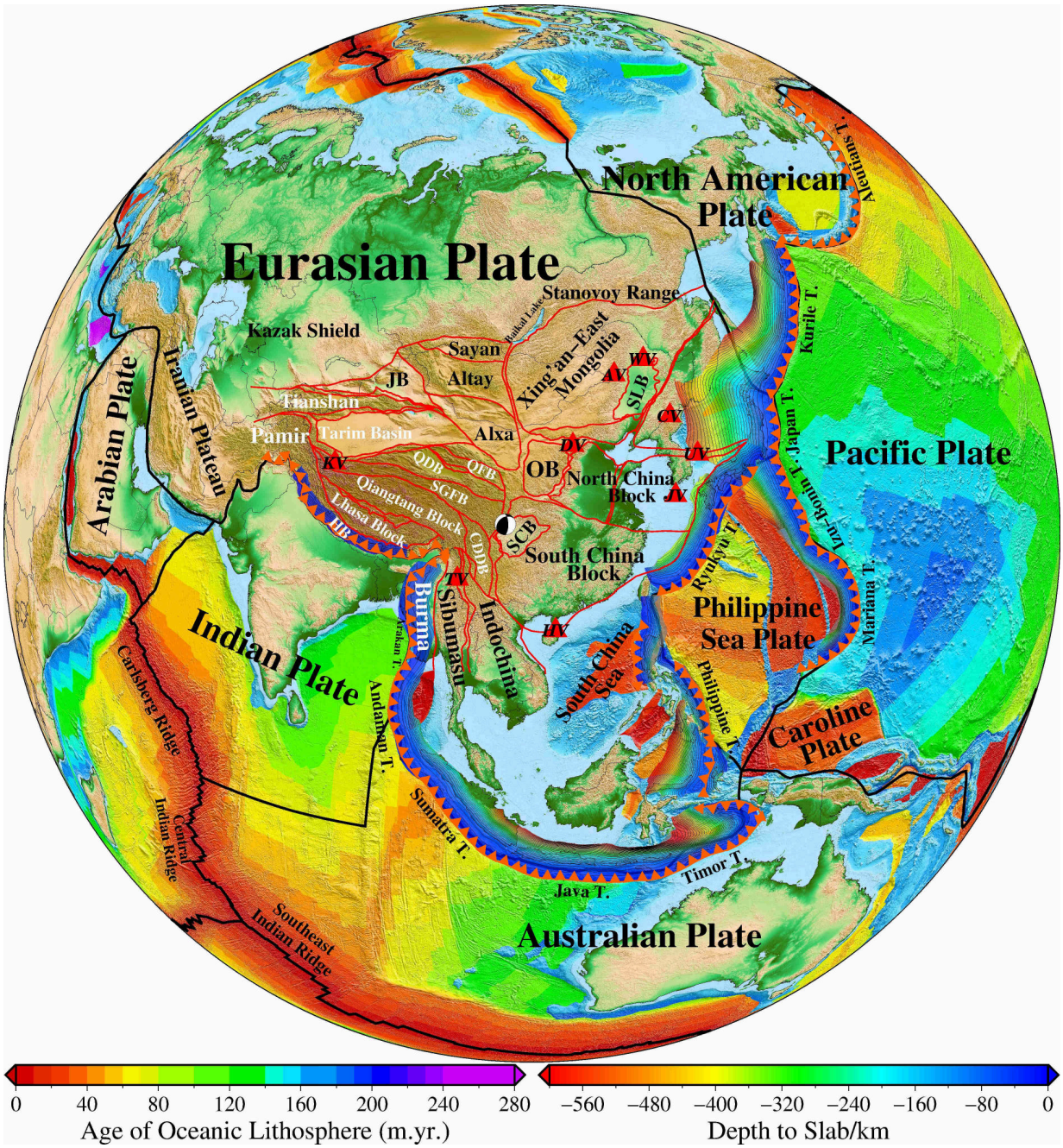

Figure 2.1: Map showing the surface topography and major tectonic features of the broad Asian region. The age-area distribution of the oceanic lithosphere (Seton et al., 2020) is shown in different colors; its scale is shown at the lower left corner below the map. The red triangles mark the active intraplate volcanoes. The red sawtooth lines show the subduction trenches where the oceanic plates are subducting into the mantle. The dark bold lines delineate the major plate boundaries (Bird, 2003), and the red lines define main tectonic units, basins, and large fault zones. The color contour lines show depths to the upper boundaries of the subducting slabs with an interval of ∼20 km (Hayes et al., 2018), whose scale is shown at the lower right corner below the map. The beach ball denotes the Great Wenchuan earthquake (Mw 7.9, May 12, 2008), which occurred along the Longmenshan Fault, a thrust structure along the border of the Tibetan Plateau and Sichuan Basin. Abbreviations are as follows: AV, Arxan Volcano; CDDB, Chuan-Dian Diamond Block; CV, Changbai Volcano; DV, Datong Volcano; HB, Himalaya Block; HV, Hainan Volcano; JB, Junggar Basin; JV, Jeju Volcano; KV, Kunlun Volcano; OB, Ordos Basin; QDB, Qaidam Basin; QFB, Qilian Fold Belt; SCB, Sichuan Basin; SGFB, Songpan Ganzi Fold Belt; SLB, Songliao Basin; TV, Tengchong Volcano; UV, Ulleung Volcano; WV, Wudalianchi Volcano.

margin of the Eurasian Plate along the Nankai Trough and the Ryukyu Trench (e.g., Wu et al., 2016), where it is descending beneath the Eurasian Plate at ∼3-5 cm/yr. In the Early Miocene (∼23 Ma), an Australian continental promontory began to collide with the Southeast Asian margin of the Eurasian Plate in eastern Indonesia (e.g., Hall, 2011), and now the Australian Plate continues to subduct northwards beneath the Indonesian arcs at ∼5.6 cm/yr along the Sumatra and Java trenches. The Indian Plate is currently subducting northeastwards beneath Southeast Tibet and the Indochina Block at ∼3.7 cm/yr, resulting in the shortening and rising of the Tibetan Plateau as well as large-scale continental deformation in the lithosphere extending from the Himalayan orogen to the Baikal rift zone in central Asia (e.g., Tapponnier et al., 1982; Yin, 2010).

Mainland China, as the tectonic transitional zone between the Gondwana and the Laurasia continents, is characterized by the complicated tectonic collage of three major Precambrian blocks (North China Craton, South China Block, and Tarim Block) and ancient continental fragments, separated and sutured by surrounding Phanerozoic orogenic/fold belts (e.g., Zheng et al., 2013). Mainland China also contains a few small cratons and terranes with diverse origins and complex histories of amalgamation, of which the Ordos and Sichuan blocks, composed of the two rigid continental cores in the East Asia convergent tectonic system, are tectonically relatively stable compared with the adjacent areas. They have suffered less deformation in the long geological history, and may have played an essential role in the formation and tectonic evolution of mainland China. As a result of the unique tectonic setting where the Paleo-Asian, Tethyan, and Paleo-Pacific/Pacific oceanic domains meet in a triangular framework, China is also an active seismic and intraplate volcanic region with significant neo-tectonic activities. According to the USGS Earthquake Catalog (`https://earthquake.usgs.gov`, last accessed June 2022), more than 2,000 earthquakes with a magnitude greater than 5.0 have occurred in mainland China, Japan Islands, and surrounding regions during the last 20 years, for example, the Great 2008 Wenchuan earthquake (Mw 7.9) and the Great 2011 Tohoku-oki earthquake (Mw 9.0). A few active intraplate volcanoes with eruptions during the Holocene exist in mainland China, such as the Arxan, Wudalianchi, and Changbai volcanoes in Northeast China, the Hainan volcano in South China, Tengchong volcano in Southwest China, and the Kunlun volcanic group in northwestern Tibet (Figure 2.1). The South China Sea, as one of the back-arc basins in the circum-Pacific tectonic domain, is a non-volcanic passive margin basin. Its unique tectonic setting has challenged ideas on the conventional intraplate continental rifting pattern (e.g., Zhang et al., 2020).

Over the past two decades the three-dimensional (3-D) crust and mantle structure beneath the broad Asian region has attracted much attention in seismic studies due to its complicated and unique geological setting involving active lithospheric deformation, intracontinental rifting, intraplate seismotectonics, volcanism and magmatism, continent-continent collision, oceanic plate deep subduction, and mantle dynamics. Following the pioneering works of Aki and Lee (1976), Aki et al. (1977), and Dziewonski et al. (1977), seismic tomography has made substantial progress with the growth of seismic data quality and quantity, and developments in both numerical mathematics and theoretical seismology. Seismic imaging has been the most effective method to detect the 3-D structure of the crust

and mantle across a range of scales and enhanced our knowledge of physics, chemistry, and geodynamic processes of the Earth's interior. Many tomographic models, based on various categories of data (e.g. body-wave arrival times, surface-wave dispersion, shear and surface waveform), have been constructed for East and Southeast Asia (e.g., Lebedev and Nolet, 2003; Huang and Zhao, 2006; Zheng et al., 2008; Li and van der Hilst, 2010; Chen et al., 2015; Shen et al., 2016; Tao et al., 2018; Ma et al., 2019; Han et al., 2021). This has greatly improved our understanding of the plate tectonic and mantle dynamic settings of this region, and its large-scale mantle structure is now well agreed upon. Because of the limitations in the methodology, seismic observation data, and computer powers then available, however, the fine-scale 3-D structure of the crust and mantle beneath China and adjacent regions has not been well established. Although the regional tomographic models can achieve a relatively higher spatial resolution, most are just limited to the shallow upper mantle. Moreover, the models for the same region are usually not consistent due to the differences in the initial reference model, observation dataset, and the seismic imaging technique adopted. To address these shortcomings and problems, we collected a phenomenal waveform data set across the broad Asian region to construct a reference seismic model. It should be a crucial step in enhancing our understanding of the subsurface behavior of cold subducting slabs and hot mantle flows and their dynamic relation to the tectonic evolution of the overriding plates as mentioned above.

With recent advances in numerical methods and high-performance computing (e.g., Komatitsch and Tromp, 2002a,b; Gokhberg and Fichtner, 2016; Afanasiev et al., 2019), it has become computationally feasible to improve images of the Earth's interior using numerical forward and adjoint simulations of seismic wave propagation through 3-D heterogeneous Earth models in iterative inversions, ranging from regional and continental (e.g., Tape et al., 2009; Fichtner et al., 2009; Zhu et al., 2012; Chen et al., 2015; Krischer et al., 2018) to global scale (e.g., Lekić and Romanowicz, 2011; French and Romanowicz, 2014; Bozdağ et al., 2016; Lei et al., 2020). Synthetic seismograms calculated by finite-element or finite-difference methods contain the full seismic wavefield information, including all body and surface wave phases as well as scattered waves generated by lateral variations of the model physical properties. Therefore, the amount of exploitable information used in full-waveform inversion (FWI) is significantly larger, which provides new opportunities for improving images of the Earth's interior. However, relying on accurate numerical wavefield simulations, FWI is not applied as widely as other traditional techniques, such as ray-based travel-time tomography (e.g., Zhao et al., 1992; Grand et al., 1997; Zhao, 2004; Li et al., 2008; Ma et al., 2019) and finite-frequency tomography (e.g., Dahlen et al., 2000; Hung et al., 2000; Montelli et al., 2004; Hosseini et al., 2020). This primarily stems from the substantial computational requirements since FWI via the adjoint-state method requires two numerical simulations of the wave equation for each source at each iteration to obtain the gradient of the misfit with respect to the model parameters. Additionally, the computational cost of the simulation scales with frequency to the power of 4 in a 3-D medium (e.g., Virieux and Operto, 2009; Thrastarson et al., 2020). The Fresnel zone of the higher-frequency wave is narrower because of divergence decreasing with increasing frequency, and as a consequence, more events are required to construct a more accurate gradient in

order to constrain the physical properties of the earth model sufficiently. To this end the dynamic mini-batch optimization, conceptually related to the stochastic gradient descent method, is an effective strategy that can drastically reduce the computational burden of real-data FWI applications (e.g., van Leeuwen and Herrmann, 2013; Boehm et al., 2018; Matharu and Sacchi, 2019; van Herwaarden et al., 2020).

The dense deployment of temporary and permanent broadband seismic stations in mainland China and adjacent regions (e.g., ChinArray project, China Digital Seismic Network, Korea National Seismograph Network, F-net Broadband Seismograph Network) in the past two decades provides notable advantages to construct a new tomographic model of the crust-mantle structure beneath the broad Asian region, using full-waveform inversion of three-component (vertical, radial, transverse) recordings. Moreover, in agreement with the collaborative and evolutionary framework for the construction of a multi-scale seismic model (Fichtner et al., 2018), the final result of this work will flow back into the Collaborative Seismic Earth Model (CSEM), which can further serve as a foundation for future generations of 3-D reference Earth models. Such models would be crucial to accurately locate earthquakes, invert earthquake sources, assess seismic hazards in earthquake-prone regions, assist accurate earthquake early-warning, and detect and locate nuclear explosions. They would also be important to refine plate tectonic studies in the coming years (Wu et al., 2016).

2.3 Seismic Data

From the Global Centroid Moment Tensor (GCMT) solution database (Ekström et al., 2012), we selected ∼2,500 earthquakes within the moment-magnitude range $5.0 \leq \mathrm{Mw} \leq 6.9$ in the domain of interest. The lower bound of the magnitude range is chosen to provide a high signal-to-noise ratio in usable recordings. The upper bound is empirically chosen to neglect finite-source effects in seismogram modelling. All events occurred between January 2009 and October 2018. Moreover, they were chosen to evenly distribute in seismogenic zones associated with active subductions, Mid-ocean ridges, and tectonic deformation and faulting (Figures 2.1 and 2.2).

We obtained three-component seismograms from nearly all available permanent broadband seismic networks in mainland China (CEArray, `http://www.seisdmc.ac.cn/`; Zheng et al., 2010), South Korea (KNSN, `http://www.kma.go.kr/`), Japan (F-net, `http://www.fnet.bosai.go.jp/`), and other regional and global temporary broadband seismic networks, made available by the Incorporated Research Institutions for Seismology Data Management Center (IRIS DMC, `http://ds.iris.edu/ds/nodes/dmc/`). To enable better performance and fast parallel processing on high-performance clusters, the Adaptable Seismic Data Format (ASDF; Krischer et al., 2016) serves as a data container in this study. It combines all seismic traces, the event information file (in QuakeML format), and the station information file (in StationXML format) for an event into a single file using the HDF5 format. The adjoint method is maximally efficient for cases with a sizeable seismogram-to-event ratio. Also the computational cost for forward and adjoint simu-

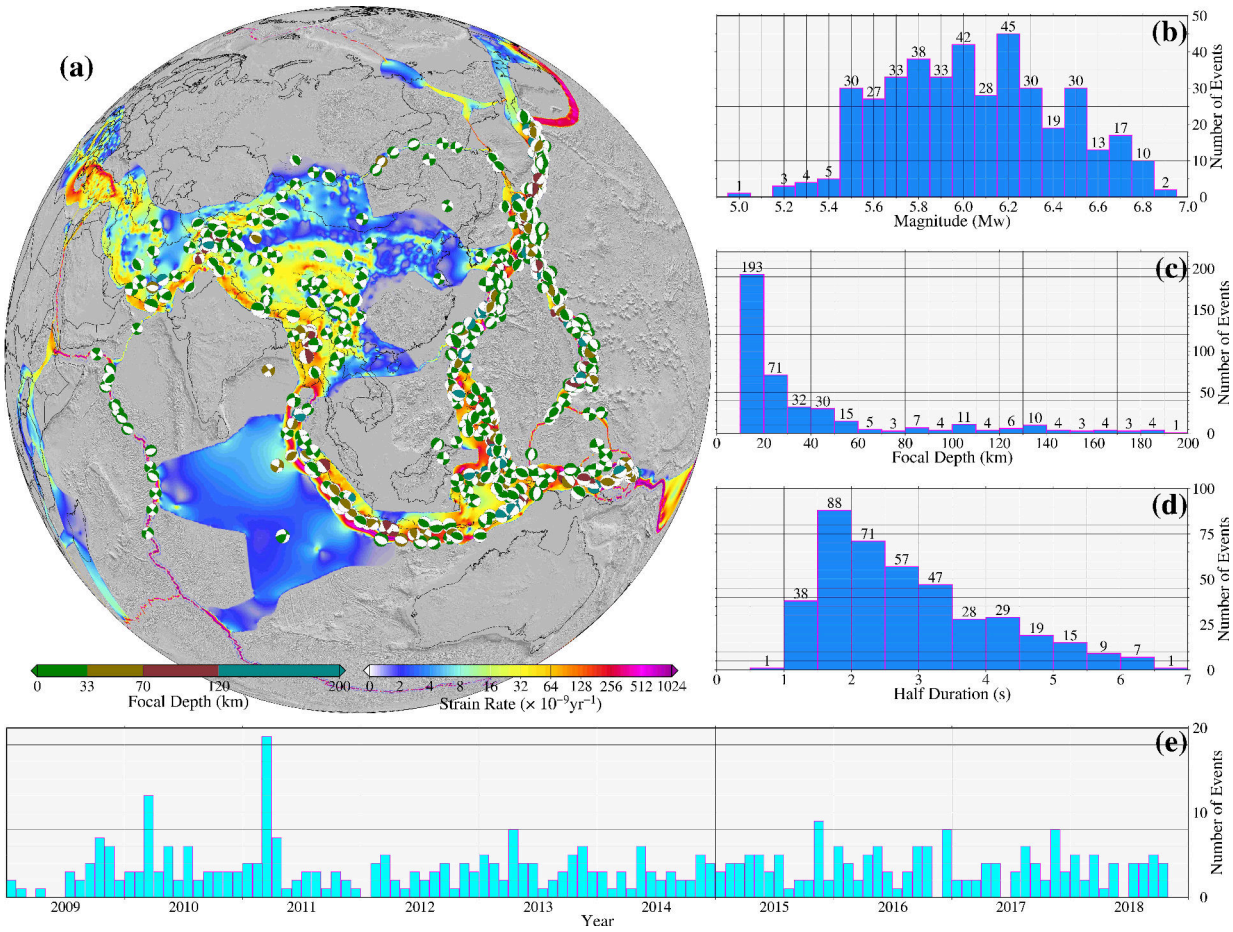

Figure 2.2: 410 earthquakes used for the full-waveform inversion in this study. (a) Distribution of 410 earthquakes. The colors of moment tensor beach balls denote the focal depths, whose scale is shown at the lower left corner below the map. The strain rates are inverted from GPS measurements (Kreemer et al., 2014). The color scale is not linear and saturated at high values, whose scale is shown at the lower right corner below the map. (b)-(e) Histograms of earthquake moment magnitudes, focal depths, half durations, and origin times.

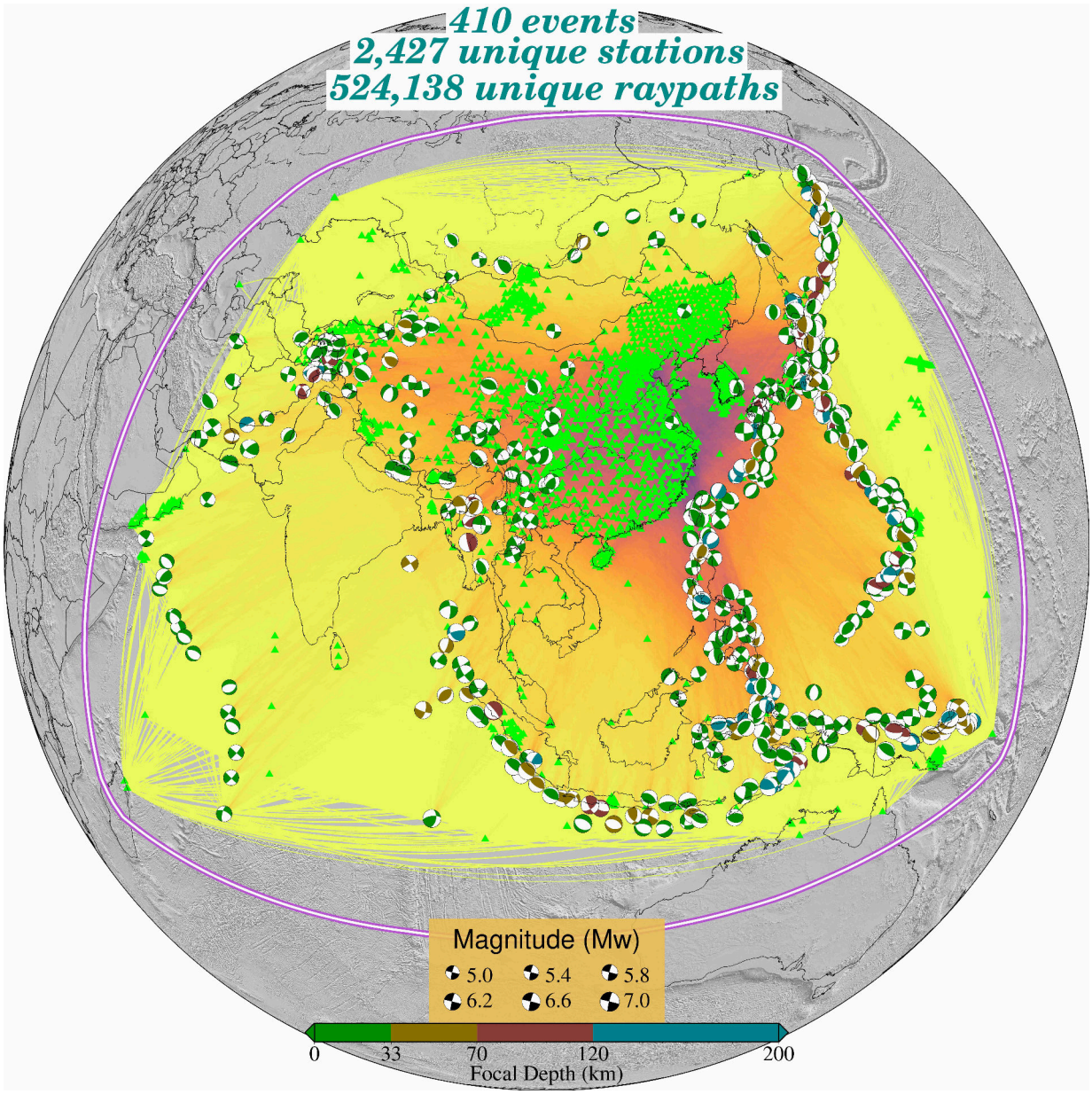

Figure 2.3: Surface-projected ray density map of the events and stations used in this study, ranging from dark red (best data coverage) to light yellow (least data coverage). Earthquake locations and mechanisms are indicated by moment tensor beach balls and stations by green triangles. In total, 410 earthquakes were recorded at 2,427 unique stations, and the complete data set has 524,138 unique source-receiver pairs. The outer boundary marks the start of the absorbing boundary region. The great circle paths of all traces used in this study are located within the outer boundary, which can mitigate the influence of the absorbing boundary on the inversion.

lations does not depend upon the number of receivers. Hence we preferentially choose events with the maximum number of high-quality seismic recordings in similar locations. To optimize the seismic wavefield azimuthal coverage, we employ earthquakes located in all azimuths with respect to CEArray stations, which are the key component of our data set. With a total of 2,427 available seismic stations and 410 seismic sources, our final data set contains more than 0.5 million three-component seismograms, resulting in tremendous amounts of high-quality recordings from $\geq$ 1,300 unique stations per event. The distribution of events, seismometers, and the surface-projected ray coverage are illustrated in Figure 2.3. Although the sensitivity of the measurements in FWI is not restricted to the ray paths, the data coverage determines the first-order features of a tomographic result, making a surface ray density plot a useful proxy to judge the potential resolution of the final model. It shows, for instance, that mainland China, the India-Eurasia collision zone, the Philippine Sea Plate, as well as the western Pacific and the Indonesia subduction zones are well covered in our region of interest.

2.4 Forward and Inverse Modelling

We perform seismic waveform modeling and inversion mainly based on the methodology established in Fichtner (2011), Kennett and Fichtner (2020), and similar works (e.g., Colli et al., 2013), which is depicted schematically in the workflow shown in Figure 2.4. We introduce some technical details of the initial model, seismic waveform modeling, optimization, and workflow management in the following sections.

2.4.1 Starting Model and Numerical Waveform Modeling

It is well known that FWI is a large nonlinear minimization problem that can only be solved efficiently with iterative gradient-based minimization schemes, during which each iteration involves a minor update constructed through linear operations on the residuals. An accurate starting model can help avoid convergence towards a local minimum or saddle points, increase the length and number of measurement windows at the beginning stage of the inversion, and accelerate the convergence of the iterative inversion towards the global minimum. Therefore, we implement a 3-D initial model that contains the long-wavelength features of the crust and mantle beneath the broad Asian region, extracted from the CSEM (Afanasiev et al., 2016; Fichtner et al., 2018). The background model of the CSEM was constructed from the 3-D long-wavelength S-velocity model S20RTS (Ritsema et al., 1999), with P-velocity variations derived from a depth-depend P-to-S scaling relation (Ritsema and van Heijst, 2002). The initial crustal model was derived from the model of Meier et al. (2007b,a), which includes estimations of both S-wave velocity and crustal thickness. The initial model additionally contains contributions from previous FWI models of Japan (at periods down to T=20 s; Simutė et al., 2016) and Australia (at periods down to T=30 s; Fichtner et al., 2010). The model for wave propagation simulations is parameterized in horizontally and vertically propagating/polarized P and S velocities (V_{PH}, V_{PV}, V_{SH}, V_{SV}),

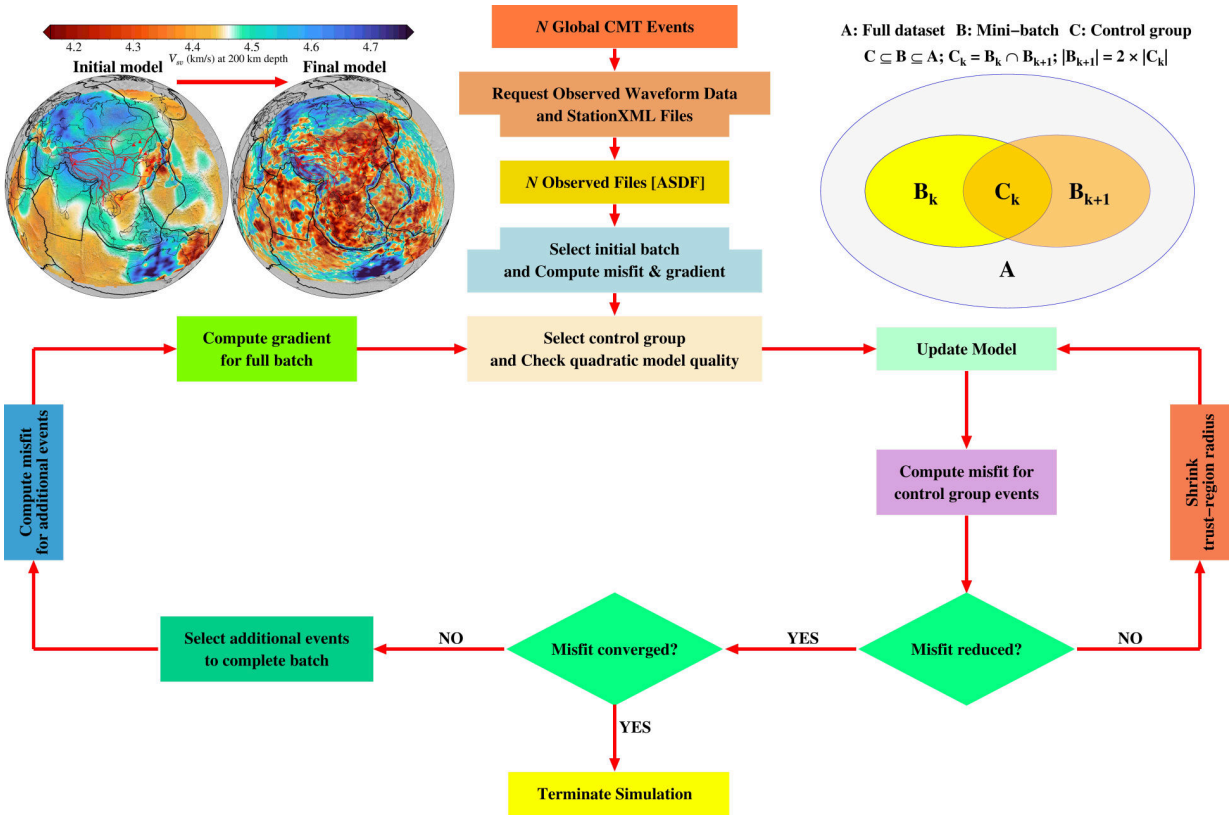

Figure 2.4: Schematic representation for the stochastic-gradient mini-batch full-waveform inversion. Mini-batch B_k for the iteration k is a subset of the complete data set A, and the mini-batch for the next iteration $k+1$, B_{k+1}, consists of the control group C_k, a subset of B_k as well as other events, which are quasi-randomly chosen from the complete data set A. It starts with the preparation of observed waveform data, as discussed in Section 2.3, and assembles the complete data set in the initialization stage. We select the first mini-batch using Mitchell's best candidate algorithm, calculate the synthetic seismograms, misfits, and gradients with a suitable initial model, and update the model. At the next iteration, we select the control group events from the previous mini-batch and recalculate misfits of the control group events with the updated model. If misfits are reduced at this stage, new events from the complete data set are selected to complete the next mini-batch, for which misfits and gradients are then again calculated with the updated model. This procedure is iterated until a satisfactory fit is achieved.

mass density (ρ), shear attenuation (Q_μ), and the dimensionless parameter (η), which is used to control the dependence of P and S velocities on the incidence angle (Dziewonski and Anderson, 1981).

FWI is an efficient method to extract information from complete seismic waveforms and recover the "best fit" model by iteratively minimizing the cumulative misfit between observed and synthetic seismograms from forward modelings. It guarantees that the observed waveform misfits are generated by the undiscovered Earth structure and not by approximation errors, and further avoids approximation artifacts from the forward modelling. In this study, accurate numerical solutions of the visco-elastic wave equation in a radially anisotropic Earth media are computed with the spectral-element seismic wave propagation solver Salvus (Afanasiev et al., 2019) accelerated by Graphics Processing Units. Salvus is a suite of highly parallelized software performing full-waveform modeling and inversion across all scales. Due to the non-uniform geometry of seismic networks and uneven distribution of seismic sources, an adaptive mesh is adopted for seismic wave propagation simulations to reduce the computational burden (Figure 2.3).

2.4.2 Misfit Function and Optimization Scheme

Seismic tomography allows us to infer Earth's internal structure from the misfit measurements between observed and synthetic data. The choice of a suitable misfit function that quantifies the differences between synthetic and observed waveforms and extracts the maximum amount of meaningful information from each seismogram plays an important role in the outcome of an inversion. The dependence of seismic amplitude characteristic attributes on variations in the medium properties is usually highly nonlinear. The absolute amplitudes are strongly influenced by local anomalies near the receiver, and important information about the deep Earth can be masked by shallow structures such as sedimentary basins (Fichtner et al., 2010). In contrast, phase differences are quasi-linearly related to 3-D Earth structural variations and so are well suited for an iterative gradient-based misfit minimization scheme. Here we work with the phase misfit measure in the time-frequency domain (e.g., Kristeková et al., 2006, 2009; Fichtner et al., 2008). The phase misfits do not require the identification and isolation of individual seismic phases, and are naturally applicable to any kind of seismic wave, regardless of its composition of seismic phases. The total phase misfit χ_p is defined by an integral over all phase differences in the time-frequency domain as

$$\begin{aligned} \chi_p^2 &= \int_t \int_\omega W^2(t,\omega)[\Theta_{syn}(t,\omega) - \Theta_{obs}(t,\omega)]^2 dt d\omega, \\ W &= \frac{log(1+|\tilde{u}_{obs}|)}{max(log(1+|\tilde{u}_{obs}|))}, \end{aligned} \tag{2.1}$$

where W is the weighting function, $\tilde{u}$ is the time–frequency representation of seismic signal u as calculated via the Gabor transform, and Θ_{syn} and Θ_{obs} are the phase of the synthetic and the observed seismogram traces. For a derivation of this misfit functional and corresponding adjoint source, see Fichtner et al. (2009) and Fichtner (2011).

To reduce the effect of clustering on the sensitivity of Fréchet kernels across the domain of interest due to the uneven distribution of seismic stations, we employ the geographical weighting strategy, which empirically leads to faster convergence of nonlinear inversions. To this end, the final misfits for a given receiver location x_r are multiplied by the factor

$$W_r = \left(\sum_{i=1, i \neq r}^{n} \frac{1}{|x_i - x_r|} \right)^{-1}. \tag{2.2}$$

We select measurement time windows in a semi-automatic fashion utilizing a sliding window cross-correlation, where initial windows are preselected based on the noise level and the overall similarity between observed and synthetic waveforms. This yields time-dependent cross-correlation coefficients and time shifts, which are further combined with specific criteria to determine the final time windows (e.g., Maggi et al., 2009; Krischer et al., 2015; Thrastarson, van Herwaarden, Krischer and Fichtner, 2021). Subsequently, the selected time windows are manually checked and adjusted to avoid cycle skipping, especially for the high-frequency signals used in the final inversion stage. As the iterations progress, the number of selected time windows for each event and the number of traces with windows increase almost exponentially from the long to the short period bands.

Our gradient-based optimization scheme iteratively improves the model to reduce the waveform misfit between iterations. To achieve an optimal global solution and mitigate the risk of convergence toward a local minimum, we divide the whole inversion procedure into three successively broadened period bands of 70-120 s, 50-120 s, and 30-120 s. This implies a multi-scale evolutionary inversion scheme of starting with the long period to determine large-scale structure before marching into the higher-frequency domain to reveal the small-scale structure (e.g., Bunks et al., 1995; Krischer et al., 2018). We calculate sensitivity kernels of the cumulative phase misfit with respect to the model parameters for each individual event through the adjoint method (e.g., Tarantola, 1988; Tromp et al., 2005; Fichtner et al., 2006). To reduce the parameter space, we enforce $\eta = 1$ and $V_{PH} = V_{PV}$ and invert only for the isotropic P velocity (V_P), the velocity of horizontally polarised S waves (V_{SH}), the velocity of vertically polarised S waves (V_{SV}), and mass density (ρ) simultaneously over the course of the inversion's three stages. The other parameters are kept at the initial values of the starting model throughout the inversion.

For each event, it is crucial to remove source and receiver imprints from the raw gradient since they generally show strong localized sensitivity in these areas. In addition, the raw gradient usually contains small-scale oscillations and high-frequency artifacts, and it is essential to prevent these sub-wavelength structures from sneaking into the model by effectively convolving the gradients through the numerical solution of the diffusion equation (e.g., Afanasiev et al., 2019). The smoothed gradient determines the descent direction, which is used to compute a model update through suitable optimization algorithms. The Limited-memory BFGS (L-BFGS) is a quasi-Newton method of optimization, which utilizes curvature information based on approximation of the Hessian (the second derivative of the misfit) and its inverse constructed from the gradients and models of previous iterations (Liu and Nocedal, 1989; Nocedal and Wright, 1999). The L-BFGS combined with

the trust-region method (Nocedal and Wright, 1999; Conn et al., 2000) can achieve a good approximation of the local objective function and significantly reduce the cost of an FWI update, which makes it greatly attractive for solving large-scale inverse problems. In this study, we performed all iterations based on the dynamic mini-batch approach coupled with the trust-region L-BFGS optimization technique (van Herwaarden et al., 2020). It is particularly well suited for our domain of interest for the following reasons: (1) the presence of redundancies in the data set because seismic sources tend to reoccur in similar locations, such as subduction zones. This limits the amount of new independent information to the gradient direction. (2) the large amount of continental-scale data set for 410 seismic sources. This poses a significant challenge for the computational requirements faced in real-data FWI applications. Different from conventional FWI or mono-batch FWI, which considers the data set as a whole in each iteration, the dynamic mini-batch FWI quasi-randomly selects a subset of the complete data set with the help of Mitchell's Best-Candidate algorithm (Mitchell, 1991) to approximate the complete gradient. It is specifically tuned to deal with redundancies in seismological data sets, potentially reducing the computational cost significantly (for details, see van Herwaarden et al., 2020, 2021).

2.4.3 Workflow Management

The FWI workflow based on the adjoint method consists of a series of iterations. Each is composed of a significant number of operations (e.g. construct, submit, and monitor forward and adjoint simulations for each seismic source, select measurement windows and calculate misfits between the observed and synthetic data, pre-processing and construction of adjoint sources, pre-processing and smoothing of gradient data, nonlinear optimizations, and model updates). One of the main challenges faced in large-scale FWI applications is to increase the quality and resolution of seismic models with massive data volumes in a reliable and trustworthy manner while keeping the time to solution as short as possible. Workflow management helps to automate the whole workflow by cutting down human interaction as much as possible, especially when performing repetitive tasks. To this end, we employ the FWI workflow manager ***Inversionson*** to fully automatically perform the above tasks until the convergence criteria of the whole inversion can be properly reached (for details, see Thrastarson, van Herwaarden and Fichtner, 2021). This workflow engine also automatically detects job failures and facilitates tracking of tasks and automatic job resubmission when necessary.

2.5 Model Assessment

In this section, we analyze the quality of the first generation full-waveform tomographic model ***SinoScope 1.0***. First, we present the iterative model evolution through three successively broadened period bands. Then we present examples of the waveform fit for a few events and stations relative to the initial and final models. Finally, we perform a computational expensive resolution test to estimate the resolution for the final model and

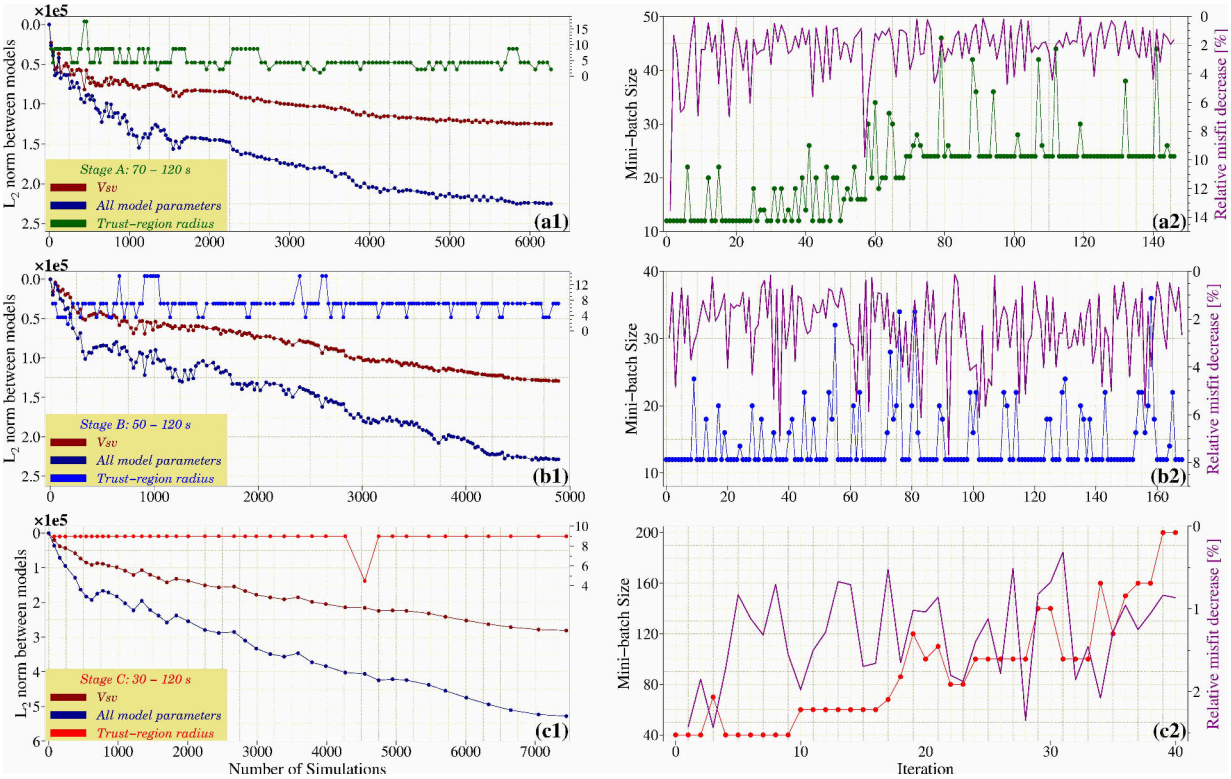

Figure 2.5: (a1)-(c1) Per-iteration L_2 distance between the initial and later models, and the trust-region radius used in the optimization for the three successively broadened period bands of 70-120 s (green), 50-120 s (blue), and 30-120 s (red). Note the general trend of L_2 distance gradually increasing. (a2)-(c2) Evolution of the mini-batch sizes and the relative misfit decrease of the control groups over the course of the inversion's three stages. Since the mini-batch size is closely related to the allowable angular difference, it automatically changes during the inversion to contribute more unique gradient information with the lowest possible computational cost. More events are required to approximate the complete gradient at the short period (30-120 s), because the Fresnel zone of the higher-frequency wave is narrower. Note the different axes.

the trade-offs between model parameters.

2.5.1 Model Evolution

For three successively broadened period bands of 70-120 s, 50-120 s, and 30-120 s in this study, the raw waveform data are corrected for the instrument responses to obtain the ground displacement and be filtered to match the spectral content of the synthetic data using ObsPy (Megies et al., 2011; Krischer et al., 2015) during the respective stages of the inversion. We first invert for the long-wavelength structures from the low-frequency waveforms and progressively towards higher-frequency waveforms for the shorter-wavelength structures, thereby avoiding strong dependence on the initial model and preventing the optimization procedure from getting trapped in local minimum.

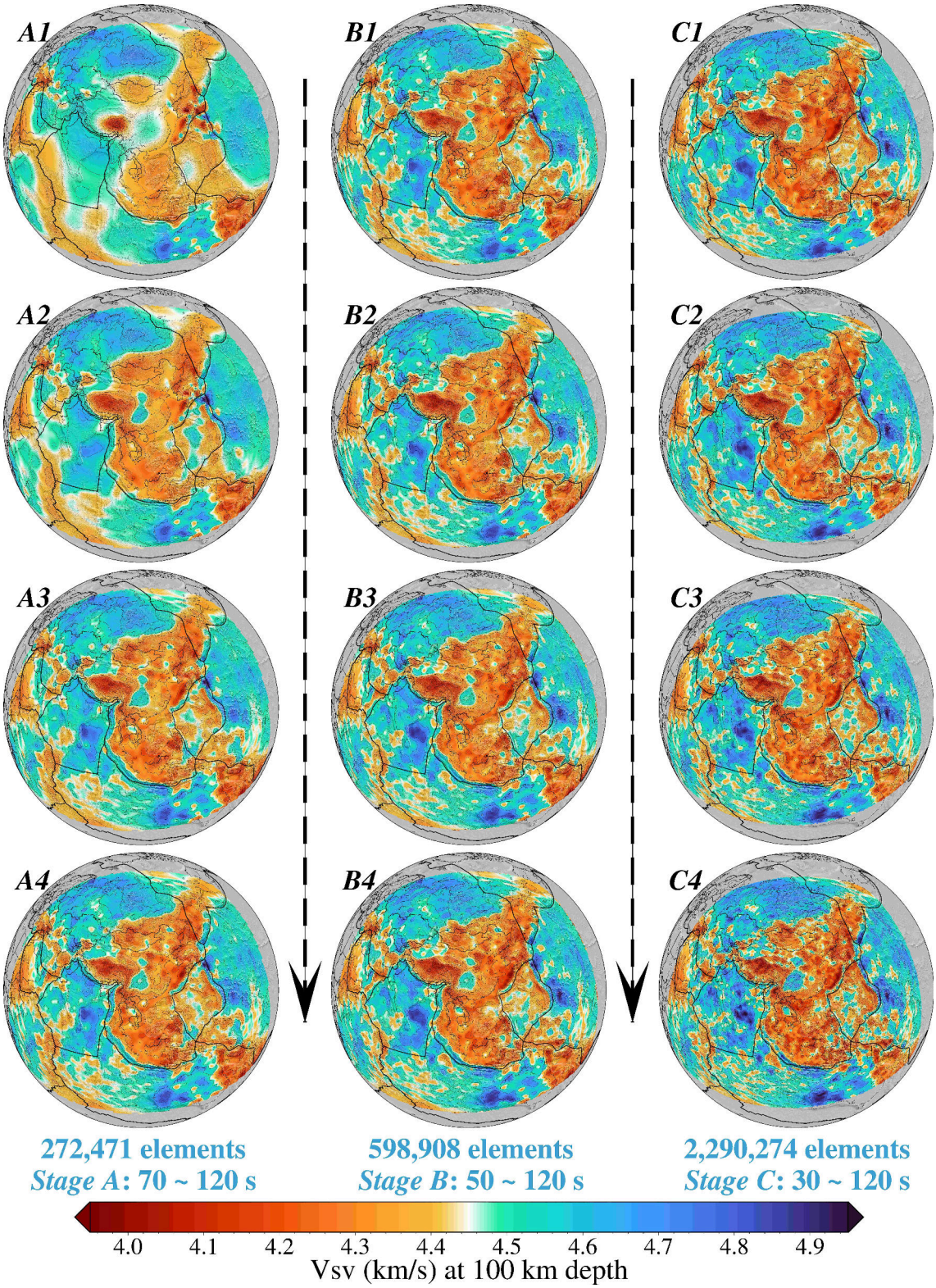

Figure 2.6: Horizontal slices of the models at different stages of the inversion. Shown are vertically polarized shear wave velocity (V_{SV}) distributions of the models at 100 km depth across the model domain. A1: the initial model for stage A (Fichtner et al., 2018); A2, A3, and A4: the dynamic mini-batch FWI results after 2068, 4180, and 6264 simulations (forward plus adjoint). B1: the initial model for stage B, interpolated from model A4; B2, B3, and B4: the dynamic mini-batch FWI results after 1640, 3264, and 4888 simulations. C1: the initial model for stage C, interpolated from model B4; C2, C3, and C4: the dynamic mini-batch FWI results after 2448, 4948, and 7448 simulations. The dynamic mini-batch iterations at the long periods mainly adjust the long-wavelength structure, and more fine-scale details appear during later iterations at short periods.

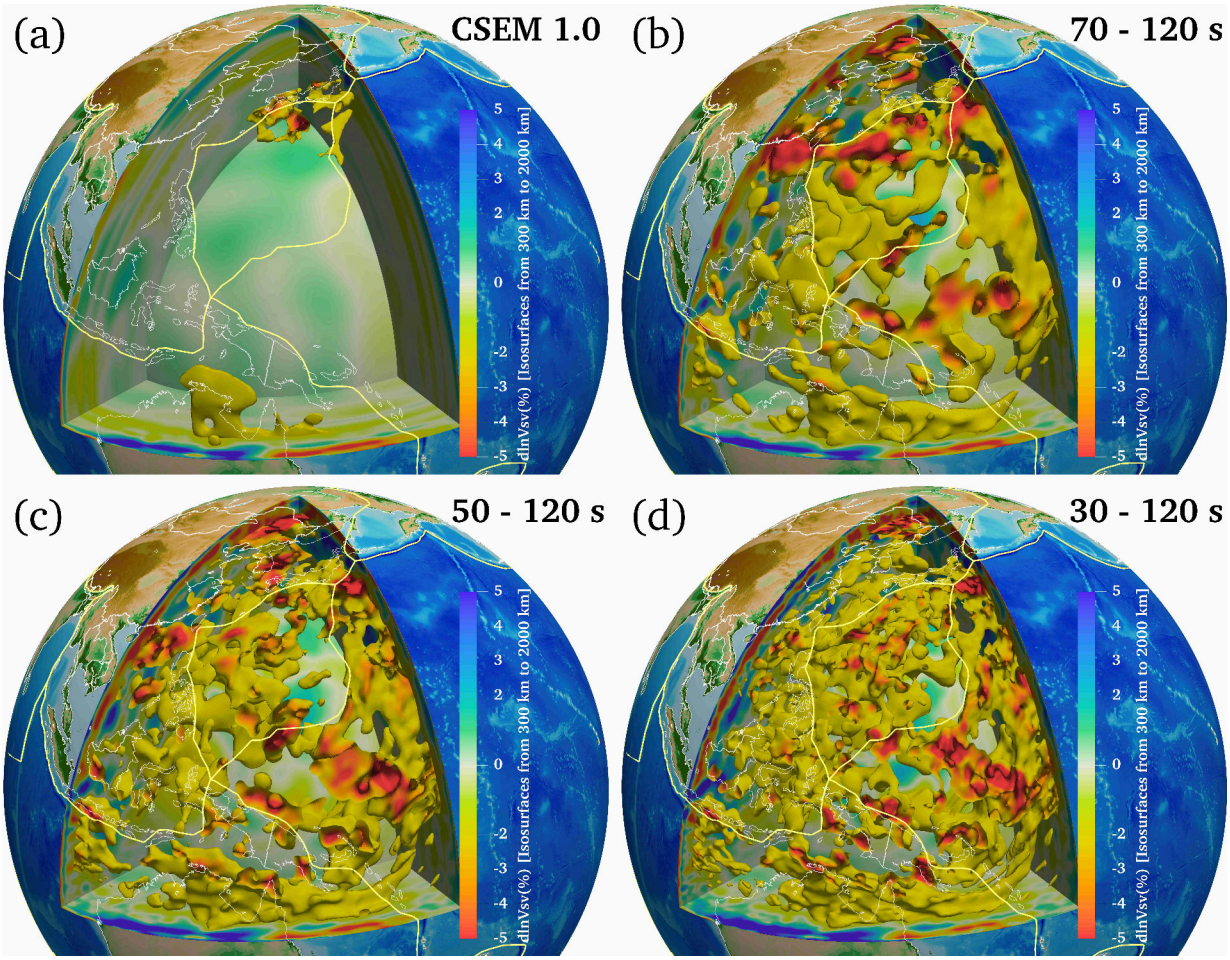

Figure 2.7: 3-D visualizations of the slow vertically polarized shear wave velocity structure (with V_{SV} perturbations $\leq$ -2%) beneath the eastern Asian regions in starting model CSEM (a), stage-A final model (b), stage-B final model (c), and stage-C final model (d) from a depth of 300 km to a maximum depth of 2,000 km. As the frequency increases, more body waves measurements are introduced in the inversion processes, and the seismic velocity structure of the Earth's deep interior is portrayed more and more finely. The color scale is identical for all plots, and each model is plotted relative to the lateral mean of the stage-C final model.

The multi-scale FWI scheme coupled with the dynamic mini-batches is a journey of continuously and steadily resolving fine-scale structures of the Earth's interior through forward and adjoint simulations. The drawback of the gradient-based optimization scheme is that it improves the models slowly with slight differences between iterations. Even significant reductions in misfit value may do not cause apparent improvement in the model parameters. For the longest-period stage A (70-120 s) at a substantially low computational cost, we performed 147 iterations, corresponding to 6,264 simulations of the forward plus adjoint on the numerical meshes with 272,471 elements (Figure 2.5). As the iteration progressed, we gradually increased the minimum control group size to provide a more accurate search direction, reducing the risk of the model's frequent rejection in the optimization. The L_2 difference between the current and initial models increases rapidly as the large-scale structure is well recovered during the first few dozen iterations and has been gradually stagnant in the final iteration stage, where more simulations would not have significantly improved model parameters. For stage B (50-120 s), we performed 168 iterations, corresponding to 4,888 simulations on the numerical meshes with 598,908 elements when the L_2 curve stagnated, and the inversion was forced to be terminated (Figure 2.5). For the shortest-period stage C (30-120 s), it is necessary to employ smaller elements and a shorter time step to resolve the smaller-scale structures. The computational costs are proportional to the number of elements and time steps. As a consequence, a single simulation of stage C is more than 20 times as expensive as a single one for stage A. We performed 41 iterations, corresponding to 7,448 simulations on the numerical meshes with 2,290,274 elements as the L_2 curve stagnated (Figure 2.5). Most notably, the trend of the L_2 curve, to a certain extent, broadly fluctuates in the early stage, which is probably because 410 events have not been wholly used to contribute their unique information to the gradient direction, and after that starts to become relatively smooth (Figure 2.5).

Figure 2.6 shows the model evolution with horizontal slices of the vertically polarised shear velocity at a depth of 100 km as a function of simulations at three different stages. For each stage of the multi-scale inversion, as it extends to shorter periods, the later stage keeps adding substantially more details into the model, which is precisely what we expected. FWI naturally inverts body and surface waves, which can combine the advantages of these two data types. The incorporation of surface waves can greatly reduce the vertical smearing effect that is typical for pure body-wave tomography in the upper mantle. Body waves provide additional lateral resolution at greater depths than pure surface-wave tomography can achieve. As illustrated in Figure 2.7, with the introduction of a large amount of body wave measurements in the inversion at the shorter periods, the deep structure of the model has been dramatically improved compared to the initial model.

2.5.2 Waveform Fits

In this section, we use waveform comparisons between initial and final models as well as the ability of the final model to explain the test data set to estimate the validity of the final model. Waveform comparisons were performed for selected source-receiver pairs that sample the study area along differently oriented ray paths. Figure 2.8 shows 10

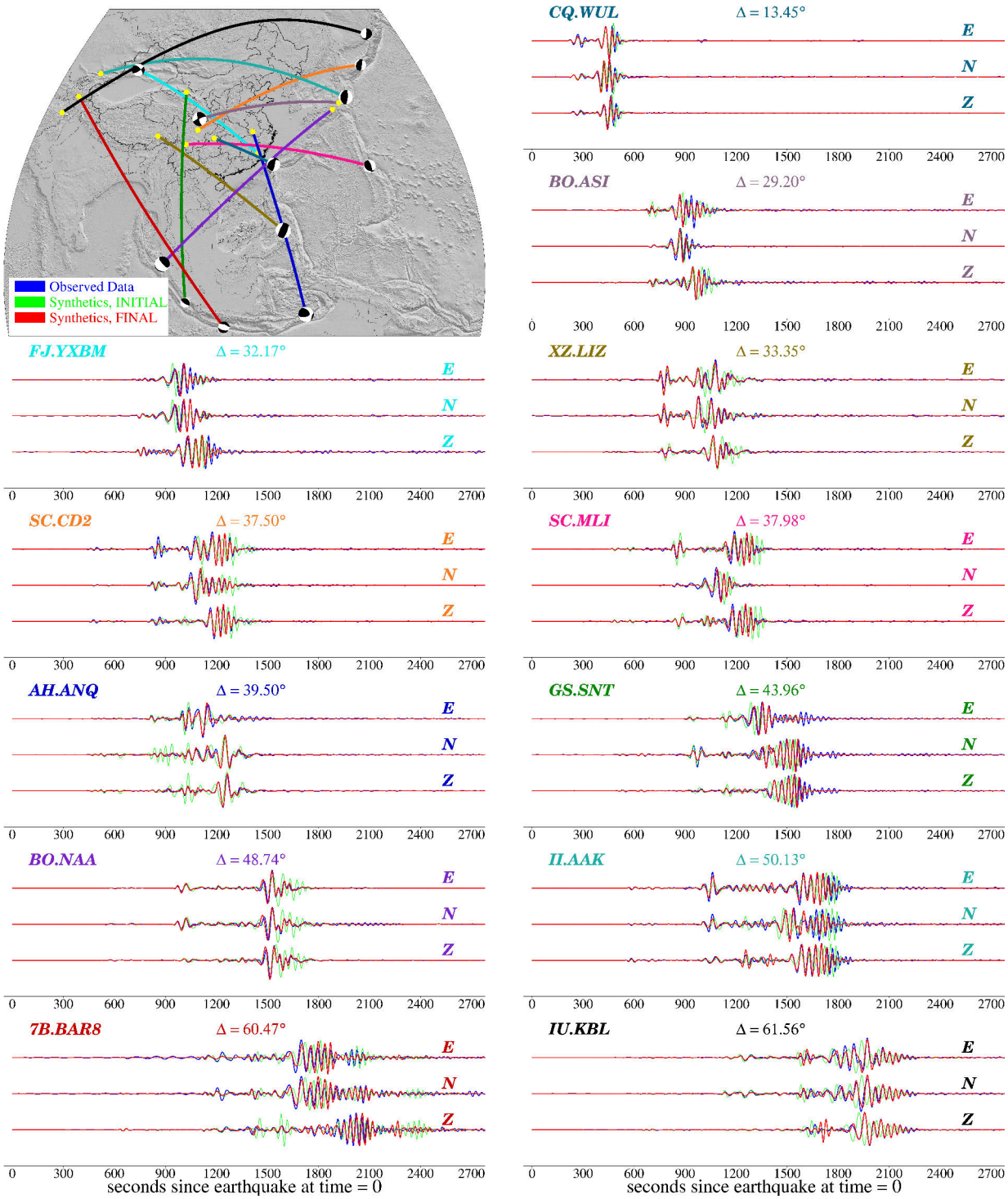

Figure 2.8: Comparisons of the overall waveform fit between synthetics calculated with the initial model CSEM as thin green lines, synthetics calculated with the stage-C final model as thick red lines, and the observed waveforms as thick blue lines for the event for which raypaths are shown in the topographic map with the same corresponding seismometer colors next to the seismograms. Epicenters are marked by beachballs in the topographic map, while solid yellow dots denote stations.

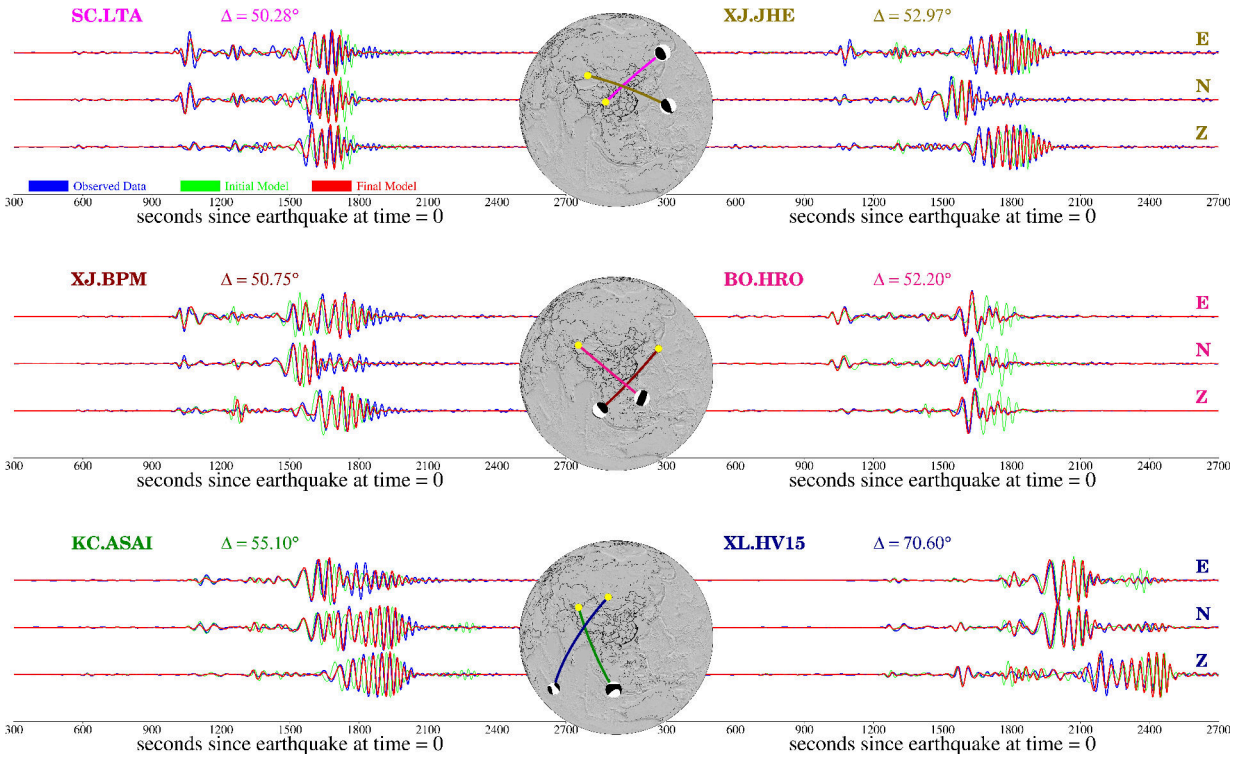

Figure 2.9: Representative waveform comparisons for several events from the test data set to assess the ability of the final model to explain new waveform data not used in the inversion. Waveform amplitudes are not scaled in order to compare the difference of waveform data more objectively. The observed waveforms are plotted as thick blue lines, synthetics calculated with the final model as thick red lines, synthetics calculated with the initial model as thin green lines, both of which are simulated at the dominant period of 30 s against to observed data. Epicenters are marked by beachballs in the topographic map, while solid yellow dots denote stations. Raypath colors match the corresponding stations next to the seismograms.

representative examples of the improved match between observed and synthetic three-component recordings from the test data set used in the inversion for the initial versus the final model. The total time window length of the fitted portions has increased by over an order of magnitude, with more than 70% misfit reduction compared with the original time windows. Also, note that the final model can explain body waves and fundamental- and higher-mode surface waves significantly better than the initial model. For most events, the amplitude fit improves along with the phase, although we did not explicitly invert the amplitude information.

We use a test data set including stations with the epicentral distance range of $50^\circ - 70^\circ$ that were not used in the above inversion, to further assess the quality of the final model and identify if the data has not been overfitting significantly. We first remove the observed data traces with no visible earthquake signal and adopt the normalized waveform difference L_2 misfit instead of the time-frequency phase misfit to measure all parts of observed and synthetic waveforms on all three components only for the fitted portions over all stations (e.g., Tape et al., 2010; Simutė et al., 2016; Krischer et al., 2018).

$$\chi(\mathbf{m}) = \frac{\int_0^T [u_{obs}(t) - u_{syn}(t, \mathbf{m})]^2 dt}{\sqrt{\int_0^T [u_{obs}(t)]^2 dt \int_0^T [u_{syn}(t, \mathbf{m})]^2 dt}} \tag{2.3}$$

where u_{obs} and u_{syn} are observed and synthetic waveform traces, T is the duration of the time series, and $\boldsymbol{m}$ is the model which the synthetic data is calculated with.

Figure 2.9 provides an exemplary comparison of synthetic three-component recordings with a duration of 3,600 s for the newly added events, calculated through the initial and the final models with the same mesh accurate for stage C. Synthetic seismograms improve significantly compared to observed seismograms when going from the initial to the final model. The average per-trace misfit $\overline{\chi}$ for the test data set calculated with the initial model is 2.15, which is considerably bigger than a value of 0.72 calculated with the final model. It indicates the model was greatly improved throughout the inversion. Based on the visual and quantitative analyses, we conclude that numerous simulations produced a well-improved model, which may be used to assist accurate earthquake early-warning, invert earthquake sources in the coming future.

2.5.3 Resolution Analysis

It is not possible to calculate the exact spatial resolution in the large-scale nonlinear inversion because there does not exist a simple mathematical operator relating the inversion input and output. In the absence of quantitative methods to evaluate resolution for an inverse problem, the checkerboard test is the most popular and relatively robust approach to estimating uncertainties in the linearized tomographic inversion with low computational costs, despite the fact that synthetic inversions, known to be called an "inversion crime", may heavily overestimate the resolving power, potentially misleading even in linear inverse problems (Humphreys and Clayton, 1988; Lévěque et al., 1993; Igel, 2017). Here, the checkerboard test is computationally prohibitive for assessing 3-D FWI quality, which

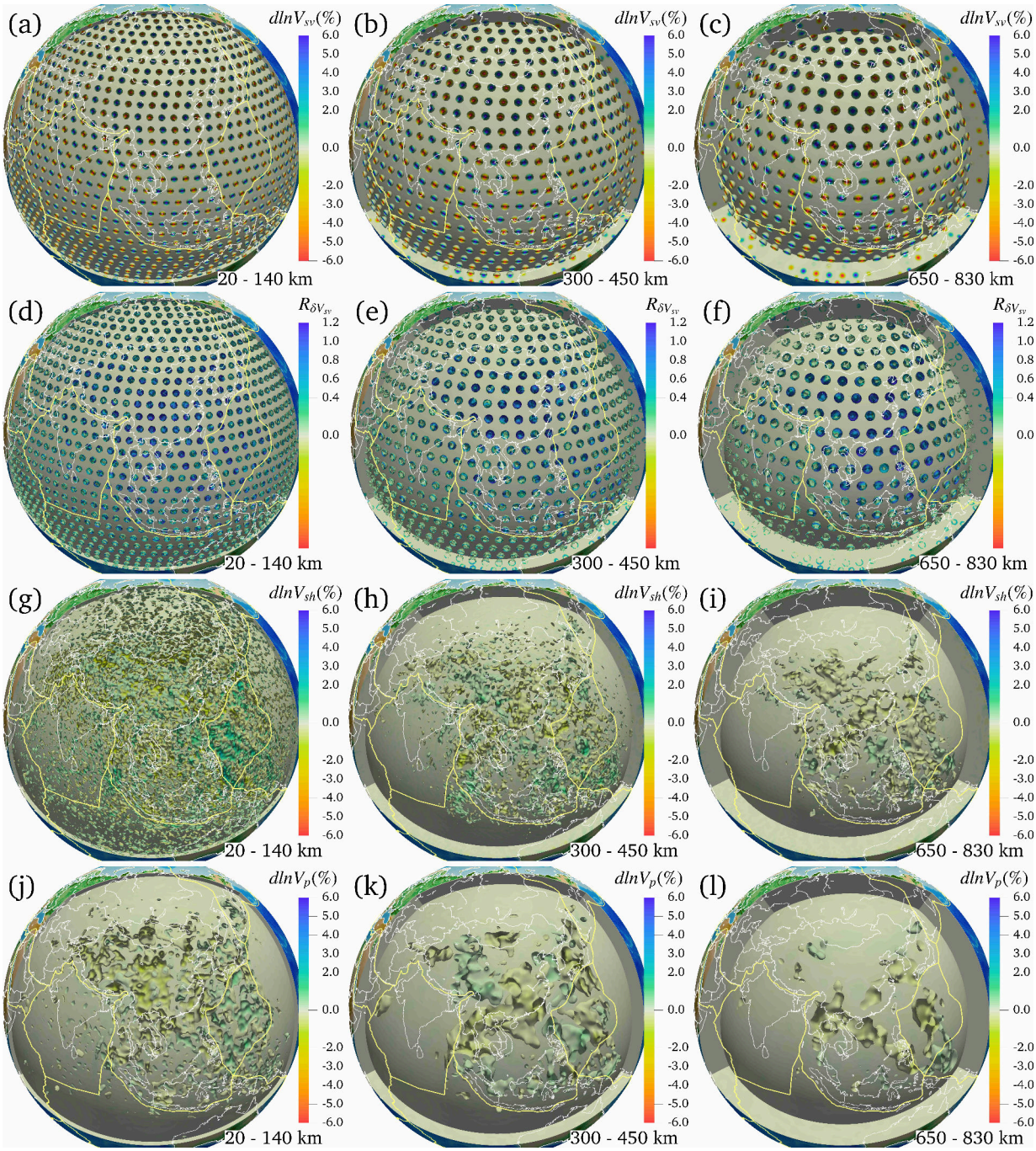

Figure 2.10: Resolution analysis and trade-offs estimates between model parameters based on iterative repairment experiments of random parametric perturbations. (a)–(c): 3-D visualizations of input ±8% Gaussian V_{SV} perturbations (δV_{SV}) at 20 km depth (σ = 40 km), 300 km depth (σ = 50 km), and 650 km depth (σ = 60 km); (d)–(f): The degree of repairment for the input perturbations with respect to V_{SV}, which provides ample information about the seismic structure and length scale our data set can robustly resolve; (g)–(i): Difference between ***SinoScope 1.0*** and the reconstructed model with respect to V_{SH}, which represents the trade-offs between V_{SV} and V_{SH}; (j)–(l): Difference between ***SinoScope 1.0*** and the reconstructed model with respect to V_P, which represents the trade-offs between V_{SV} and V_P.

requires roughly the same amount of computational resources as the actual inversion. One of the main problems facing resolution analysis and uncertainty quantification in FWI is that seismic waveforms inherently depend nonlinearly on the Earth's structure, meaning that the well-established machinery of linear inverse theory is no longer applicable (Backus and Gilbert, 1967; Tarantola, 2005). Generally, the nonlinear resolution analysis rests on (1) a quadratic approximation of the misfit functional in the vicinity of an optimal model, (2) an approximation of the Hessian built efficiently by gradient information from a set of perturbed models around the optimal model (Fichtner and Trampert, 2011a,b). The inverse of the pre-conditioned Hessian can serve as a proxy of the posterior covariance from which space-dependent uncertainties and correlations between parameters and inter-parameter trade-offs can be conservatively extracted. The stochastic-gradient optimization scheme employed in this work, however, adds new complexity to the already complex non-linear resolution analysis in the sense of non-identity Hessian information. To ameliorate this problem, we introduce a novel strategy to rigorously evaluate interparameter trade-offs between different physical parameters and the spatial resolution in the whole volume of interest by repairing the input 3-D Gaussian-sphere perturbations of the final model with a few L-BFGS iterations.

When synthetic waveforms can well fit the observed data and the inversion has reached convergence, input localized anomalies $\delta \boldsymbol{m}$ that perturbed the final model will be repaired or removed within the well-covered areas through several additional iterations. The difference between the final model and the reconstructed model can provide substantial information about the resolution length and trade-offs between different model parameters. We perturbed the final model (***SinoScope 1.0***) by interleaved Gaussian spheres with ±8% maximum amplitude of the vertically polarized shear wave velocity (V_{SV}) for a specific depth and standard deviation σ, leaving other parameters unchanged. The horizontal grid spacing of the Gaussian spheres are 400 km (with σ = 40 km at 20 km depth), 500 km (with σ = 50 km at 300 km depth), and 600 km (with σ = 60 km at 650 km depth). We adopt the parameter $\mathbf{R}$ to evaluate the degree of repairment for the input perturbations quantitatively.

$$\mathbf{R} = \frac{\mathbf{m}_2 - \mathbf{m}_3}{\mathbf{m}_2 - \mathbf{m}_1} \qquad s.\ t.\ \ \mathbf{m}_2 \neq \mathbf{m}_1 \tag{2.4}$$

where $\mathbf{m}_1$, $\mathbf{m}_2$, and $\mathbf{m}_3$ are the final model (***SinoScope 1.0***), the perturbed model, and the reconstructed model, respectively. When the input perturbation is completely removed, $\mathbf{R}$ is equal to 1.0; by contrast, when the input perturbation fails to be repaired, $\mathbf{R}$ is less than or equal to 0.0. We consider that the seismic structure can be well recovered when $\mathbf{R}$ is $\geq$ 0.4 and $\mathbf{R}$ is $\leq$ 1.2 at the corresponding grid node of the final model.

The conservative resolution length of each parameter of interest will be obtained with roughly 10 iterations, shown in Figure 2.10 and Figures S1-S5. Although additional iterations still have the potential to improve the amplitude recovery, it is legitimate to terminate the iteration for the computational reasons at this point. Gaussian anomalies are reasonably well removed within the crust and upper mantle, which is an expected result of the dominant position of the surface wave in the data set and the sensitivity distribution of the

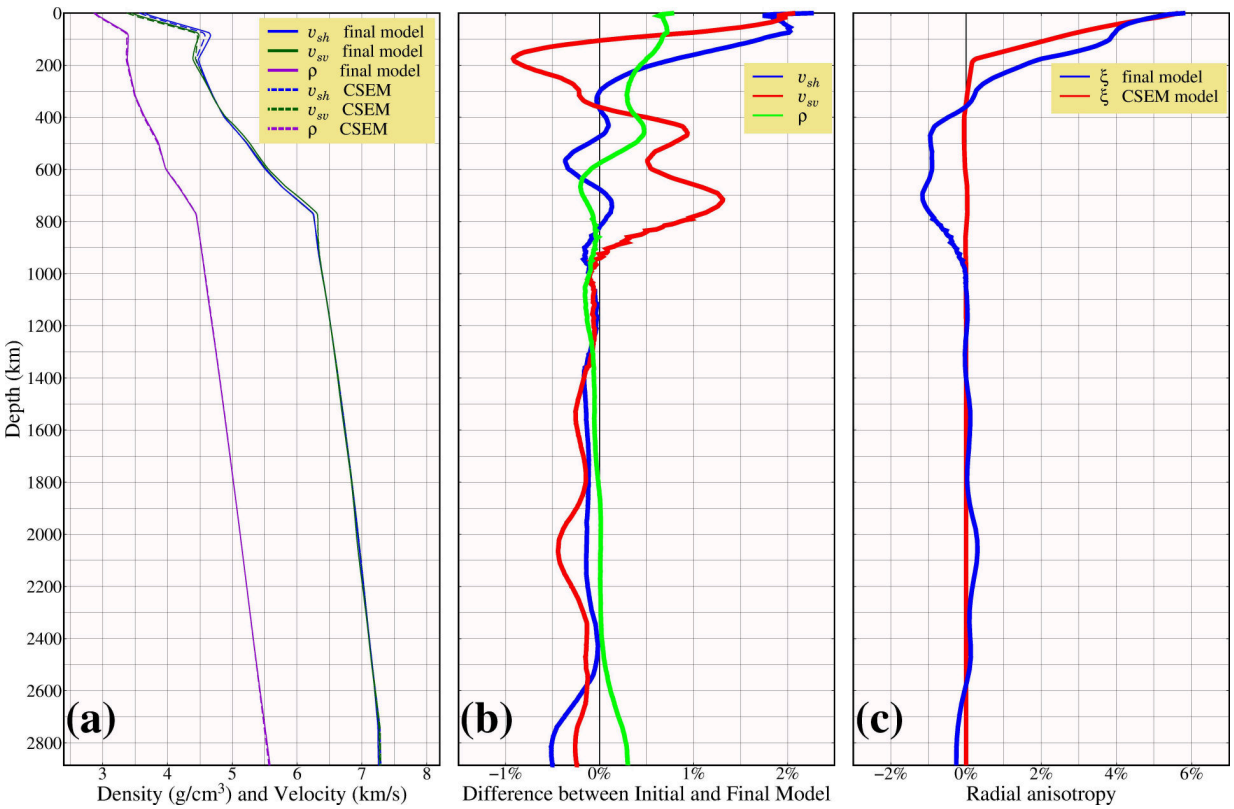

Figure 2.11: (a) Depth averages of the horizontally and vertically polarized shear wave velocities (V_{SH} and V_{SV}) and mass density (ρ) of the final model compared to the initial model CSEM Fichtner et al. (2018). (b)-(c) Depth average of the magnitude of the relative difference between the initial and final models for model parameters (V_{SH}, V_{SV}, and ρ) and radial shear wave anisotropy (ξ). The model has been updated considerably for all parameters from the surface down to the CMB through multi-scale evolutionary inversions. Especially, average shear velocities change significantly from the initial model above 1,000 km, reflected in the corresponding depth-averaged anisotropy.

surface wave. At greater depths, our data set still has an ability to illuminate the Asian region very well because of the incorporation of the body wave. Furthermore, the trade-off with other model parameters mainly occurs as random noise near the surface and does not produce a significant anomaly at the disturbance location. The resolution analysis shows that we can quantitatively interpret the observational characteristics spanning from the western subduction zones of the Pacific Plate to the north of the Indo-Australian Plate.

2.6 Results and Discussion

We have applied the methods described in the above sections to our waveform data set for the radially anisotropic crust-mantle structure in the broad Asian region. The lateral averages of the horizontally and vertically polarized shear wave velocities (V_{SH} and V_{SV}),

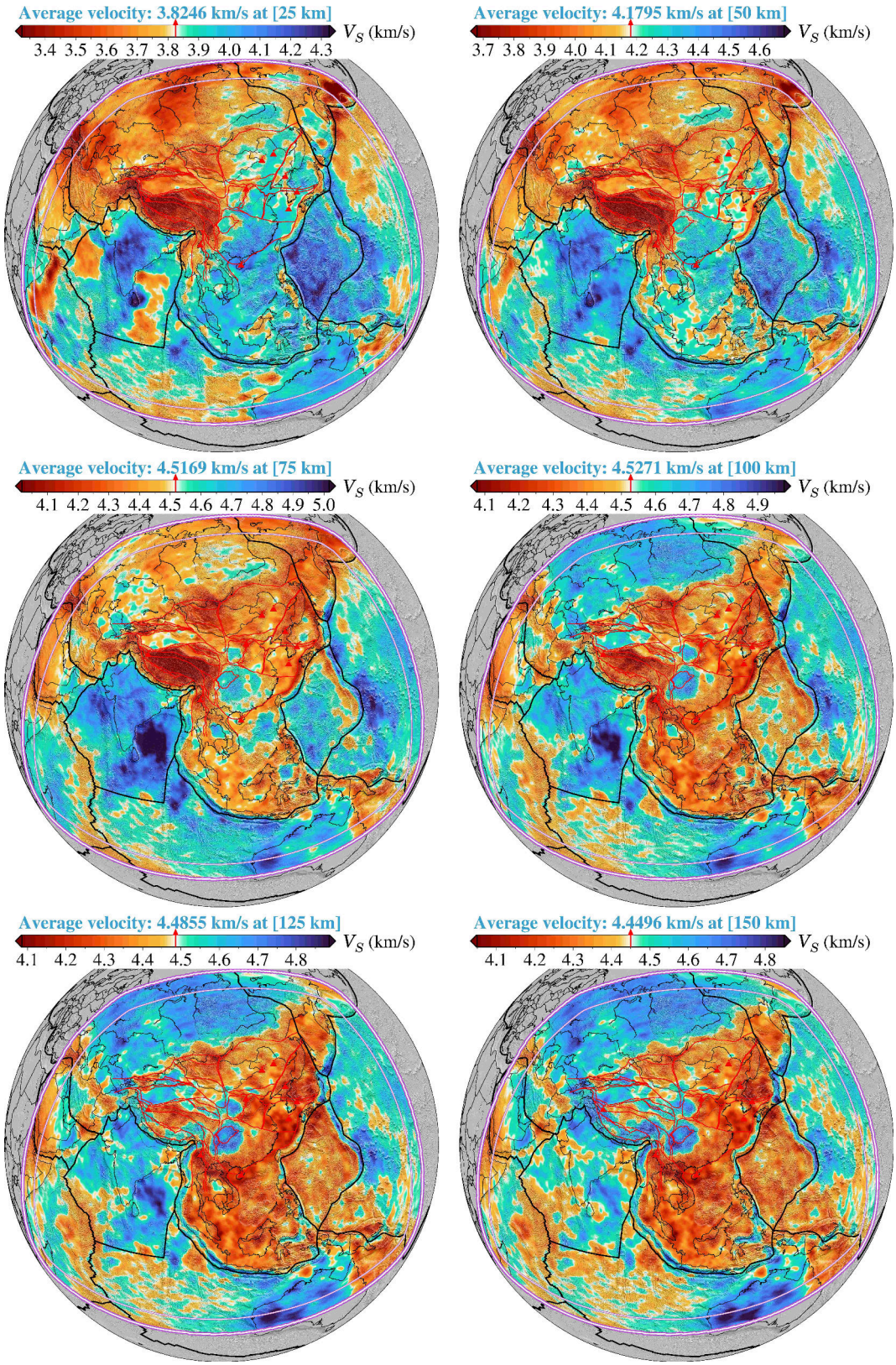

Figure 2.12: Horizontal slices through the final tomographic model showing the absolute isotropic V_S for the lithosphere at various depths. The depth of each layer is shown on the top of each map. V_S is the Voigt-Reuss-Hill average shear wave velocity. The thick white outer line marks the edge of the computational domain where we run all kinds of simulations and inversion procedures, and the thin white inner line marks the start of the absorbing boundary region. Within the buffer zone between the outer and inner model boundaries, wave propagation energy will be absorbed that would otherwise result in artificial reflections. The red triangles denote active intraplate volcanoes. The other labeling is the same as that in Figure 2.1. Please note that different color scales are used for different depth levels.

density (ρ), and radial shear wave anisotropy $\xi = \frac{(V_{SH}-V_{SV})}{V_S}$ of the final model compared against the initial model are presented in Figure 2.11, where V_S is the Voigt-Reuss-Hill average shear wave velocity, computed from SV and SH velocities as $V_S = \sqrt{\frac{(2V_{SV}^2+V_{SH}^2)}{3}}$ (Panning and Romanowicz, 2006). The average density does not change significantly from the initial model because the density is generally difficult to be constrained by seismic data within the period range of this study (e.g., Blom et al., 2017).

The final tomographic model is presented in Figures 2.12-2.14 at constant depths, shown as the absolute isotropic S-wave velocities. High-resolution seismic images reveal significant lateral heterogeneities in the crust and mantle. This provides fruitful information about the depth extension of surface geological features and the influence and control of mantle dynamics upon lithospheric processes such as mountain building, seismogenesis, and volcanism. The radial anisotropy parameter $\xi = (V_{SH} - V_{SV})/V_S$ is the relative seismic wave velocity difference between horizontally (SH) and vertically (SV) polarized shear waves, which can be treated as an important indicator of whether lithospheric deformation in the crust and mantle or mantle flow in the asthenosphere is dominant in either the horizontal direction (positive ξ, $V_{SH} > V_{SV}$) or the vertical direction (negative ξ, $V_{SV} > V_{SH}$) or (e.g., Fichtner et al., 2010; Zhu et al., 2017). The geologic/tectonic interpretation guided by seismic velocity and radial anisotropy is work in progress and will be presented in subsequent publications.

The model not only confirms well-established features but also exhibits sharper and more detailed shear wave velocity anomalies (Figures S6-S10). Within the depth range of the lithosphere, the sharp transition from high-velocity to low-velocity anomalies clearly marks plate boundaries among the Eurasian Plate, Indo-Australian Plate, Philippine Sea Plate, Pacific Plate, and tectonic boundaries between the Tarim Basin and the Tibetan Plateau, the Sichuan Basin and the Chuandian Block, and the North China Block and the South China Block (Figure 2.12). The large-scale low-velocity anomalies beneath the Tibetan Plateau are roughly bounded by the Tarim Basin in the northwest, Ordos and Sichuan Basins in the east, the Alxa Block in the north, and the north margin of the Indian Plate in the south (Figure 2.12; e.g., Shen et al., 2016; Han et al., 2021). The Indian Plate has subducted down to 250-300 km depth underneath the Tibetan Plateau, with the northern frontal edge of the Indian slab reaching the Songpan Ganzi Fold Belt (Figures 2.12 and 2.13). The western Pacific slab, imaged as a high-velocity zone, is subducting beneath the Eurasian Plate from Kuril trench, Japan trench, Izu-Bonin trench, and Mariana trench down to the deep mantle (Figures 2.12 and 2.13; e.g., Huang and Zhao, 2006; Li et al., 2008; Li and van der Hilst, 2010; Chen et al., 2015; Tao et al., 2018). The Philippine Sea and Caroline plates are characterized by conspicuous high-velocity anomalies in the lithosphere to a depth of $\sim$ 90 km (Figure 2.12), underlain by the low-velocity zone (generally referred to as the asthenosphere; e.g., Barrell, 1914) in the upper mantle (Figures 2.12 and 2.13).

Below the base of the lithosphere, our results exhibit notable widespread asthenosphere with a thickness of $\sim$100 km in East and Southeast Asia, bounded by subduction trenches (Kurile, Japan, Ryukyu, Philippine, Timor, Java, Sumatra, Andaman, Arakan), the Ordos Block and Sichuan Basin (Figures 2.12 and 2.13). Under the Stanovoy Range and north

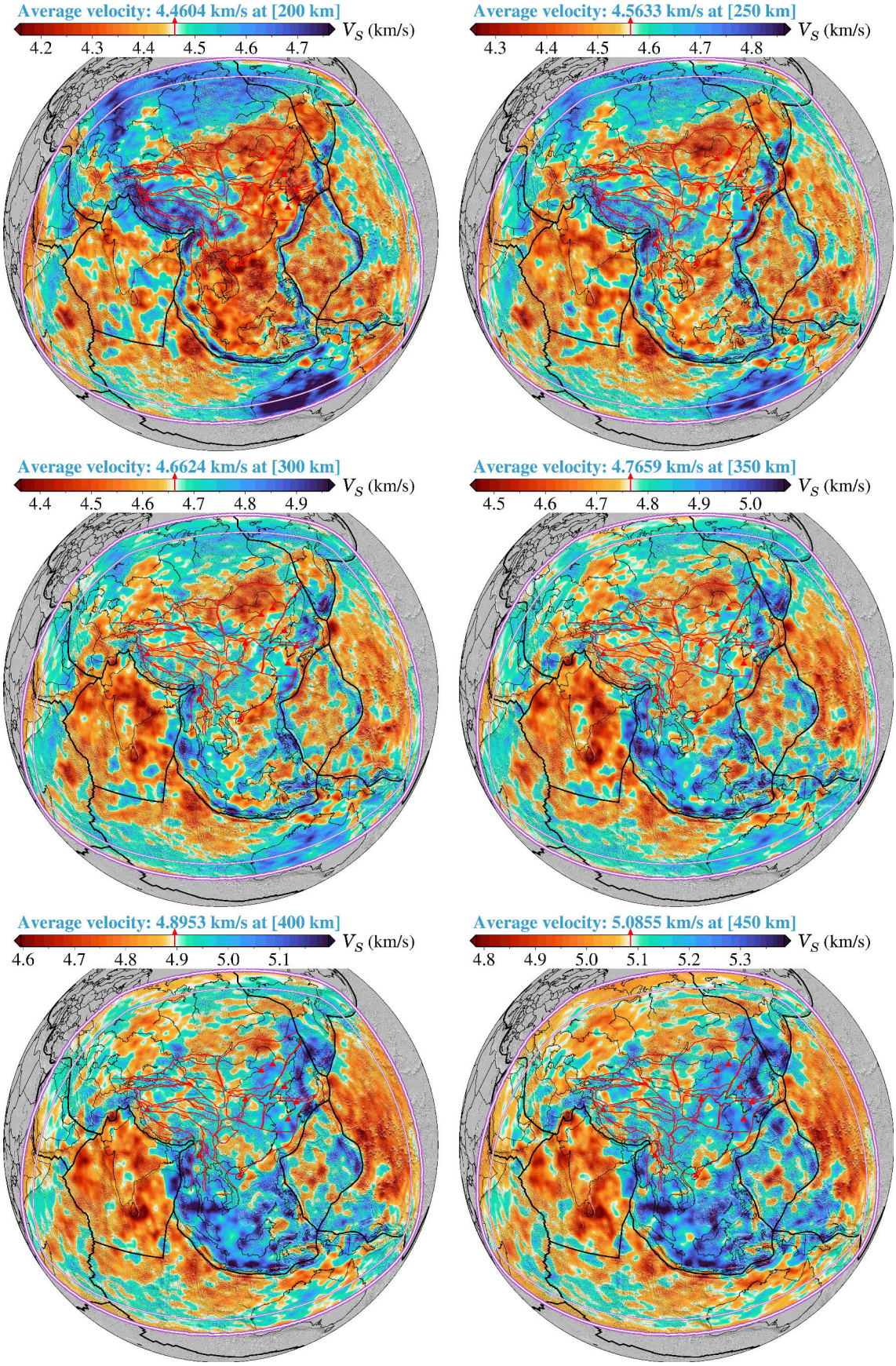

Figure 2.13: Horizontal slices through the final tomographic model showing the absolute isotropic V_S for the lowermost upper mantle, mantle transition zone, and uppermost lower mantle at various depths. The depth of each layer is shown on the top of each map. The other labeling is the same as that in Figure 2.12. Please note that different color scales are used for different depth levels.

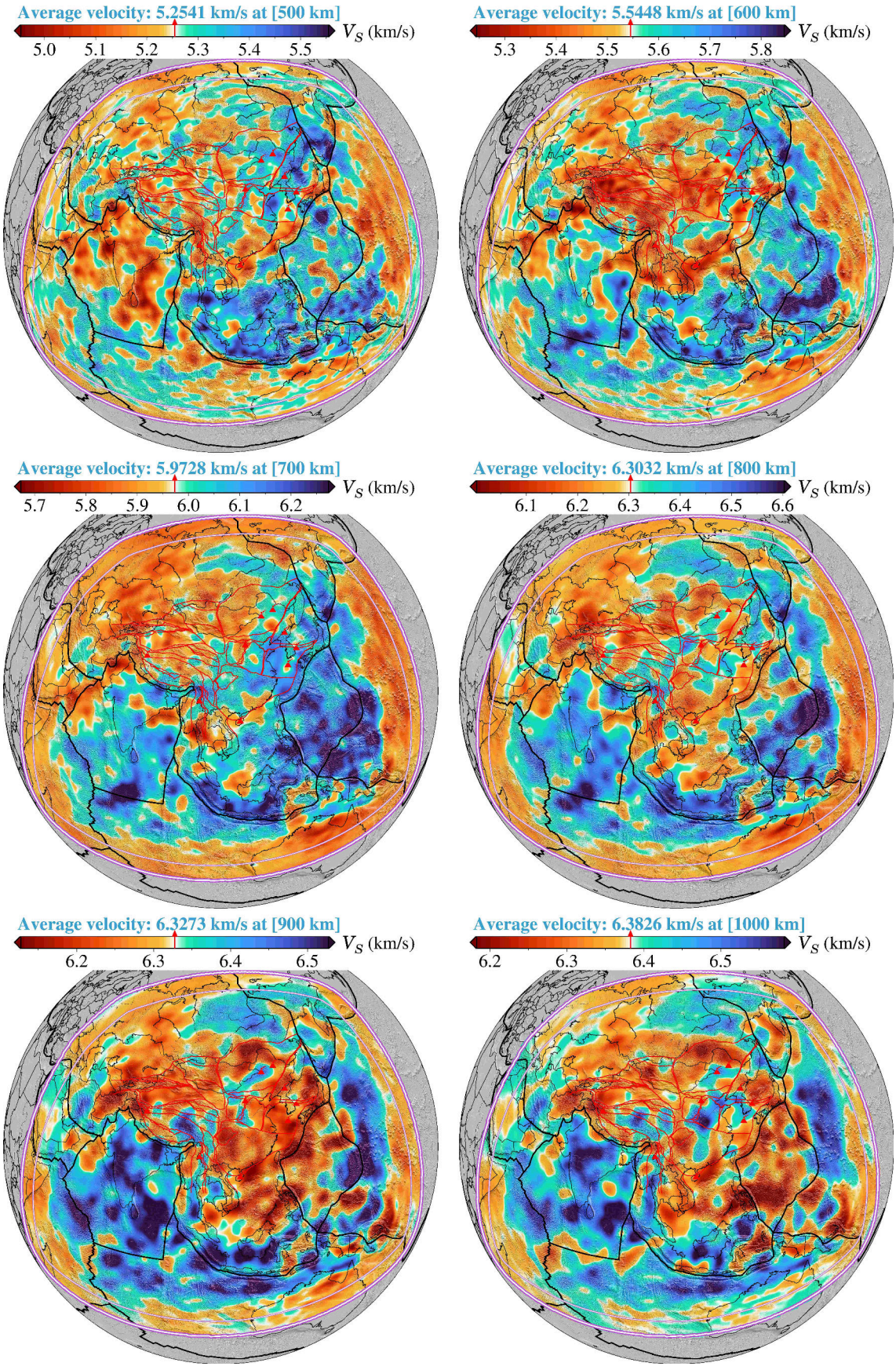

Figure 2.14: Horizontal slices through the final tomographic model showing the absolute isotropic V_S for the lower mantle down to 1,000 km depth at various depths. The depth of each layer is shown on the top of each map. The other labeling is the same as that in Figure 2.12. Please note that different color scales are used for different depth levels.

part of Northeast China, the low-velocity anomalies are still prominent down to the top of the mantle transition zone (MTZ; Figures 2.12 and 2.13). The strong low-velocity bodies correlated with the Altay-Sayan Mountain Range continuously extend from the crust to the uppermost mantle (Figures 2.12 and 2.13). The active intraplate volcanic areas in East Asia (such as Wudalianchi, Arxan, Jingpo Lake, Changbai, Datong, Ulleung, Jeju, Tengchong) are underlain by significant low-velocity anomalies in the upper mantle (Figures 2.12 and 2.13). Beneath the Indo-Australian Plate, we observe distinct low-velocity anomalies from a depth of ∼200 km to the bottom of the MTZ, continuously extending northward below western China from the lower MTZ to the top of the lower mantle (Figures 2.13 and 2.14).

Southeast Asia, as one of the most complex tectonic regions on Earth, is currently surrounded by strongly curved subduction zones. One dominant feature in our images is the high-velocity zones around Southeast Asia (Figures 2.12 and 2.13), which generally represent the subducting slabs, such as the Burma slab under Southeast Tibet, the Australian slab under Sumatra and Java, the Philippine Sea slab under the Philippines, and the Molucca Sea slabs under the eastern Indonesia. Our results reveal clearly subhorizontal high-velocity anomalies in and around the MTZ (Figure 2.13), which have been well identified from previous tomographic studies but there has been little agreement on their origin (e.g., Hall and Spakman, 2015; Obayashi et al., 2013). Narrow ENE striking high-velocity anomalies appear from the top of the MTZ down to a depth of 900 km beneath the Caroline Plate (Figures 2.13 and 2.14), suggesting that ancient continental or oceanic lithosphere resides inside the MTZ, penetrates the 660-km discontinuity and sinks into the lower mantle, possibly corresponding to different episodes of the slab subduction. Significant high-velocity anomalies are visible in the uppermost lower mantle beneath the north of the Indo-Australian Plate (Figure 2.14), which may represent fragments of the late Mesozoic Tethyan slab subducted before the India-Eurasia collision (e.g., Nerlich et al., 2016).

2.7 Conclusions

We conducted a 3-D full-waveform inversion for the crust-mantle structure beneath China and adjacent regions based on numerical forward and adjoint simulations of anelastic seismic wave propagation with the shortest period of 30 s. New model ***SinoScope 1.0*** reveals high-velocity anomalies in the upper mantle beneath major subduction zones and three stable blocks (Ordos, Sichuan, and Tarim basins) and low-velocity anomalies beneath Holocene volcanoes, back-arc regions of ongoing subductions, and India-Eurasia collision zone, which are generally viewed as well-established features of the broad Asian region (e.g., Huang and Zhao, 2006; Li and van der Hilst, 2010; Chen et al., 2015, 2017; Tao et al., 2018). It can further advance our understanding of the tectonic evolution, plate subductions, and mantle dynamics in the broad Asian region. Furthermore, ***SinoScope 1.0*** will be employed to estimate the present-day mantle heterogeneity state to retrodict the history of mantle flow and dynamic topography in the subsequent works, building upon our previous works presented by Colli et al. (2018) and Ghelichkhan et al. (2021).

The ∼0.53 million 60-minute three-component seismograms from 410 earthquakes recorded at 2,427 seismic stations were employed in three successively broadened period bands of 70 - 120 s, 50 - 120 s, and 30 - 120 s, resulting in the assimilation of more than 10 million time windows throughout the inversion's three stages. ***SinoScope 1.0*** is simultaneously constrained by three-component long-period surface waves and short-period body waves and updated by the non-linear minimization of time-frequency domain phase misfits, bringing out numerous small-scale features not observed in previous tomography models. To judge the quality of the model, we performed a validation test with a few earthquakes not used in the construction of the model to demonstrate that it provides significant improvements in phase and amplitude fits compared to the initial model. In addition, we conducted a detailed resolution analysis before interpreting the final model and its features.

Given the rapidly growing volume of seismological waveform data released by various international seismic networks, advances in computational power and numerical optimization routines have enabled the possibility of tackling finer-scale and more complex tomography problems in the coming future. This will undoubtedly drive more work to produce the second-generation full-waveform tomographic model (***SinoScope 2.0***), especially motivated by the deployment of a large-scale broadband seismic array (ChinArray, `http://www.chinarraydmc.cn`), which densely covers the entire mainland China and is spaced ∼35–40 km apart on average. Evident future work needs to assimilate the quick-growing earthquake database recorded by a few seismic networks not available now, for example, ChinArray, Russian Seismic Network, Mongolian Seismic Network, Indian Seismic Network, Indonesian Seismic Network, Pacific Array (`http://eri-ndc.eri.u-tokyo.ac.jp/PacificArray/`), and reduce the shortest simulation period further from 30 to 10 s, or lower in order to more sufficiently constrain physical properties of the Earth's interior and further improve resolution without producing local artifacts.

2.8 Data Availability Statement

The free software GMT Wessel et al. (2013) is used for making most of the figures. The 3-D renderings of the visualizations (Figures 2.7 and 2.10) are generated using ParaView software Ayachit (2015). Source parameters adopted in the wavefield simulations were extracted from the GCMT catalog (`https://www.globalcmt.org/CMTsearch.html`). The anisotropic seismic tomography model presented in this study (which we call ***SinoScope 1.0***) and the waveform data for this research are available on the Zenodo repository: `https://doi.org/10.5281/zenodo.6597380` Ma et al. (2022).

2.9 Acknowledgement

The authors the Data Management Center of China National Seismic Network (`http://www.seisdmc.ac.cn`), the Full Range Seismograph Network of Japan (F-net, `http://www.fnet.bosai.go.jp`), the National Seismograph Network of South Korea and the

IRIS Data Management Center (http://ds.iris.edu/ds/nodes/dmc/) for providing the high-quality waveform data used in this study. Specifically, we gratefully acknowledge the Gauss Center for Supercomputing e.V. (www.gauss-centre.eu) for funding this project by providing computing time on the GCS Supercomputer SuperMUC-NG at Leibniz Supercomputing Center (www.lrz.de) and support from the Swiss National Supercomputing Center (CSCS) in the form of computing time grants s1040. J. Ma and T. Liu acknowledge the financial support from the China Scholarship Council. S. Thrastarson and D. -P. van Herwaarden were supported by the European Unions Horizon 2020 research and innovation program through an ERC Starting Grant (The Collaborative Seismic Earth Model, Grant No. 714069). Y. Tian was supported by the grant from the National Natural Science Foundation of China (Grant No. 41874049). S.-J. Chang was supported by the Korea Meteorological Administration Research and Development Program under Grant KMI 2022-00810, by the National Research Foundation of Korea (NRF) grant funded by the Korean government (MSIT) (2019R1A2C208506111), and by Basic Science Research Program through the NRF funded by the Ministry of Education (No. 2019R1A6A1A03033167). We would also like to thank Christian Böhm, Lion Krischer, and Michael Afanasiev for fruitful discussions. Many thanks also to Jens Oeser for building an excellent computing infrastructure at the Institute of Geophysics at LMU München, without which it is impossible to perform one single numerical simulation. We are very grateful to Michael Bostock (the Editor), Jiaqi Li, and an anonymous reviewer for their constructive comments and suggestions that improved the manuscript. Open Access funding enabled and organized by Projekt DEAL.

2.10 Authorship contribution statement

Jincheng Ma: Conceptualization, Data processing, Tomographic inversions, Visualization, Writing - Original draft.
Hans-Peter Bunge and Andreas Fichtner: Supervision, Writing - Review
Solvi Thrastarson, Dirk-Philip van Herwaarden, You Tian, Sung-Joon Chang, and Tingting Liu: Interpretations and Preparation of the manuscript

2.11 Appendix: Supplementary Figures

Contents of this file
Figures S1 - S10

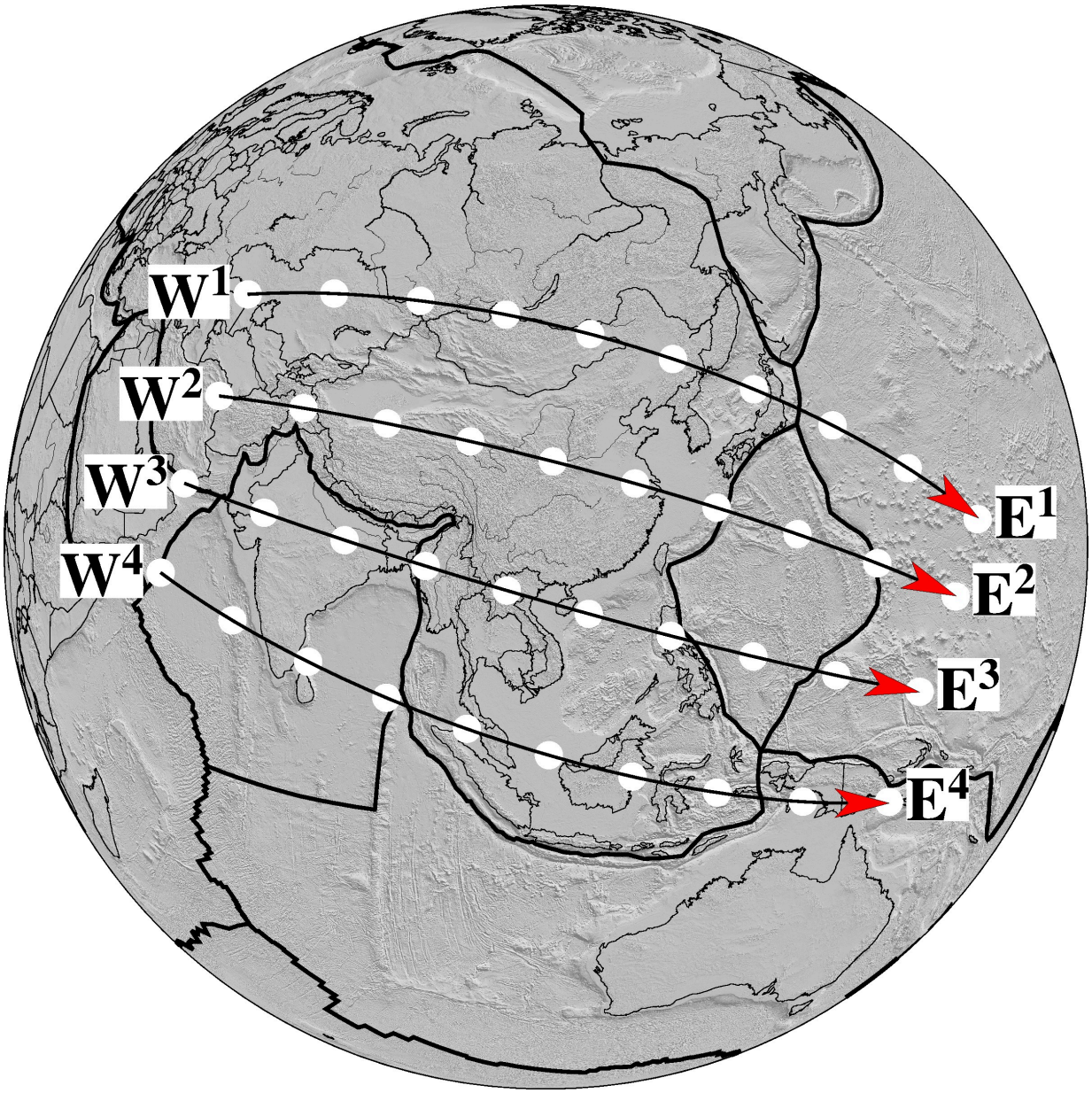

Figure 2.S1: Topographic map showing the locations of the vertical cross-sections in Figures 2.S2 - 2.S5. White dots along the lines are marked every 10°.

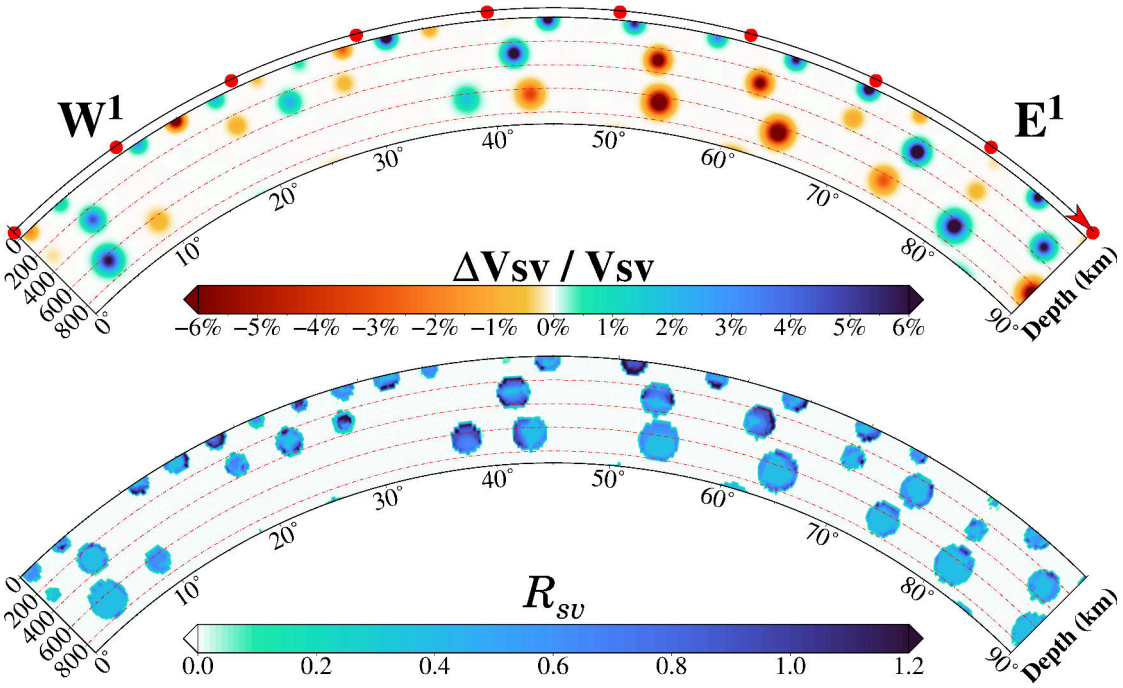

Figure 2.S2: (top): Input $\delta \boldsymbol{m}$ for Gaussian V_{SV} perturbations (δV_{SV}) along the profile W1-E1; (bottom): The degree of repairment for the input perturbations with respect to V_{SV}. Red dots along the lines are marked every 10°.

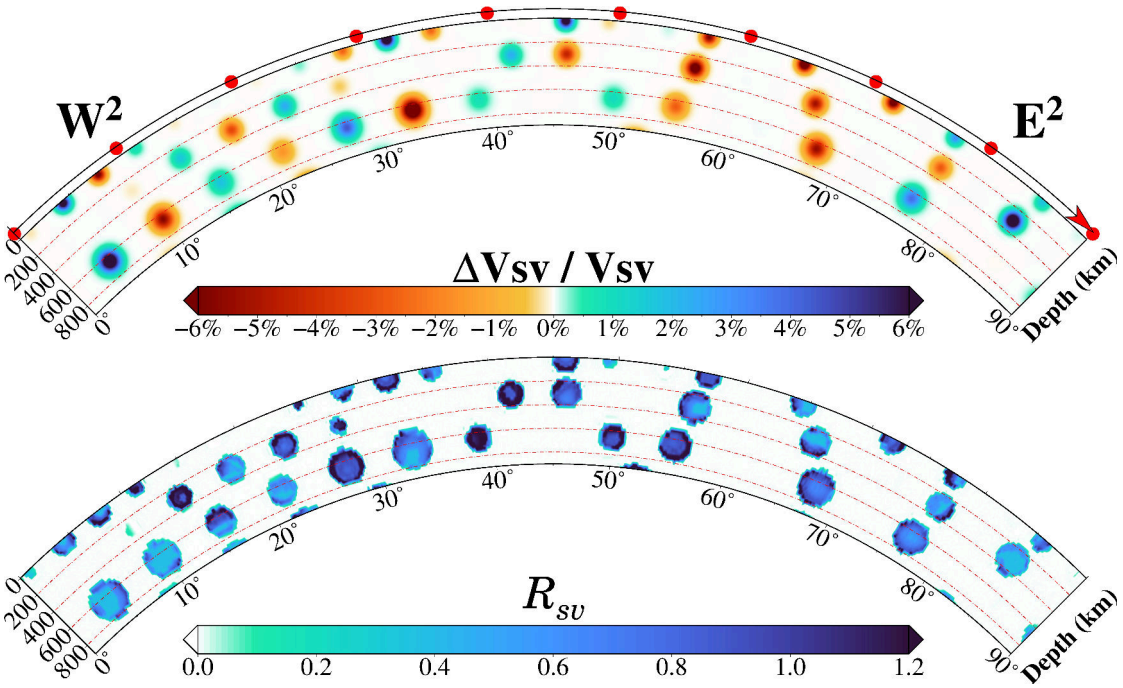

Figure 2.S3: (top): Input $\delta \boldsymbol{m}$ for Gaussian V_{SV} perturbations (δV_{SV}) along the profile W2-E2; (bottom): The degree of repairment for the input perturbations with respect to V_{SV}. Red dots along the lines are marked every 10°.

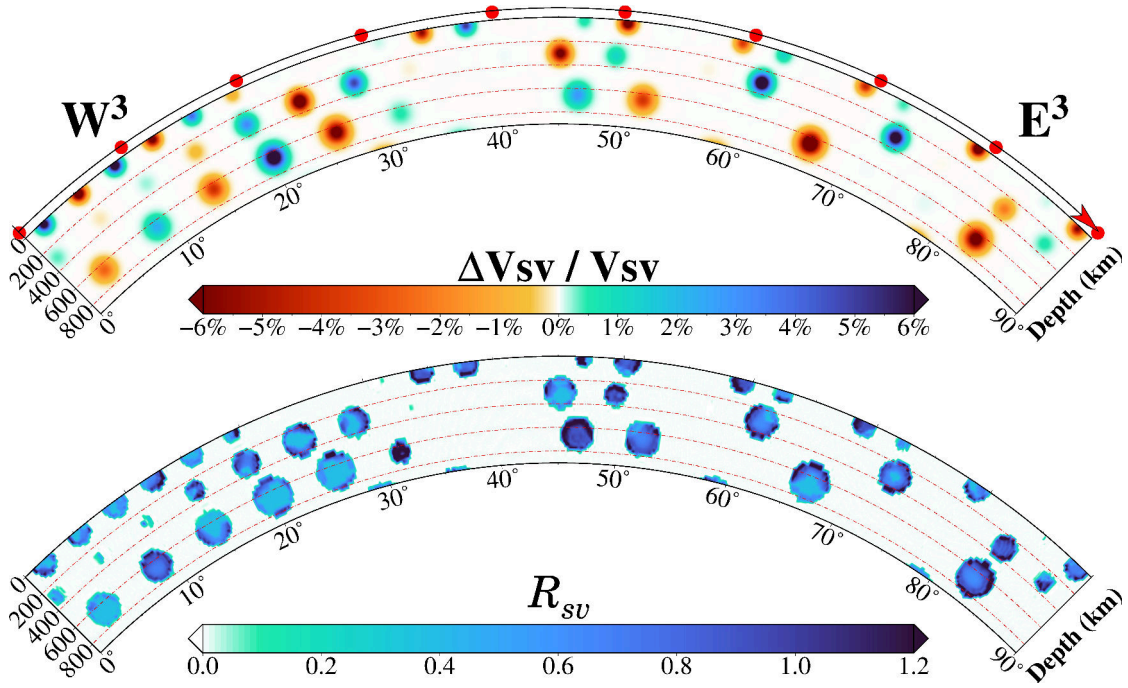

Figure 2.S4: (top): Input $\delta \boldsymbol{m}$ for Gaussian V_{SV} perturbations (δV_{SV}) along the profile W3-E3; (bottom): The degree of repairment for the input perturbations with respect to V_{SV}. Red dots along the lines are marked every 10°.

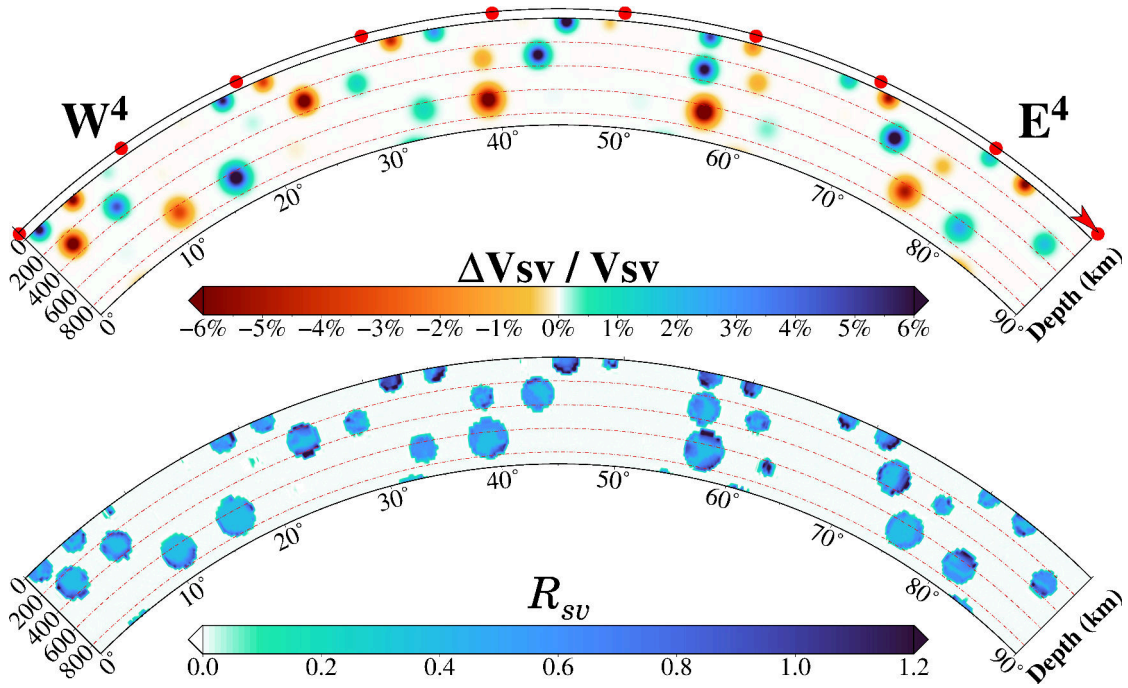

Figure 2.S5: (top): Input $\delta \boldsymbol{m}$ for Gaussian V_{SV} perturbations (δV_{SV}) along the profile W4-E4; (bottom): The degree of repairment for the input perturbations with respect to V_{SV}. Red dots along the lines are marked every 10°.

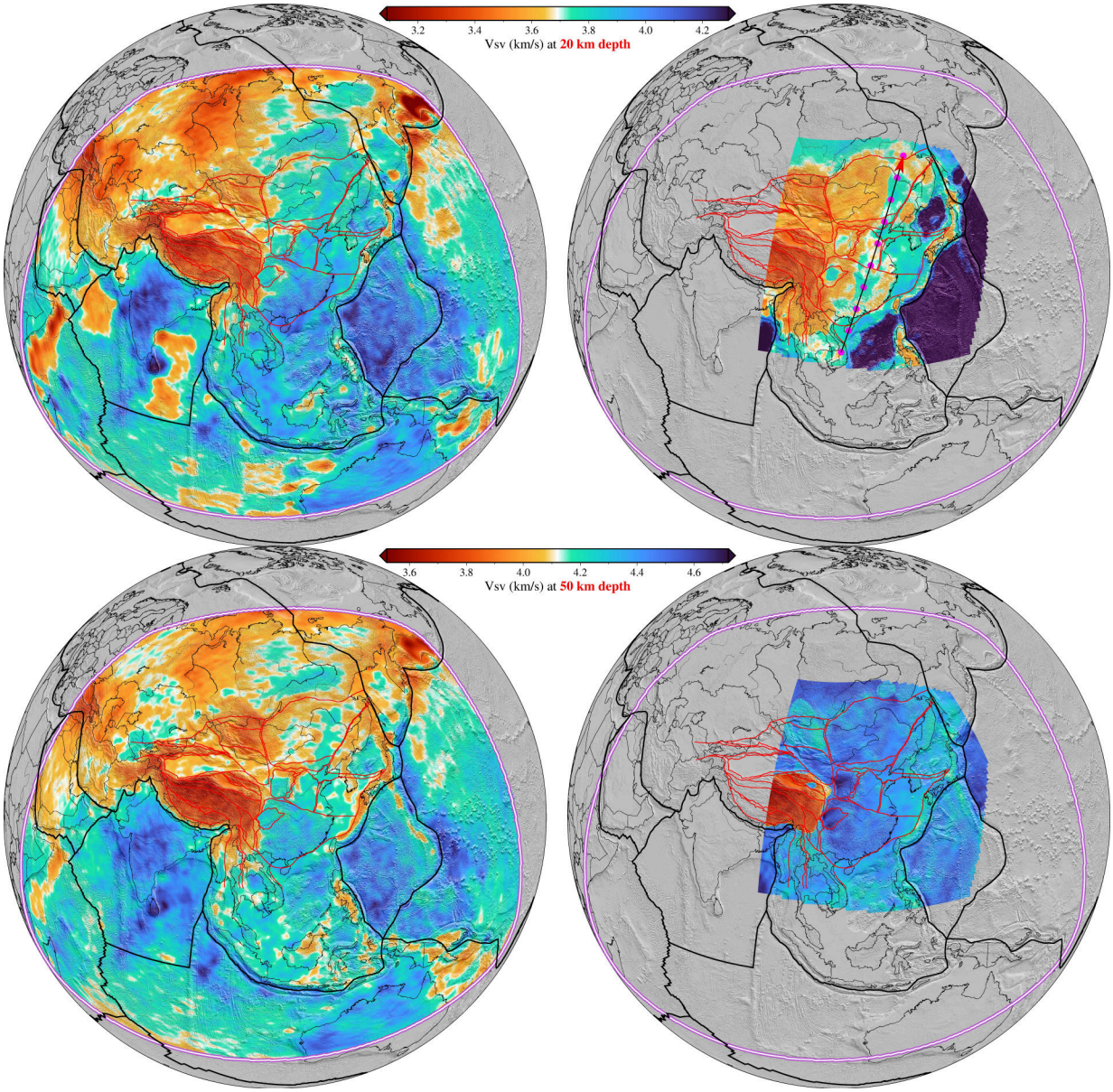

Figure 2.S6: Comparison between (left column) ***SinoScope 1.0*** and (right column) FWEA18 (Tao et al., 2018). Please note that same color scales are used for different tomographic models at various depths. Location of the cross section (top right) for which vertical profile is shown in Figures 2.S9. Magenta dots along the lines are marked every 5°.

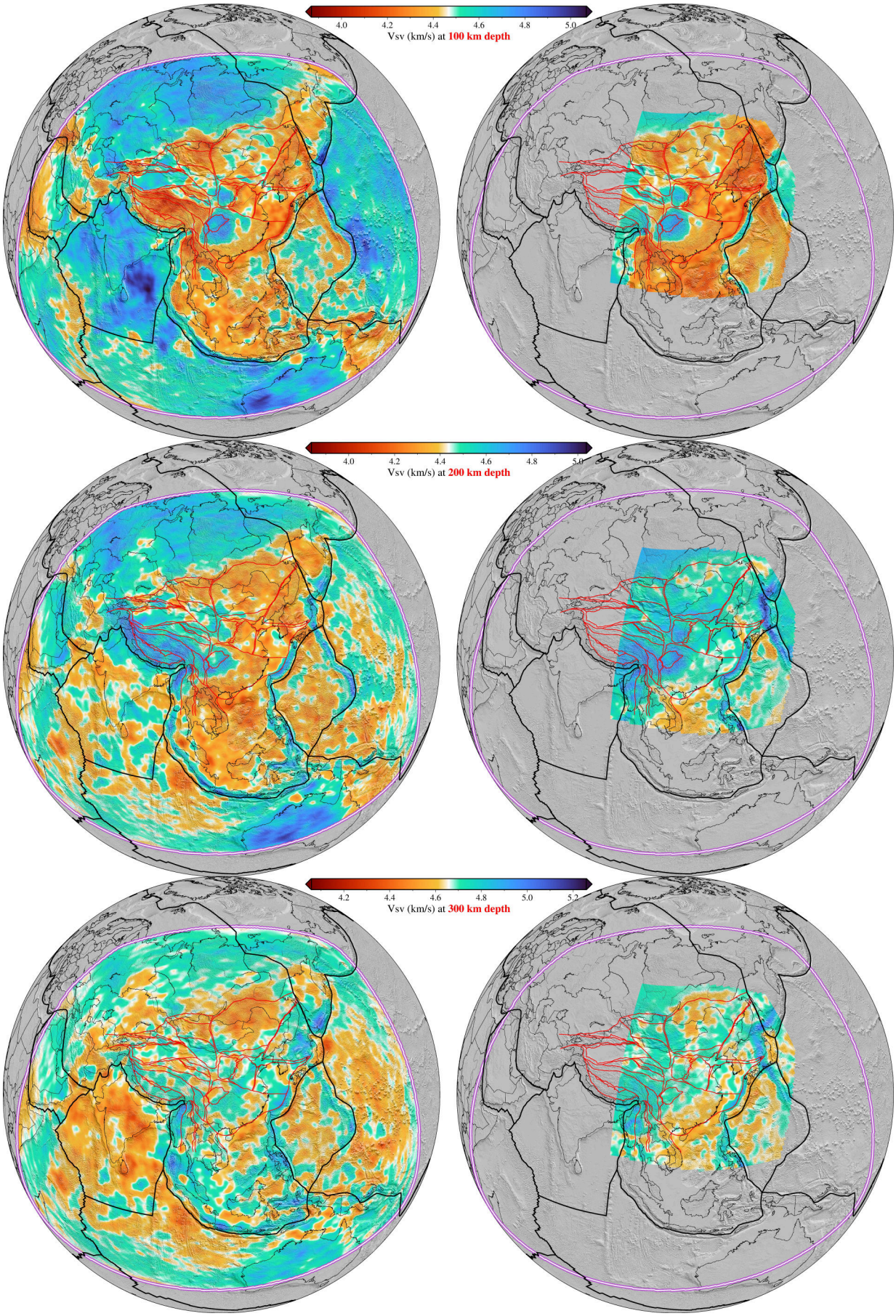

Figure 2.S7: Comparison between (left column) ***SinoScope 1.0*** and (right column) FWEA18 (Tao et al., 2018). Please note that same color scales are used for different tomographic models at various depths.

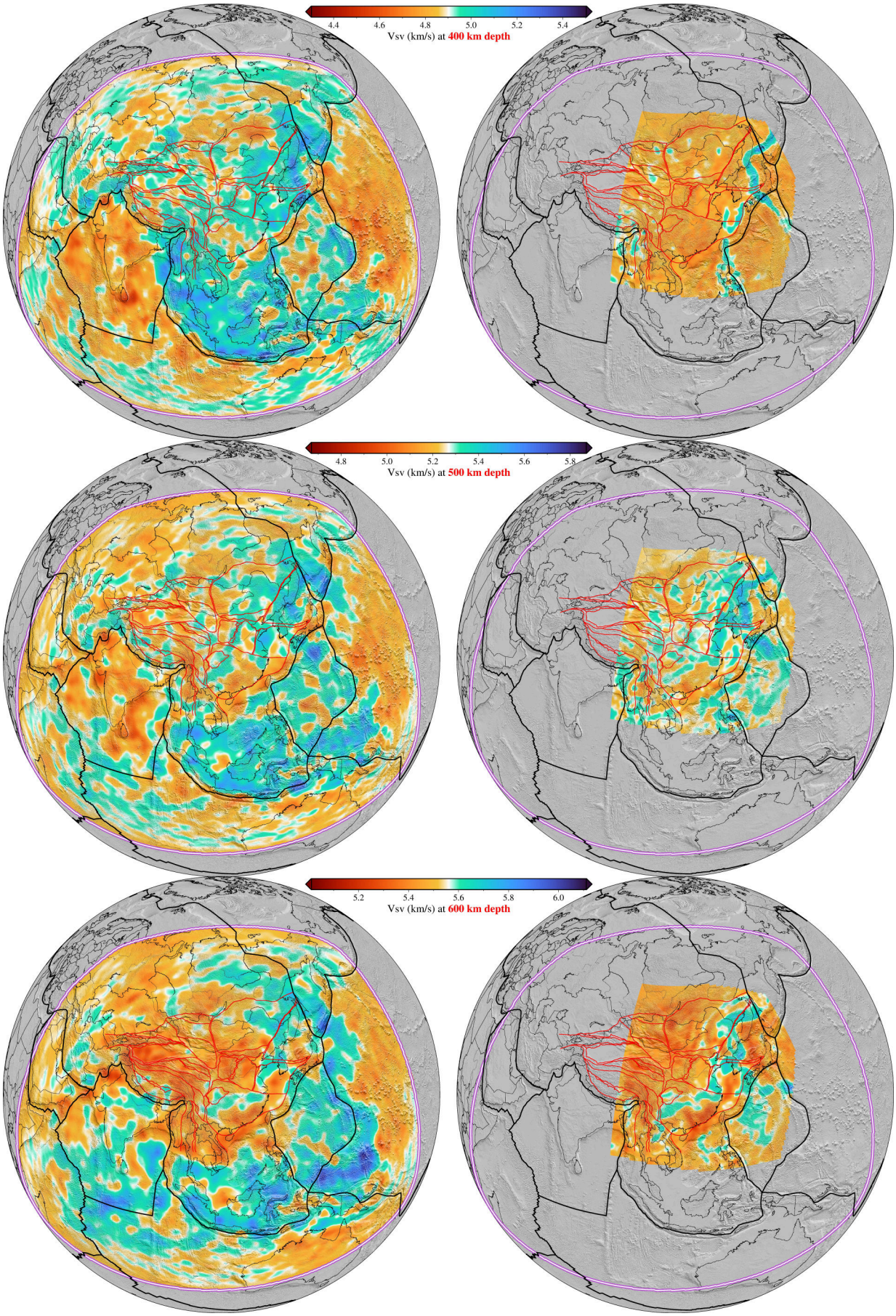

Figure 2.S8: Comparison between (left column) ***SinoScope 1.0*** and (right column) FWEA18 (Tao et al., 2018). Please note that same color scales are used for different tomographic models at various depths.

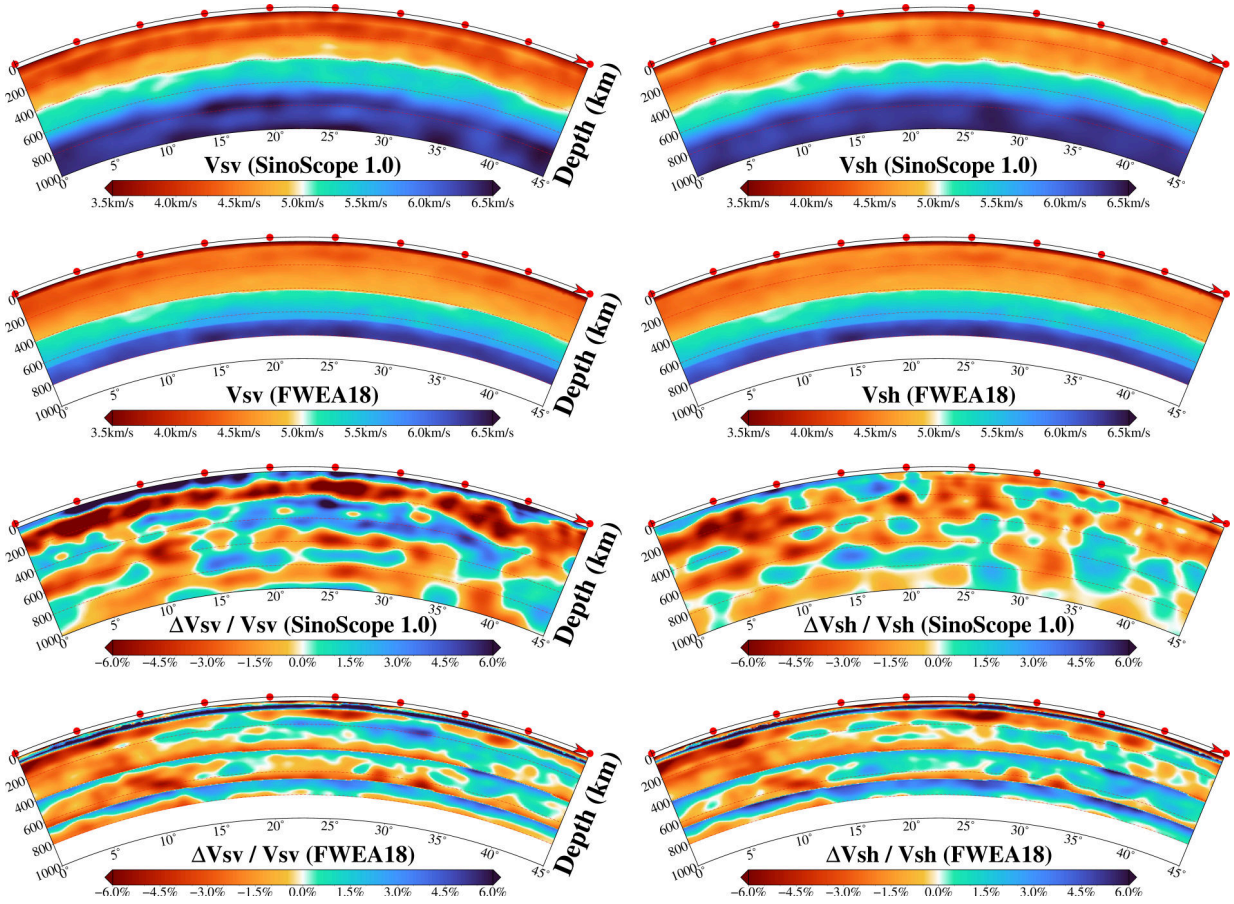

Figure 2.S9: Comparison between ***SinoScope 1.0*** and FWEA18 (Tao et al., 2018) for a north-south cross-section along the profile shown in Figure 2.S6. Perturbations (δlnV_{SV} and δlnV_{SH}) are in % relative to the depth-average from ***SinoScope 1.0***.

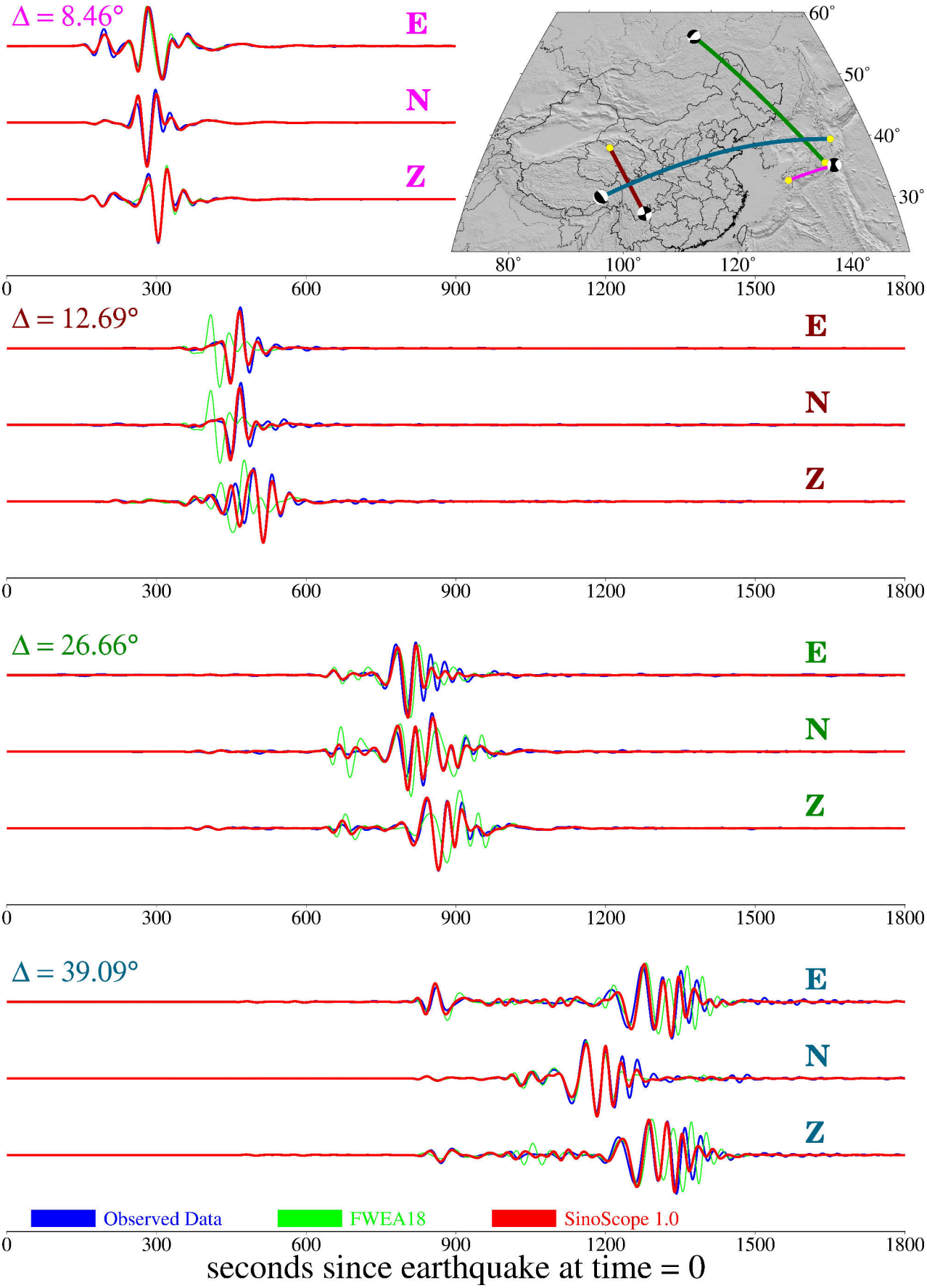

Figure 2.S10: Exemplary waveform comparisons of synthetics through ***SinoScope 1.0*** and FWEA18 (Tao et al., 2018) simulated at a dominant period of 30 s against observed data. Amplitudes are not scaled.

Reference

Afanasiev, M., Boehm, C., van Driel, M., Krischer, L., Rietmann, M., May, D. A., Knepley, M. G. and Fichtner, A. (2019). Modular and flexible spectral-element waveform modelling in two and three dimensions, *Geophysical Journal International* **216**(3): 1675–1692.
URL: *https://doi.org/10.1093/gji/ggy469*

Afanasiev, M., Peter, D., Sager, K., Simutė, S., Ermert, L., Krischer, L. and Fichtner, A. (2016). Foundations for a multiscale collaborative Earth model, *Geophysical Journal International* **204**(1): 39–58.
URL: *https://doi.org/10.1093/gji/ggv439*

Aki, K., Christoffersson, A. and Husebye, E. S. (1977). Determination of the three-dimensional seismic structure of the lithosphere, *Journal of Geophysical Research (1896-1977)* **82**(2): 277–296.
URL: *https://agupubs.onlinelibrary.wiley.com/doi/abs/10.1029/JB082i002p00277*

Aki, K. and Lee, W. H. K. (1976). Determination of three-dimensional velocity anomalies under a seismic array using first p arrival times from local earthquakes: 1. a homogeneous initial model, *Journal of Geophysical Research (1896-1977)* **81**(23): 4381–4399.
URL: *https://agupubs.onlinelibrary.wiley.com/doi/abs/10.1029/JB081i023p04381*

Ayachit, U. (2015). *The ParaView Guide: A Parallel Visualization Application*, Kitware, Inc., Clifton Park, NY, USA.

Backus, G. E. and Gilbert, J. F. (1967). Numerical Applications of a Formalism for Geophysical Inverse Problems, *Geophysical Journal International* **13**(1-3): 247–276.
URL: *https://doi.org/10.1111/j.1365-246X.1967.tb02159.x*

Barrell, J. (1914). The strength of the earth's crust, *The Journal of Geology* **22**(7): 655–683.
URL: *https://doi.org/10.1086/622181*

Bird, P. (2003). An updated digital model of plate boundaries, *Geochemistry, Geophysics, Geosystems* **4**(3).
URL: *https://agupubs.onlinelibrary.wiley.com/doi/abs/10.1029/2001GC000252*

Blom, N., Boehm, C. and Fichtner, A. (2017). Synthetic inversions for density using seismic and gravity data, *Geophysical Journal International* **209**(2): 1204–1220.
URL: *https://doi.org/10.1093/gji/ggx076*

Boehm, C., Korta Martiartu, N., Vinard, N., Jovanović Balic, I. and Fichtner, A. (2018). Time-domain spectral-element ultrasound waveform tomography using a stochastic quasi-Newton method, *Medical Imaging 2018: Ultrasonic Imaging and Tomography*, Vol.

10580 of *Society of Photo-Optical Instrumentation Engineers (SPIE) Conference Series*, p. 105800H.

Bozdağ, E., Peter, D., Lefebvre, M., Komatitsch, D., Tromp, J., Hill, J., Podhorszki, N. and Pugmire, D. (2016). Global adjoint tomography: first-generation model, *Geophysical Journal International* **207**(3): 1739–1766.
URL: *https://doi.org/10.1093/gji/ggw356*

Bunks, C., Saleck, F. M., Zaleski, S. and Chavent, G. (1995). Multiscale seismic waveform inversion, *Geophysics* **60**(5): 1457–1473.
URL: *https://doi.org/10.1190/1.1443880*

Chen, M., Niu, F., Liu, Q., Tromp, J. and Zheng, X. (2015). Multiparameter adjoint tomography of the crust and upper mantle beneath east asia: 1. model construction and comparisons, *Journal of Geophysical Research: Solid Earth* **120**(3): 1762–1786.
URL: *https://agupubs.onlinelibrary.wiley.com/doi/abs/10.1002/2014JB011638*

Chen, M., Niu, F., Tromp, J., Lenardic, A., Lee, C.-T. A., Cao, W. and Ribeiro, J. (2017). Lithospheric foundering and underthrusting imaged beneath tibet, *Nature communications* **8**(1): 1–10.

Colli, L., Fichtner, A. and Bunge, H.-P. (2013). Full waveform tomography of the upper mantle in the south atlantic region: Imaging a westward fluxing shallow asthenosphere?, *Tectonophysics* **604**: 26–40. Progress in understanding the South Atlantic margins.
URL: *https://www.sciencedirect.com/science/article/pii/S0040195113003806*

Colli, L., Ghelichkhan, S., Bunge, H.-P. and Oeser, J. (2018). Retrodictions of Mid Paleogene mantle flow and dynamic topography in the Atlantic region from compressible high resolution adjoint mantle convection models: Sensitivity to deep mantle viscosity and tomographic input model, *Gondwana Research* **53**: 252–272.

Conn, A. R., Gould, N. I. M. and Toint, P. L. (2000). *Trust Region Methods*, Society for Industrial and Applied Mathematics.
URL: *https://epubs.siam.org/doi/abs/10.1137/1.9780898719857*

Dahlen, F. A., Hung, S.-H. and Nolet, G. (2000). Fréchet kernels for finite-frequency traveltimes—I. Theory, *Geophysical Journal International* **141**(1): 157–174.
URL: *https://doi.org/10.1046/j.1365-246X.2000.00070.x*

DeMets, C., Gordon, R. G., Argus, D. F. and Stein, S. (1994). Effect of recent revisions to the geomagnetic reversal time scale on estimates of current plate motions, *Geophysical Research Letters* **21**(20): 2191–2194.
URL: *https://agupubs.onlinelibrary.wiley.com/doi/abs/10.1029/94GL02118*

Dziewonski, A. M. and Anderson, D. L. (1981). Preliminary reference earth model, *Physics of the Earth and Planetary Interiors* **25**(4): 297–356.
URL: *https://www.sciencedirect.com/science/article/pii/0031920181900467*

Dziewonski, A. M., Hager, B. H. and O'Connell, R. J. (1977). Large-scale heterogeneities in the lower mantle, *Journal of Geophysical Research (1896-1977)* **82**(2): 239–255.
URL: *https://agupubs.onlinelibrary.wiley.com/doi/abs/10.1029/JB082i002p00239*

Ekström, G., Nettles, M. and Dziewoński, A. (2012). The global cmt project 2004–2010: Centroid-moment tensors for 13,017 earthquakes, *Physics of the Earth and Planetary Interiors* **200-201**: 1–9.
URL: *https://www.sciencedirect.com/science/article/pii/S0031920112000696*

Fichtner, A. (2011). *Full Seismic Waveform Modelling and Inversion*, Springer, Berlin, Heidelberg.

Fichtner, A., Bunge, H.-P. and Igel, H. (2006). The adjoint method in seismology: I. theory, *Physics of the Earth and Planetary Interiors* **157**(1): 86–104.
URL: *https://www.sciencedirect.com/science/article/pii/S0031920106001051*

Fichtner, A., Kennett, B. L., Igel, H. and Bunge, H.-P. (2010). Full waveform tomography for radially anisotropic structure: New insights into present and past states of the australasian upper mantle, *Earth and Planetary Science Letters* **290**(3): 270–280.
URL: *https://www.sciencedirect.com/science/article/pii/S0012821X09007262*

Fichtner, A., Kennett, B. L. N., Igel, H. and Bunge, H.-P. (2008). Theoretical background for continental- and global-scale full-waveform inversion in the time–frequency domain, *Geophysical Journal International* **175**(2): 665–685.
URL: *https://doi.org/10.1111/j.1365-246X.2008.03923.x*

Fichtner, A., Kennett, B. L. N., Igel, H. and Bunge, H.-P. (2009). Full seismic waveform tomography for upper-mantle structure in the australasian region using adjoint methods, *Geophysical Journal International* **179**(3): 1703–1725.
URL: *https://onlinelibrary.wiley.com/doi/abs/10.1111/j.1365-246X.2009.04368.x*

Fichtner, A. and Trampert, J. (2011a). Hessian kernels of seismic data functionals based upon adjoint techniques, *Geophysical Journal International* **185**(2): 775–798.
URL: *https://doi.org/10.1111/j.1365-246X.2011.04966.x*

Fichtner, A. and Trampert, J. (2011b). Resolution analysis in full waveform inversion, *Geophysical Journal International* **187**(3): 1604–1624.
URL: *https://doi.org/10.1111/j.1365-246X.2011.05218.x*

Fichtner, A., van Herwaarden, D.-P., Afanasiev, M., Simutė, S., Krischer, L., Çubuk Sabuncu, Y., Taymaz, T., Colli, L., Saygin, E., Villaseñor, A., Trampert, J., Cupillard, P., Bunge, H.-P. and Igel, H. (2018). The collaborative seismic earth model: Generation 1, *Geophysical Research Letters* **45**(9): 4007–4016.
URL: *https://agupubs.onlinelibrary.wiley.com/doi/abs/10.1029/2018GL077338*

French, S. W. and Romanowicz, B. A. (2014). Whole-mantle radially anisotropic shear velocity structure from spectral-element waveform tomography, *Geophysical Journal International* **199**(3): 1303–1327.
URL: *https://doi.org/10.1093/gji/ggu334*

Ghelichkhan, S., Bunge, H.-P. and Oeser, J. (2021). Global mantle flow retrodictions for the early Cenozoic using an adjoint method: evolving dynamic topographies, deep mantle structures, flow trajectories and sublithospheric stresses, *Geophysical Journal International* **226**(2): 1432–1460.
URL: *https://doi.org/10.1093/gji/ggab108*

Gokhberg, A. and Fichtner, A. (2016). Full-waveform inversion on heterogeneous hpc systems, *Computers & Geosciences* **89**: 260–268.
URL: *https://www.sciencedirect.com/science/article/pii/S0098300415301035*

Grand, S., van der Hilst, R. and Widiyantoro, S. (1997). Global seismic tomography: A snapshot of convection in the earth, *Geol. Soc. Am. TODAY* **7**: 1–7.

Hall, R. (2011). Australia–se asia collision: plate tectonics and crustal flow. the se asian gateway: history and tectonics, *Geological Society of London Special Publications* **355**: 75–109.

Hall, R. and Spakman, W. (2015). Mantle structure and tectonic history of se asia, *Tectonophysics* **658**: 14–45.
URL: *https://www.sciencedirect.com/science/article/pii/S0040195115003698*

Han, S., Zhang, H., Xin, H., Shen, W. and Yao, H. (2021). USTClitho2.0: Updated Unified Seismic Tomography Models for Continental China Lithosphere from Joint Inversion of Body-Wave Arrival Times and Surface-Wave Dispersion Data, *Seismological Research Letters* **93**(1): 201–215.
URL: *https://doi.org/10.1785/0220210122*

Hayes, G. P., Moore, G. L., Portner, D. E., Hearne, M., Flamme, H., Furtney, M. and Smoczyk, G. M. (2018). Slab2, a comprehensive subduction zone geometry model, *Science* **362**(6410): 58–61.
URL: *https://www.science.org/doi/abs/10.1126/science.aat4723*

Hosseini, K., Sigloch, K., Tsekhmistrenko, M., Zaheri, A., Nissen-Meyer, T. and Igel, H. (2020). Global mantle structure from multifrequency tomography using P, PP and P-diffracted waves, *Geophysical Journal International* **220**(1): 96–141.
URL: *https://doi.org/10.1093/gji/ggz394*

Huang, J. and Zhao, D. (2006). High-resolution mantle tomography of china and surrounding regions, *Journal of Geophysical Research: Solid Earth* **111**(B9).
URL: *https://agupubs.onlinelibrary.wiley.com/doi/abs/10.1029/2005JB004066*

Humphreys, E. and Clayton, R. W. (1988). Adaptation of back projection tomography to seismic travel time problems, *Journal of Geophysical Research: Solid Earth* **93**(B2): 1073–1085.
URL: *https://agupubs.onlinelibrary.wiley.com/doi/abs/10.1029/JB093iB02p01073*

Hung, S.-H., Dahlen, F. and Nolet, G. (2000). Fréchet kernels for finite-frequency traveltimeséII. Examples, *Geophysical Journal International* **141**(1): 175–203.
URL: *https://doi.org/10.1046/j.1365-246X.2000.00072.x*

Igel, H. (2017). *Computational seismology: a practical introduction*, Oxford University Press.

Jolivet, L., Faccenna, C., Becker, T., Tesauro, M., Sternai, P. and Bouilhol, P. (2018). Mantle flow and deforming continents: From india-asia convergence to pacific subduction, *Tectonics* **37**(9): 2887–2914.
URL: *https://agupubs.onlinelibrary.wiley.com/doi/abs/10.1029/2018TC005036*

Kennett, B. L. N. and Fichtner, A. (2020). *Exploiting Seismic Waveforms: Correlation, Heterogeneity and Inversion*, Cambridge University Press.

Komatitsch, D. and Tromp, J. (2002a). Spectral-element simulations of global seismic wave propagation—I. Validation, *Geophysical Journal International* **149**(2): 390–412.
URL: *https://doi.org/10.1046/j.1365-246X.2002.01653.x*

Komatitsch, D. and Tromp, J. (2002b). Spectral-element simulations of global seismic wave propagation—II. Three-dimensional models, oceans, rotation and self-gravitation, *Geophysical Journal International* **150**(1): 303–318.
URL: *https://doi.org/10.1046/j.1365-246X.2002.01716.x*

Kreemer, C., Blewitt, G. and Klein, E. C. (2014). A geodetic plate motion and global strain rate model, *Geochemistry, Geophysics, Geosystems* **15**(10): 3849–3889.
URL: *https://agupubs.onlinelibrary.wiley.com/doi/abs/10.1002/2014GC005407*

Krischer, L., Fichtner, A., Boehm, C. and Igel, H. (2018). Automated large-scale full seismic waveform inversion for north america and the north atlantic, *Journal of Geophysical Research: Solid Earth* **123**(7): 5902–5928.
URL: *https://agupubs.onlinelibrary.wiley.com/doi/abs/10.1029/2017JB015289*

Krischer, L., Megies, T., Barsch, R., Beyreuther, M., Lecocq, T., Caudron, C. and Wassermann, J. (2015). ObsPy: a bridge for seismology into the scientific python ecosystem, *Computational Science & Discovery* **8**(1): 014003.
URL: *https://doi.org/10.1088/1749-4699/8/1/014003*

Krischer, L., Smith, J., Lei, W., Lefebvre, M., Ruan, Y., de Andrade, E. S., Podhorszki, N., Bozdağ, E. and Tromp, J. (2016). An Adaptable Seismic Data Format, *Geophysical Journal International* **207**(2): 1003–1011.
URL: *https://doi.org/10.1093/gji/ggw319*

Kristeková, M., Kristek, J. and Moczo, P. (2009). Time-frequency misfit and goodness-of-fit criteria for quantitative comparison of time signals, *Geophysical Journal International* **178**(2): 813–825.
URL: *https://doi.org/10.1111/j.1365-246X.2009.04177.x*

Kristeková, M., Kristek, J., Moczo, P. and Day, S. M. (2006). Misfit criteria for quantitative comparison of seismograms, *Bulletin of the Seismological Society of America* **96**(5): 1836–1850.
URL: *https://doi.org/10.1785/0120060012*

Lebedev, S. and Nolet, G. (2003). Upper mantle beneath southeast asia from s velocity tomography, *Journal of Geophysical Research* **108**: 2048.

Lei, W., Ruan, Y., Bozdağ, E., Peter, D., Lefebvre, M., Komatitsch, D., Tromp, J., Hill, J., Podhorszki, N. and Pugmire, D. (2020). Global adjoint tomography—model GLAD-M25, *Geophysical Journal International* **223**(1): 1–21.
URL: *https://doi.org/10.1093/gji/ggaa253*

Lekić, V. and Romanowicz, B. (2011). Inferring upper-mantle structure by full waveform tomography with the spectral element method, *Geophysical Journal International* **185**(2): 799–831.
URL: *https://doi.org/10.1111/j.1365-246X.2011.04969.x*

Li, C. and van der Hilst, R. D. (2010). Structure of the upper mantle and transition zone beneath southeast asia from traveltime tomography, *Journal of Geophysical Research: Solid Earth* **115**(B7).
URL: *https://agupubs.onlinelibrary.wiley.com/doi/abs/10.1029/2009JB006882*

Li, C., van der Hilst, R. D., Engdahl, E. R. and Burdick, S. (2008). A new global model for p wave speed variations in earth's mantle, *Geochemistry, Geophysics, Geosystems* **9**(5).
URL: *https://agupubs.onlinelibrary.wiley.com/doi/abs/10.1029/2007GC001806*

Liu, D. C. and Nocedal, J. (1989). On the limited memory bfgs method for large scale optimization, *Mathematical Programming* **45**(1): 503–528.
URL: *https://doi.org/10.1007/BF01589116*

Lévěque, J.-J., Rivera, L. and Wittlinger, G. (1993). On the use of the checker-board test to assess the resolution of tomographic inversions, *Geophysical Journal International* **115**(1): 313–318.
URL: *https://doi.org/10.1111/j.1365-246X.1993.tb05605.x*

Ma, J., Bunge, H.-P., Thrastarson, S., Fichtner, A., van Herwaarden, D. P., Tian, Y., Chang, S.-J. and Liu, T. (2022). Seismic full-waveform inversion of the crust- mantle structure beneath China and adjacent regions, *Journal of Geophysical Research: Solid Earth* .
URL: *https://doi.org/10.5281/zenodo.6597380*

Ma, J., Thrastarson, S., van Herwaarden, D.-P., Fichtner, A. and Bunge, H.-P. (2020). Multiscale Seismic Full-waveform Tomography of the Crust and Mantle beneath China and adjacent regions, *EGU General Assembly Conference Abstracts*, EGU General Assembly Conference Abstracts, p. 2967.

Ma, J., Tian, Y., Zhao, D., Liu, C. and Liu, T. (2019). Mantle dynamics of western pacific and east asia: New insights from p wave anisotropic tomography, *Geochemistry, Geophysics, Geosystems* **20**(7): 3628–3658.
URL: *https://agupubs.onlinelibrary.wiley.com/doi/abs/10.1029/2019GC008373*

Maggi, A., Tape, C., Chen, M., Chao, D. and Tromp, J. (2009). An automated time-window selection algorithm for seismic tomography, *Geophysical Journal International* **178**(1): 257–281.
URL: *https://doi.org/10.1111/j.1365-246X.2009.04099.x*

Matharu, G. and Sacchi, M. (2019). A subsampled truncated-newton method for multiparameter full-waveform inversion, *Geophysics* **84**(3): R333–R340.
URL: *https://doi.org/10.1190/geo2018-0624.1*

Megies, T., Beyreuther, M., Barsch, R., Krischer, L. and Wassermann, J. (2011). ObsPy – what can it do for data centers and observatories?, *Instituto Nazionale di Geofisica e Vulcanologia, INGV* **54**(1).
URL: *https://doi.org/10.4401/ag-4838*

Meier, U., Curtis, A. and Trampert, J. (2007a). Fully nonlinear inversion of fundamental mode surface waves for a global crustal model, *Geophysical Research Letters* **34**: 1–6.

Meier, U., Curtis, A. and Trampert, J. (2007b). Global crustal thickness from neural network inversion of surface wave data, *Geophysical Journal International* **169**(2): 706–722.
URL: *https://doi.org/10.1111/j.1365-246X.2007.03373.x*

Mitchell, D. P. (1991). Spectrally optimal sampling for distribution ray tracing, *Association for Computing Machinery (ACM)* **25**(4): 157–164.
URL: *https://doi.org/10.1145/127719.122736*

Montelli, R., Nolet, G., Dahlen, F. A., Masters, G., Engdahl, E. R. and Hung, S.-H. (2004). Finite-frequency tomography reveals a variety of plumes in the mantle, *Science* **303**(5656): 338–343.
URL: *https://www.science.org/doi/abs/10.1126/science.1092485*

Nerlich, R., Colli, L., Ghelichkhan, S., Schuberth, B. and Bunge, H.-P. (2016). Constraining central neo-tethys ocean reconstructions with mantle convection models, *Geophysical Research Letters* **43**(18): 9595–9603.
URL: *https://agupubs.onlinelibrary.wiley.com/doi/abs/10.1002/2016GL070524*

Nocedal, J. and Wright, S. J. (1999). *Numerical Optimization*, Springer, New York, NY, USA.

Obayashi, M., Yoshimitsu, J., Nolet, G., Fukao, Y., Shiobara, H., Sugioka, H., Miyamachi, H. and Gao, Y. (2013). Finite frequency whole mantle p wave tomography: Improvement of subducted slab images, *Geophysical Research Letters* **40**(21): 5652–5657.
URL: *https://agupubs.onlinelibrary.wiley.com/doi/abs/10.1002/2013GL057401*

Panning, M. and Romanowicz, B. (2006). A three-dimensional radially anisotropic model of shear velocity in the whole mantle, *Geophysical Journal International* **167**(1): 361–379.
URL: *https://doi.org/10.1111/j.1365-246X.2006.03100.x*

Ritsema, J. and van Heijst, H.-J. (2002). Constraints on the correlation of P- and S-wave velocity heterogeneity in the mantle from P, PP, PPP and PKPab traveltimes, *Geophysical Journal International* **149**(2): 482–489.
URL: *https://doi.org/10.1046/j.1365-246X.2002.01631.x*

Ritsema, J., van Heijst, H. J. and Woodhouse, J. H. (1999). Complex shear wave velocity structure imaged beneath africa and iceland, *Science* **286**(5446): 1925–1928.
URL: *https://www.science.org/doi/abs/10.1126/science.286.5446.1925*

Seton, M., Müller, R. D., Zahirovic, S., Williams, S., Wright, N. M., Cannon, J., Whittaker, J. M., Matthews, K. J. and McGirr, R. (2020). A global data set of present-day oceanic crustal age and seafloor spreading parameters, *Geochemistry, Geophysics, Geosystems* **21**(10): e2020GC009214.
URL: *https://agupubs.onlinelibrary.wiley.com/doi/abs/10.1029/2020GC009214*

Shen, W., Ritzwoller, M. H., Kang, D., Kim, Y., Lin, F.-C., Ning, J., Wang, W., Zheng, Y. and Zhou, L. (2016). A seismic reference model for the crust and uppermost mantle beneath China from surface wave dispersion, *Geophysical Journal International* **206**(2): 954–979.
URL: *https://doi.org/10.1093/gji/ggw175*

Simutė, S., Steptoe, H., Cobden, L., Gokhberg, A. and Fichtner, A. (2016). Full-waveform inversion of the japanese islands region, *Journal of Geophysical Research: Solid Earth* **121**(5): 3722–3741.
URL: *https://agupubs.onlinelibrary.wiley.com/doi/abs/10.1002/2016JB012802*

Tao, K., Grand, S. P. and Niu, F. (2018). Seismic structure of the upper mantle beneath eastern asia from full waveform seismic tomography, *Geochemistry, Geophysics, Geosystems* **19**(8): 2732–2763.
URL: *https://agupubs.onlinelibrary.wiley.com/doi/abs/10.1029/2018GC007460*

Tape, C., Liu, Q., Maggi, A. and Tromp, J. (2009). Adjoint tomography of the southern california crust, *Science* **325**(5943): 988–992.
URL: *https://www.science.org/doi/abs/10.1126/science.1175298*

Tape, C., Liu, Q., Maggi, A. and Tromp, J. (2010). Seismic tomography of the southern California crust based on spectral-element and adjoint methods, *Geophysical Journal International* **180**(1): 433–462.
URL: *https://doi.org/10.1111/j.1365-246X.2009.04429.x*

Tapponnier, P., Peltzer, G., Le Dain, A. Y., Armijo, R. and Cobbold, P. (1982). Propagating extrusion tectonics in Asia: New insights from simple experiments with plasticine, *Geology* **10**(12): 611–616.
URL: *https://doi.org/10.1130/0091-7613(1982)10<611:PETIAN>2.0.CO;2*

Tarantola, A. (1988). Theoretical background for the inversion of seismic waveforms including elasticity and attenuation, *Pure and Applied Geophysics* **128**(1-2): 365–399.
URL: *https://doi.org/10.1007/bf01772605*

Tarantola, A. (2005). *Inverse problem theory and methods for model parameter estimation*, SIAM.

Thrastarson, S., van Herwaarden, D.-P. and Fichtner, A. (2021). Inversionson: Fully automated seismic waveform inversions, *California Digital Library (CDL)* .
URL: *https://doi.org/10.31223/x5f31v*

Thrastarson, S., van Herwaarden, D.-P., Krischer, L. and Fichtner, A. (2021). LASIF: LArge-scale seismic inversion framework, an updated version, *EarthArXiv* .
URL: *https://doi.org/10.31223/x5nc84*

Thrastarson, S., van Driel, M., Krischer, L., Boehm, C., Afanasiev, M., van Herwaarden, D.-P. and Fichtner, A. (2020). Accelerating numerical wave propagation by wavefield adapted meshes. Part II: full-waveform inversion, *Geophysical Journal International* **221**(3): 1591–1604.
URL: *https://doi.org/10.1093/gji/ggaa065*

Tromp, J., Tape, C. and Liu, Q. (2005). Seismic tomography, adjoint methods, time reversal and banana-doughnut kernels, *Geophysical Journal International* **160**(1): 195–216.
URL: *https://doi.org/10.1111/j.1365-246X.2004.02453.x*

van Leeuwen, T. and Herrmann, F. J. (2013). Fast waveform inversion without source-encoding, *Geophysical Prospecting* **61**(s1): 10–19.
URL: *https://onlinelibrary.wiley.com/doi/abs/10.1111/j.1365-2478.2012.01096.x*

van Herwaarden, D. P., Afanasiev, M., Thrastarson, S. and Fichtner, A. (2021). Evolutionary full-waveform inversion, *Geophysical Journal International* **224**(1): 306–311.
URL: *https://doi.org/10.1093/gji/ggaa459*

van Herwaarden, D. P., Boehm, C., Afanasiev, M., Thrastarson, S., Krischer, L., Trampert, J. and Fichtner, A. (2020). Accelerated full-waveform inversion using dynamic mini-batches, *Geophysical Journal International* **221**(2): 1427–1438.
URL: *https://doi.org/10.1093/gji/ggaa079*

Virieux, J. and Operto, S. (2009). An overview of full-waveform inversion in exploration geophysics, *Geophysics* **74**(6): WCC1–WCC26.
URL: *https://doi.org/10.1190/1.3238367*

Wessel, P., Smith, W. H. F., Scharroo, R., Luis, J. and Wobbe, F. (2013). Generic mapping tools: Improved version released, *Eos, Transactions American Geophysical Union* **94**(45): 409–410.
URL: *https://agupubs.onlinelibrary.wiley.com/doi/abs/10.1002/2013EO450001*

Wu, J., Suppe, J., Lu, R. and Kanda, R. (2016). Philippine sea and east asian plate tectonics since 52 ma constrained by new subducted slab reconstruction methods, *Journal of Geophysical Research: Solid Earth* **121**(6): 4670–4741.
URL: *https://agupubs.onlinelibrary.wiley.com/doi/abs/10.1002/2016JB012923*

Yin, A. (2010). Cenozoic tectonic evolution of asia: A preliminary synthesis, *Tectonophysics* **488**(1): 293–325. Extensional Tectonics in the Basin and Range, the Aegean, and Western Anatolia.
URL: *https://www.sciencedirect.com/science/article/pii/S0040195109003217*

Zhang, Y., Yu, K., Fan, T., Yue, Y., Wang, R., Jiang, W., Xu, S. and Wang, Y. (2020). Geochemistry and petrogenesis of quaternary basalts from weizhou island, northwestern south china sea: Evidence for the hainan plume, *Lithos* **362-363**: 105493.
URL: *https://www.sciencedirect.com/science/article/pii/S0024493720301304*

Zhao, D. (2004). Global tomographic images of mantle plumes and subducting slabs: insight into deep earth dynamics, *Physics of the Earth and Planetary Interiors* **146**(1): 3–34. Plumes and Superplumes.
URL: *https://www.sciencedirect.com/science/article/pii/S0031920104001086*

Zhao, D., Hasegawa, A. and Horiuchi, S. (1992). Tomographic imaging of p and s wave velocity structure beneath northeastern japan, *Journal of Geophysical Research: Solid Earth* **97**(B13): 19909–19928.
URL: *https://agupubs.onlinelibrary.wiley.com/doi/abs/10.1029/92JB00603*

Zheng, S., Sun, X., Song, X., Yang, Y. and Ritzwoller, M. H. (2008). Surface wave tomography of china from ambient seismic noise correlation, *Geochemistry, Geophysics, Geosystems* **9**(5).
URL: *https://agupubs.onlinelibrary.wiley.com/doi/abs/10.1029/2008GC001981*

Zheng, X.-F., Yao, Z.-X., Liang, J.-H. and Zheng, J. (2010). The Role Played and Opportunities Provided by IGP DMC of China National Seismic Network in Wenchuan Earthquake Disaster Relief and Researches, *Bulletin of the Seismological Society of America* **100**(5B): 2866–2872.
URL: *https://doi.org/10.1785/0120090257*

Zheng, Y.-F., Xiao, W.-J. and Zhao, G. (2013). Introduction to tectonics of china, *Gondwana Research* **23**(4): 1189–1206.
URL: *https://www.sciencedirect.com/science/article/pii/S1342937X12003127*

Zhu, H., Bozdağ, E., Peter, D. and Tromp, J. (2012). Structure of the european upper mantle revealed by adjoint tomography, *Nature Geoscience* **5**(7): 493–498.
URL: *https://doi.org/10.1038/ngeo1501*

Zhu, H., Komatitsch, D. and Tromp, J. (2017). Radial anisotropy of the North American upper mantle based on adjoint tomography with USArray, *Geophysical Journal International* **211**(1): 349–377.
URL: *https://doi.org/10.1093/gji/ggx305*

Chapter 3

Structure and dynamics of lithosphere and asthenosphere in Asia: A seismological perspective

This chapter was published as a paper entitled "Structure and dynamics of lithosphere and asthenosphere in Asia: A seismological perspective" in *Geophysical Research Letters*, 2023, https://doi.org/10.1029/2022GL101704

Structure and Dynamics of Lithosphere and Asthenosphere in Asia: A Seismological Perspective

Jincheng Ma[1†], Hans-Peter Bunge[1], Andreas Fichtner[2], Sung-Joon Chang[3], and You Tian[4]

[1] Department of Earth and Environmental Sciences, Ludwig-Maximilians-Universität München, Munich, Germany
[2] Department of Earth Sciences, ETH Zürich, Zurich, Switzerland
[3] Department of Geophysics, Kangwon National University, Chuncheon, South Korea
[4] College of Geoexploration Science and Technology, Jilin University, Changchun, China

Key Points:

- Full-waveform tomographic images reveal lateral heterogeneities and anisotropy in the lithosphere and asthenosphere beneath the Asian region
- India-Eurasia collision induced large-scale low-velocity anomaly and crustal thickening spanning from the Himalayas to the Baikal rift zone
- Asthenosphere in East & SE Asia exhibits strong $v_{sh} > v_{sv}$ and partially decouples lithosphere, bounded by subduction trench & cratonic keels

3.1 Abstract

Knowledge of lithospheric structure is essential for understanding the impact of continental collision and oceanic subduction on surface tectonic configurations. Full-waveform tomographic images reveal lateral heterogeneities and anisotropy of the lithosphere and asthenosphere in Asia. Estimating lithospheric thickness from seismic velocity reductions at depth exhibits large variations underneath different tectonic units. The thickest cratonic roots are present beneath the Sichuan, Ordos, and Tarim basins and central India. Radial anisotropy signatures of eleven representative tectonic provinces uncover the different nature and geodynamic processes of their respective past and present deformation. The large-scale continental lithospheric deformation is characterized by low-velocity anomalies from the Himalayan Orogen to the Baikal rift zone in central Asia, coupled with the post-collision thickening of the crust. The horizontal low-velocity layer of ∼100-300 km depth extent below the lithosphere points toward the existence of the asthenosphere beneath East and Southeast Asia, with heterogeneous anisotropy indicative of channel flows.

Plain Language Summary

The lithospheric plates, like mosaics of the Earth's surface, are moving coherently over the weaker, convecting asthenosphere. The lithospheric structure and thickness dictated by mantle dynamics play a first-order role in understanding the active tectonics and morphological evolution of the Asian region. Here, the latest high-resolution full-waveform tomographic model, *SinoScope 1.0*, is employed to investigate the seismic structure and dynamics of the lithosphere and asthenosphere from a seismological perspective. The lithospheric thickness of known various geological units and cratonic blocks is retrieved with large variability. The observed anisotropic signatures within the lithosphere and asthenosphere provide important constraints on the deformation state and history of different tectonic provinces. The India-Eurasia collision primarily induced large-scale lithospheric deformation and thickening of the crust in the west of the North-South Gravity Lineament. The narrow low-velocity layer below the lithosphere lies beneath East and Southeast Asia and is bounded by subduction trenches and cratonic blocks, which provides seismic evidence for the low-viscosity asthenosphere that partially decouples plates from mantle flow beneath and allows plate tectonics to work above. The lithospheric thinning and extension, intensive magmatism, and mineralization are potentially associated with the strong interaction between the lithosphere and asthenospheric flow in the eastern Asian margin.

3.2 Introduction

The Asian region is characterized by diverse and complex patterns of extensive magmatism and intracontinental deformation, which are recorded in its geological and tectonic history and revealed by seismic imaging (Figure 3.1; Yin, 2010; Ren et al., 2013; Ma et al., 2022). Cenozoic (66 - 0 Ma) deformation dominates the tectonic configuration of the Asian continent along the Eastern Tethyan orogen, expressed by developments of the Tibetan Plateau and Iranian Plateau resulting from collisions of Indian and Arabian plates towards the Eurasian Plate (Chang and Zeng, 1973; Dewey, 1989; DeCelles et al., 2002; Reilinger et al., 2006). Large fragments of the Eurasian lithosphere were extruded eastward out of the central Tibetan Plateau and toward southern China and northern Indochina, significantly influencing the geological evolution of Southeast Asia (Tapponnier et al., 1982, 2001; Gilder et al., 1996). The central Asian deformation domain extends from the northern edge of the Tibetan Plateau to the northern tip of the Baikal rift system, representing one of the far-field effects of the India-Eurasia collision (Molnar and Tapponnier, 1975; Tapponnier and Molnar, 1979; Yin and Harrison, 2000; Yin, 2006). In East and Southeast Asia, subduction is the dominant plate-tectonic process, and there have been thousands of kilometers of oceanic lithosphere absorbed by the mantle beneath the Eurasian Plate during the Mesozoic (252 - 66 Ma) as the Tethys Oceans and Izanagi Plate were subducted (Müller et al., 2016). Moreover, during the Cenozoic, the Australian Plate moved northwards, the Pacific Plate and Philippine Sea Plate moved westwards, and some fragments sourced from them were collaged to Southeast Asia (Seton et al., 2012; Hall and Spakman,

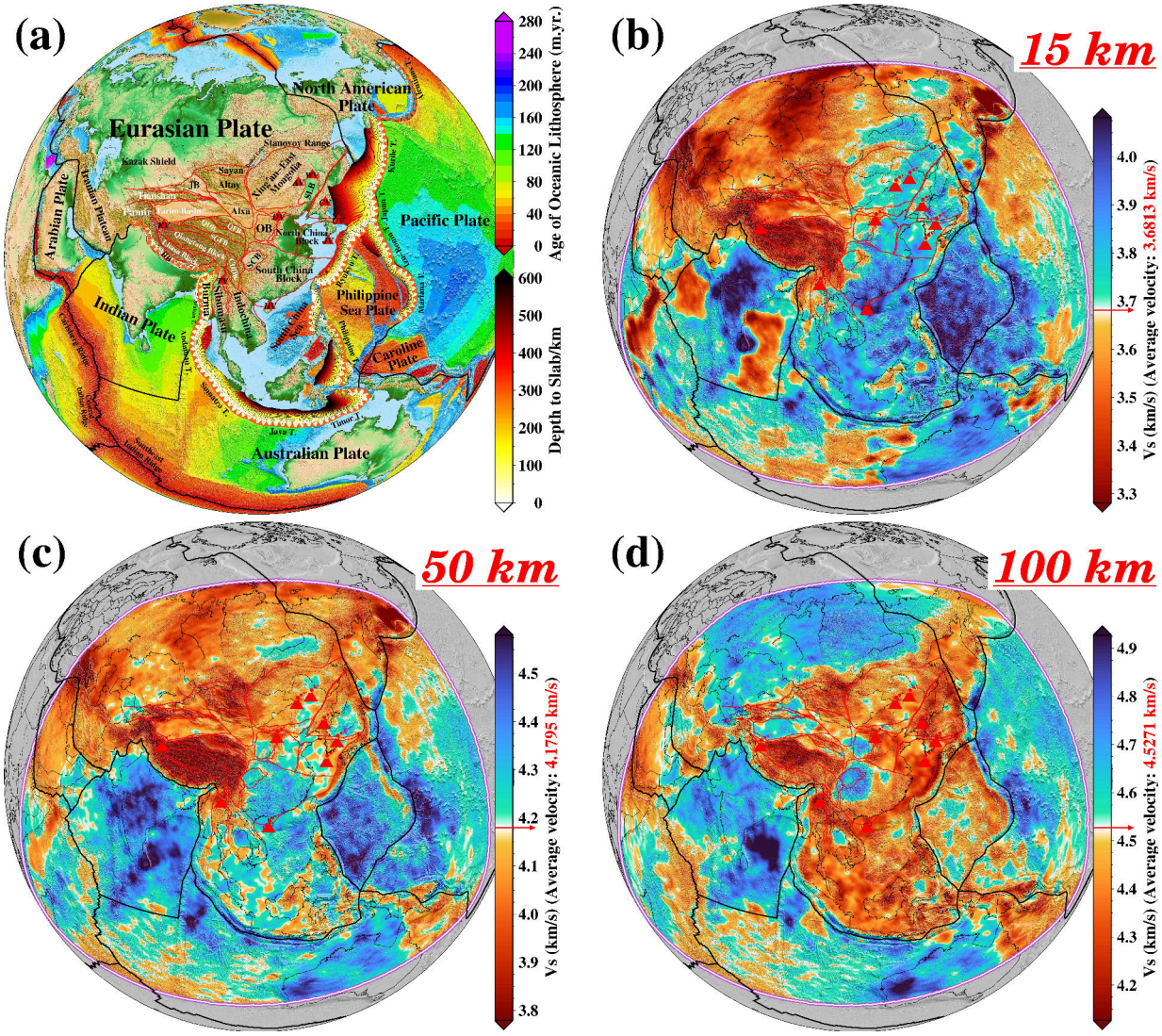

Figure 3.1: (a) Surface topography and major tectonic features of the broad Asian region. Colors show the age of the oceanic lithosphere with the scale shown on the top right side. Color contour lines show depths to the upper boundaries of the subducting slabs with an interval of 20 km (Slab2.0; Hayes et al., 2018), whose scale is shown on the lower right side. Black lines denote the major plate boundaries (modified from Bird, 2003), and red lines delineate main tectonic units, basins, and large fault zones. Red triangles mark the Cenozoic intraplate volcanoes. AV, Arxan Volcano; CDDB, Chuan-Dian Diamond Block; CV, Changbai Volcano; DV, Datong Volcano; HB, Himalaya Block; HV, Hainan Volcano; JB, Junggar Basin; JV, Jeju Volcano; KV, Kunlun Volcano; OB, Ordos Basin; QDB, Qaidam Basin; QFB, Qilian Fold Belt; SCB, Sichuan Basin; SGFB, Songpan Ganzi Fold Belt; SLB, Songliao Basin; TV, Tengchong Volcano; UV, Ulleung Volcano; WV, Wudalianchi Volcano. (b-d) Map views of the absolute isotropic shear-wave velocity at depths of 15 km, 50 km, and 100 km.

2015). The interactions of these lithospheric plates are suggested to be a mechanism to cause the lithospheric thinning and destruction, intensive intraplate seismic and volcanic activities, marginal basins and volcanic arcs, and possibly the further development of the trench-arc-back-arc extensional system in the eastern Asian margin (Schellart and Lister, 2005; Zhao, 2021). To better understand how tectonic stresses of the overlying plate control asthenospheric deformation which in turn affects plate dynamics, it is necessary to study the detailed structure of the lithosphere and asthenosphere as well as the plate tectonics and mantle dynamics of the Asian region.

Cenozoic deformation of the Asian lithosphere is commonly attributed to the combined effects of continental collision and oceanic subduction. How the two classes of plate boundary processes interact with one another in controlling the widely distributed intracontinental deformation over a 3,000-km region remains the subject of debate and controversy. When collision and subduction are considered as two relatively independent processes, one thought is that the timing, location, and style of Cenozoic extensional features along the eastern margin of the Eurasian Plate are closely related to the subduction of oceanic plates rather than far-field effects of the India-Eurasia collision (e.g., Northrup et al., 1995; Yin, 2000; Hall, 2002; Royden et al., 2008). Alternatively, the India-Eurasia collision provokes compressional stresses that diverge from the collision zone and transmit through the rigid lithosphere all the way to subduction trenches, where it follows the retreat of subducting lithospheres, controlling the geometry and kinematics of major strike-slip faults and back-arc basins under the influence of the large-scale deformation of the Asian lithosphere (e.g., Tapponnier et al., 1982; Jolivet et al., 1994). Moreover, the tectonic development of the broad Asian region, commonly interpreted as a result of the plate boundary processes as discussed above, intrinsically correlates with the thermal structure of the lithosphere induced by crustal and mantle processes (e.g., Molnar et al., 1993; Harrison et al., 1998; Beaumont et al., 2001; Jolivet et al., 2018). Until now, it remains poorly understood what roles of collision and subduction coupled with time-dependent mantle flows have played in shaping the overall tectonics and deformation history of the Asian lithosphere.

In this study, our primary focus is on deciphering the seismic structure and dynamics of the lithosphere and asthenosphere beneath China and adjacent regions with the help of the latest full-waveform tomographic model of this region by Ma et al. (2022). The present work sheds important new light on the dynamic characteristics of the different tectonic provinces, the morphology of the underthrusting Indian lithosphere and its geodynamic implications, and the interaction between the lithosphere and asthenosphere in the eastern Asian margin.

3.3 Data and Full-waveform Inversion

Our dataset contains more than 500,000 three-component seismograms recorded at 2,427 seismometers, corresponding to 410 earthquakes that occurred between 2009 and 2018 along the tectonically active zones of continental collision and oceanic subduction (Figure S1 in the Supporting Information). Physical properties of the Earth's interior are

indirectly detected through seismic waves excited by earthquakes. When seismic waves propagate inside the Earth and encounter structural heterogeneities with a certain scale, wave propagation speed changes, reflection and scattering phenomena occur, and interconversions between compressional and shear waves happen. The combined effect of multiple heterogeneities produces a complicated wavefield recorded in the form of three-component seismograms. The full-waveform inversion technique based on adjoint and spectral-element methods can be employed to maximumly exploit the information contained in these seismic wavefield complexities to determine the fine-scale structural heterogeneities from which they originated across various orders of magnitude in frequency and wavelength (e.g., Fichtner, 2011; Kennett and Fichtner, 2020; Tromp, 2020). Here we provide a detailed tectonic interpretation of the latest full-waveform inversion applied to the broad Asian region (*SinoScope 1.0*; Ma et al., 2022), with a special focus on China and adjacent regions where particularly dense data coverage is available. The multi-scale full-waveform inversion naturally combines the advantages of surface- and body-waves and jointly inverts for the crust and mantle structure in the period range of 30 s to 120 s, yielding constraints on lithosphere and asthenosphere whose interactions shape the nature of plate tectonics.

3.4 Results and Discussion

The model parameters involved in the inversion include the wave velocities of vertically and horizontally propagating/polarized P- and S-waves (v_{pv}, v_{ph}, v_{sv}, and v_{sh}) and mass density (ρ). The data that enters the inversion process is mostly sensitive to variations in v_{sv} and v_{sh}; sensitivity kernels with respect to v_{pv}, v_{ph} and ρ are small or negligible (Ma et al., 2022), which are not used to facilitate the interpretation of tomographic images in the following sections. Radial anisotropy is a type of transverse isotropy with a radial symmetry axis, which produces differences in propagation speed between horizontally and vertically polarized shear waves, irrespective of their propagation azimuth (e.g., Hess, 1964; Montagner and Tanimoto, 1991). The radial anisotropy parameter $\xi = (v_{sh} - v_{sv})/v_s$ provides an important indicator of lithospheric deformation in the crust and mantle or mantle flow in the asthenosphere in either horizontal direction (positive ξ) or vertical direction (negative ξ), where the isotropic shear-wave velocity is computed from v_{sh} and v_{sv} as $v_s = \sqrt{\frac{(2v_{sv}^2+v_{sh}^2)}{3}}$ (Panning and Romanowicz, 2006). Horizontal slices through the variations of v_s, v_{sv}, v_{sh} and ξ are shown in Figures S2-S12.

3.4.1 Average Radial Characteristics of Different Tectonic Provinces

The tectonic framework of Asia is characterized by the assembly of diverse tectonic units along with orogenic belts in the triangular area where the Paleo-Asian Ocean, Tethyan, and Western-Pacific domains meet. To obtain more detailed characteristics of velocity and anisotropy variations with depth in the specific region, the study area is subdivided into eleven representative tectonically distinct subregions according to the distribution of major

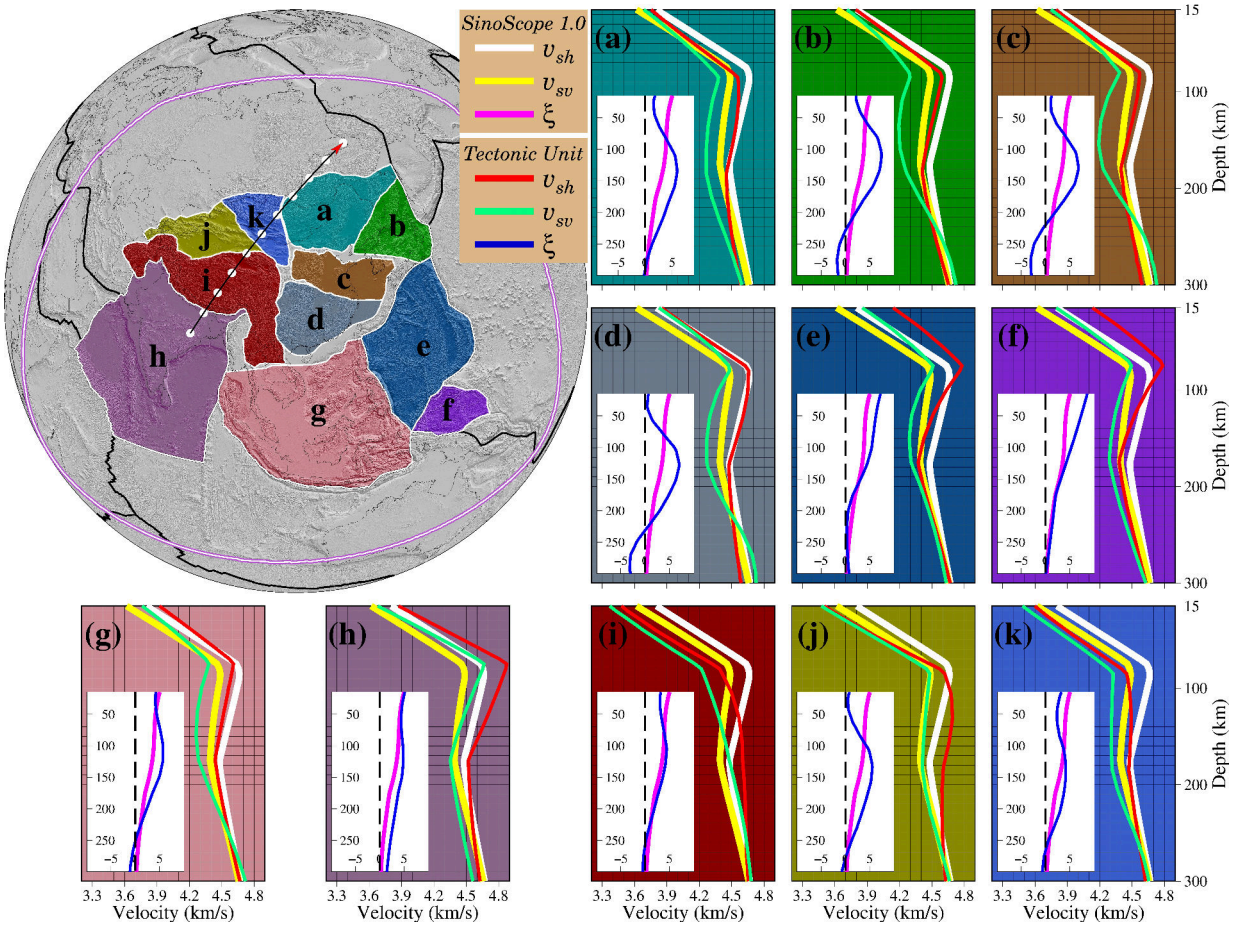

Figure 3.2: Topographic map shows the geographic locations of the samples and the cross-section (black line with white dots) for which the vertical profile is shown in Figure 3.3. (a-k) Lateral averages for vertically/horizontally polarized shear-wave velocity (v_{sv} and v_{sh}) and radial shear-wave anisotropy (ξ) of eleven tectonically distinct provinces, corresponding to the color-matched shaded areas as shown in the map, which are extracted from *SinoScope 1.0* (Ma et al., 2022) and illustrated by red (v_{sh}), green (v_{sv}), and blue (ξ) lines. Bold white (v_{sh}), yellow (v_{sv}), and magenta (ξ) lines are overall 1-D radial profiles of *SinoScope 1.0* (Ma et al., 2022) and are plotted for comparison with specific tectonic units. Dashed lines represent depth profiles for isotropic models with $\xi = 0$.

boundaries and faults (Figures 3.1 and 3.2; Bird, 2003; Zhang et al., 2003). The radially averaged v_{sv} and v_{sh} of the inversion domain are marked by a pronounced negative velocity gradient at depths ranging from 80 to 180 km (Figure 3.2). Within the upper 200 km of the Earth, variations in the radial anisotropy range between 1% and 5%, which indicates that the Asian lithosphere as a whole is dominated by horizontal movements, as derived from GPS observations (Hao et al., 2019; Wang and Shen, 2020).

The concept of lithosphere-asthenosphere boundary (LAB) remains debated because of different definitions based on different geophysical observations (Eaton et al., 2009). In seismic tomography, the LAB inferred from the shear-velocity structure can be defined as a sharp boundary between the high-velocity lid and the low-velocity zone, which is interpreted as the maximum of the velocity gradient ($-\delta V/\delta z$) above the low-velocity zone (Burgos et al., 2014). However, the maximum gradient is not unequivocally observed beneath the continental lithosphere due to the nonexistence of sharp velocity contrast across the LAB. The strong 3-D velocity heterogeneities of the full-waveform tomographic model may also make some empirical approaches (e.g., Priestley and MKenzie, 2006) no longer applicable for estimating the depth of the LAB (hereafter referred to as the lithospheric thickness) for a given isotherm when converting shear-wave velocities to temperatures. It mainly stems from the possibility of unrealistic temperature values during the velocity-to-temperature conversion. Hence, we adopt the perturbation cutoff of v_{sv} and v_{sh} (δv_{sv} and $\delta v_{sh} \geq 1.25\%$ in Figures S13 and S14; Maurya et al., 2016) to estimate the lithospheric thickness coupled with depth slices of the absolute shear-velocity structure down to 250 km depth (Figures S2-S12) and further discuss specific structural features of major geological units in the study area.

The observations that emerge from our tomographic results reveal a thick cratonic lithosphere ($\sim$80 km; Figures S2-S5 and S13) in South China, whereas the lithosphere with the presence of $\geq 1.25\%$ high-velocity is just $\sim$65 km in Northeast and North China. The thickest lithospheric keels (200-250 km) comprising deep cratonic roots are observed in the Sichuan, Ordos, and Tarim basins. The deep part of the cratonic root of the Sichuan Basin appears larger than its surface expression and extends eastward to the middle of the South China Block (Figures S13 and S14). The lithospheric thickness of the Indian Plate is retrieved with large variability between 150 and 250 km. Compared with the continental lithosphere, the oceanic lithosphere beneath the South China Sea, Philippine Sea Plate, and Caroline Plate is almost flatter and thinner ($\sim$90 km), overlying the low-velocity asthenosphere (Figures S2-S6 and S13-S14). The low-velocity zone is widely observed beneath Eastern Mongolia, Northeast, North and South China, Japan Sea, Philippine Sea Plate, Caroline Plate, Southeast Asia, and Indian Plate, except in areas of the thick continental crust where there is no apparent velocity contrast, for instance, Tibetan Plateau and Mongolian Plateau. As is evident from Figure 3.2, the velocity reduction pattern and depth above which reduction occurs, strongly vary with the choice of the tectonic province, reflecting their respective distinct seismic characteristics. Following a drop in v_{sv} and v_{sh}, the base of the low-velocity zone is marked by an increase: the transition is sharp in v_{sh} but gradual in v_{sv}, the Indian Plate being the only exception as both v_{sv} and v_{sh} increase sharply.

Seismic anisotropy in the upper mantle is generally attributed to the coherent lattice-preferred orientation of intrinsically anisotropic crystals such as olivine (Nicolas and Christensen, 1987; Zhang and Karato, 1995) and is related to past and present geodynamic processes, which provides insights into our understanding of lithospheric evolution, physical interaction between lithosphere and asthenosphere, and channel flow within the asthenosphere. Unresolved sub-wavelength heterogeneities are also capable of producing apparent anisotropy, which does not need to be related in the same way as intrinsic anisotropy (Fichtner et al., 2013). Since it is currently impossible to quantitatively separate the intrinsic and apparent anisotropy, we here restrict attention to holistic anisotropic signatures of different tectonic provinces. The strength and nature of seismic anisotropy vary significantly depending on the depth extent and tectonic unit (Figure 3.2). For the Philippine Sea and Caroline plates, we observe significant positive radial anisotropy ($\xi \geq 5$) at depths shallower than 110 km, peaking near the surface with rapidly decreasing strength at greater depths, which indicates a strong correlation with the present-day horizontal plate motion (Wu et al., 2016). The Indian Plate and Southeast Asia, which are composed of oceanic and continental lithosphere, exhibit different behaviour of radial anisotropy in contrast to the Philippine Sea and Caroline plates. Southeast Asia is characterized by more substantial positive anisotropy than the average 1-D radial one down to ∼200 km with the maximum value at a depth of ∼120 km, whereas the pattern switches to negative at depths greater than 250 km, consistent with what Wehner et al. (2022) revealed. Beneath the Indian Plate, variations in radial anisotropy show a systematic tendency of being positive, with a secondary peak found at a depth of ∼120 km except for the surface, which is the expected result of the dominant horizontal movement of the Indian Plate since the late Mesozoic. South China Block, as the relatively stable continental area, displays small to zero positive radial anisotropy in the uppermost 50 km. After that, the magnitude of radial anisotropy substantially increases and reaches a peak at a depth of ∼120 km, followed by a consistent decrease at larger depths; the prominent negative pattern of radial anisotropy is observed in the depth range of ∼230-300 km. The behaviour of radial anisotropy beneath Eastern Mongolia, Northeast China, North China Block, and Japan Sea is similar to that of the South China Block, apart from the magnitude. The frozen-in lithospheric anisotropy ($\xi > 0$) that reflects the fossil strain field, results from a long and complex history involved in surficial tectonics (Savage, 1999), where the horizontal deformation process dominates. The existence of positive large-scale radial anisotropy with maximum values around depths of 120 km coincides with the depth range of the hypothetical shear zone between the lithosphere and asthenosphere (Ribe, 1989). Negative radial anisotropy at depths greater than 200 km largely correlates with the hot upwellings or cold downwellings above the flat slab beneath Northeast China, Japan Sea, North and South China blocks, and Southeast Asia (e.g., Ma et al., 2019; Zhao, 2021). As the far-field deformation response to the India-Eurasia collision, the low-velocity lithosphere is dominated by positive radial anisotropy beneath the Tibetan Plateau, Tianshan Orogen, eastern and western Himalayan syntaxes, and Altay-Sayan Mountain Range, which provides a good indicator of the relative horizontal movement of continental blocks in the extreme tectonic deformation environment.

3.4.2 Lithospheric Dynamics in Response to the India-Eurasia Collision

Since the Early Cenozoic onset of collision, the Asian lithosphere has been significantly deforming across a vast region, especially from the Himalayan Orogen in the south to the Baikal rift zone in the north (Yin, 2010). The India-Eurasia convergence has driven Himalayan mountain building, Tibetan Plateau formation, and widespread deformation outside the collision zone, accommodating north-south crustal shortening with estimates in the range from a few hundred kilometres to >2000 km (e.g., Tapponnier et al., 2001; Li et al., 2015; Huang et al., 2015). The most prominent features of the Tibetan Plateau and its surrounding deforming area are the thicker crust (50–90 km) than typical continental crust and the strongest negative Bouguer gravity anomaly (up to -500 mGal) in the world (Figure S15). The cross-section through the Tibetan Plateau shows that the Moho (the boundary between the crust and mantle) deepens gently northward from ∼35 km beneath the Tethyan Himalaya to 75-90 km beneath the Qiangtang Block and Songpan Ganzi Fold Belt (Figure 3.3), consistent with the results of receiver function analysis (e.g., He et al., 2014; Cheng et al., 2021). The Indian lithosphere is underthrusting beneath the Himalaya along the Main Himalayan Thrust and continues to extend beneath the Lhasa and Qiangtang blocks with ramp-flat geometry (Figures S16-S21), which has contributed to the crustal thickening, resulting in the deep Moho there (Figure 3.3). The asthenosphere carrying the northward movement of the Indian lithospheric mantle exhibits significant positive radial anisotropy ($\xi > 5$) along the strike. As the tectonic transitional zone between the Tibetan Plateau and stable Siberian Craton, the widely distributed deformation range from the Qilian Fold Belt to the Baikal rift zone is underlain by relatively low-velocity mantle with dominant positive radial anisotropy. It probably reconciles with compressional stresses that diverge from the collision zone. In Figure 3.3, there exists a good agreement between the underthrusting Indian lithosphere and the low Bouguer anomaly along the N-S trending profile, indicating that the geometry of the Bouguer gravity low is induced by the crustal thickening beneath the Tibetan Plateau. Across the well-known North-South Gravity Lineament (NSGL) extending >4000 km from Siberia to South China, there is an abrupt shift in the Moho topography and Bouguer gravity anomaly (Figures S22-S26). The NSGL is likely caused primarily by variations in the Moho depth as a result of the post-collision crustal thickening in the west of the NSGL. The different lithospheric compositions on either side of the NSGL probably contribute secondarily to the formation of the NSGL, which is most likely related to the interaction between the lithosphere and asthenosphere beneath East and Southeast Asia.

3.4.3 Asthenosphere Beneath East and Southeast Asia

The seismic low-velocity channels imaged beneath the East and Southeast Asian lithosphere reflect the presence of the low-viscosity asthenosphere (Figure 3.4), which has weaker mechanical strength than the overlying lithosphere and decouples tectonic plates from the deep mantle. The widespread and prominent low-velocity asthenosphere with a thickness

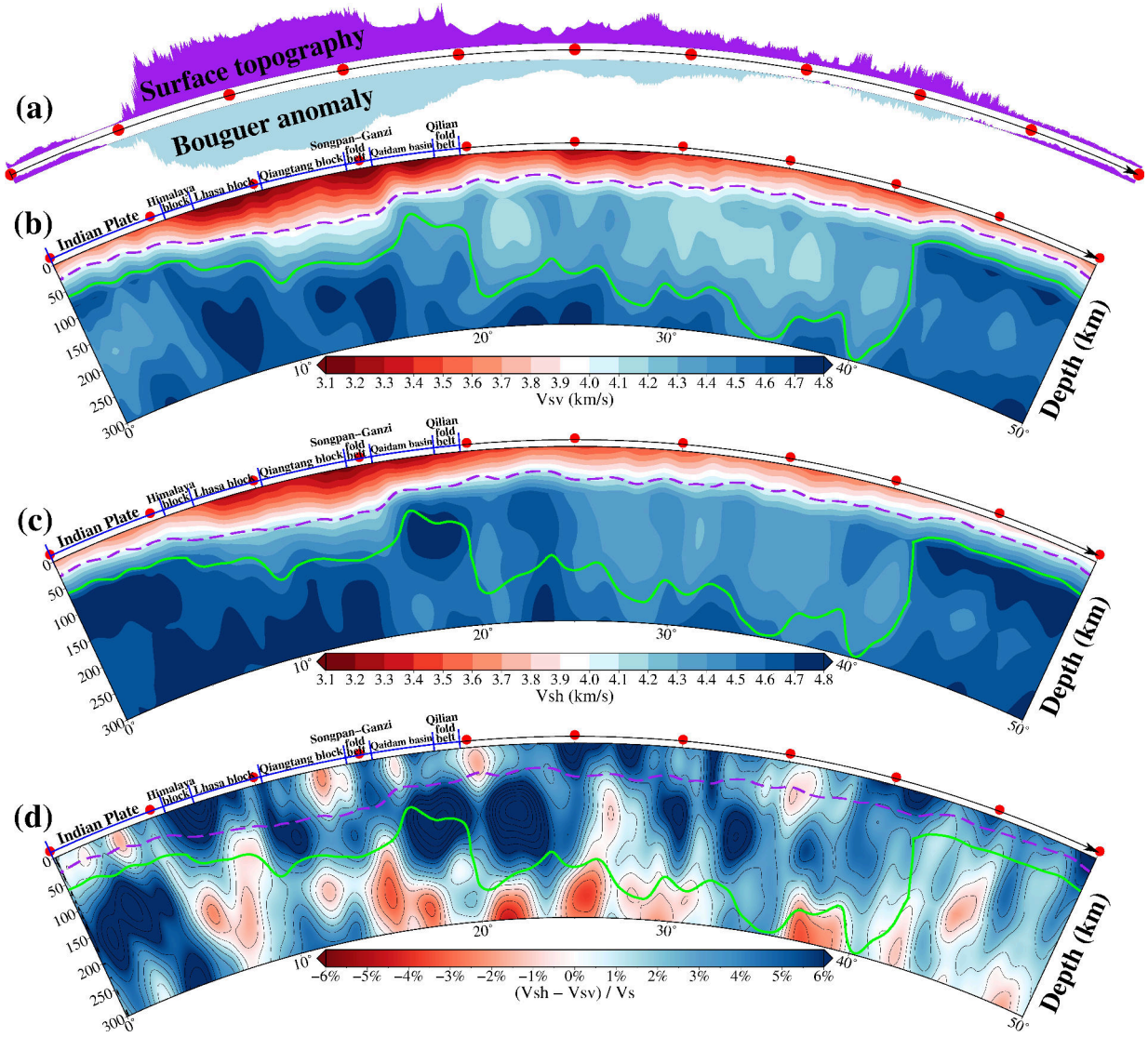

Figure 3.3: (a) Surface topography (top) and Bouguer gravity anomaly (bottom) from the WGM2012 model (Bonvalot et al., 2012) along the oblique profile shown in Figure 3.2. Purple and light blue colors denote positive and negative values of the elevation and Bouguer anomaly, respectively. (b-d) Cross-sections are shown for absolute vertically/horizontally polarized shear-wave velocity (v_{sv} and v_{sh}) and radial shear-wave anisotropy (ξ). Dashed magenta lines indicate the Moho depth estimated from *SinoScope 1.0* (v_s = 4.0 km/s iso-velocity to be a representation of the Moho depth; Ma et al., 2022). Green lines (indicated by an iso-velocity contour of v_s = 4.5 km/s) envelope low-velocity bodies in the mantle beneath the lithosphere. Red dots on the frame of each cross-section are marked every 5°.

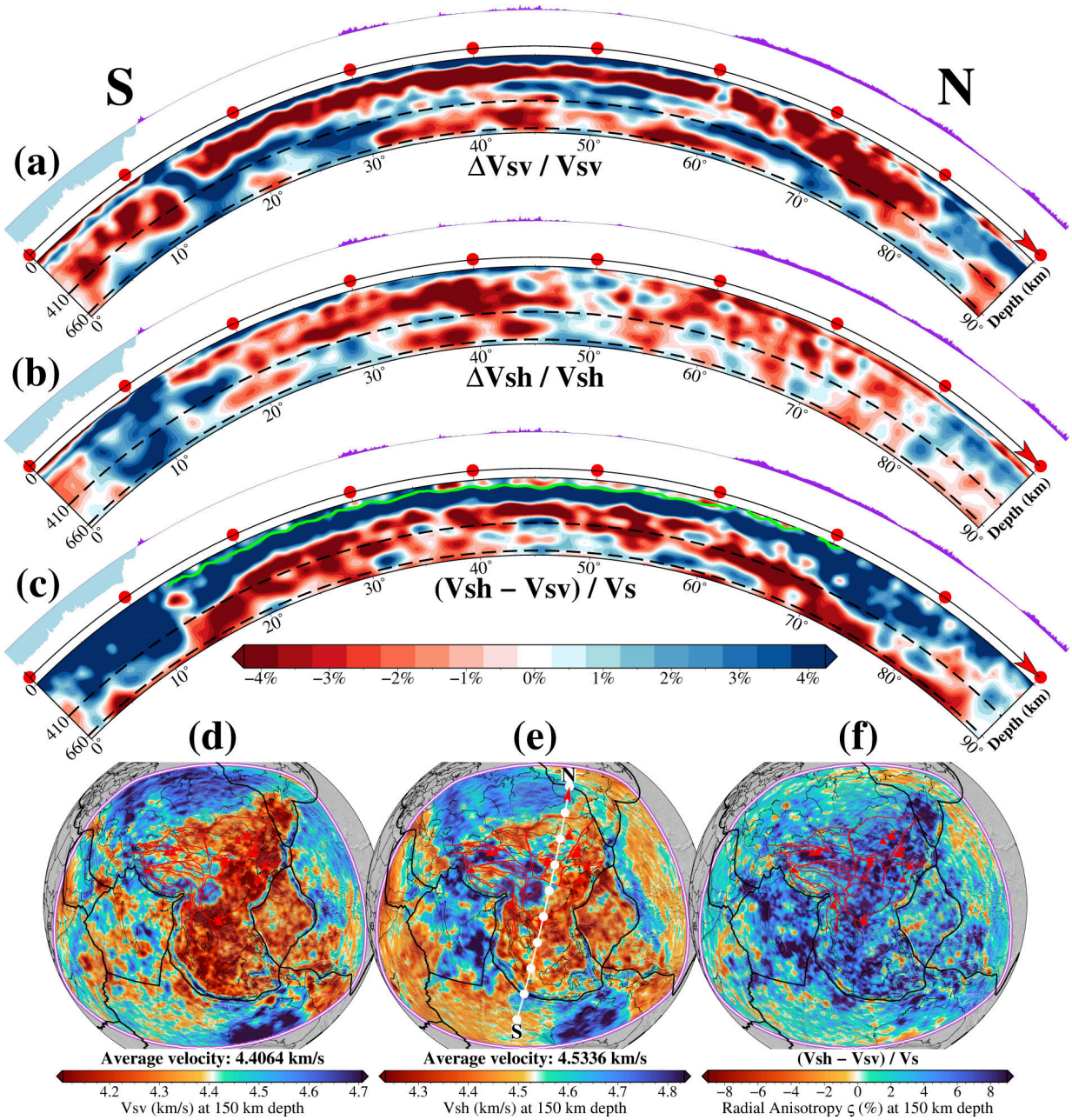

Figure 3.4: (a-c) North-south cross-sections of vertically/horizontally polarized shear-wave velocity (v_{sv} and v_{sh}) perturbations and radial shear-wave anisotropy (ξ) along the profile shown in the map (e). Surface topography and bathymetry along each profile is shown on the top of each cross-section. Dashed black lines denote the 410-km and 660-km discontinuities; Red dots on the frame of each cross-section are marked every 10°. The green line denotes the estimated LAB. (d-f) Distributions of the absolute v_{sv} and v_{sh}, and ξ at 150 km depth; their scales are shown at the bottom.

range of ∼100-300 km is bounded by the subducting slab along the strongly curved convergent boundary (Kurile, Japan, Ryukyu, Philippine, Timor, Java, Sumatra, Andaman, and Arakan) and lithospheric keels (Sichuan and Ordos blocks), which is also coincident spatially with extensive intraplate volcanism. The presence of apparent radial anisotropy ($\xi > 4$) in the asthenosphere reflects strong shear flow beneath the lithosphere, which is accompanied by the largest shear strain at the top and bottom boundaries of the flow channel. The heating from the asthenosphere on the lithosphere subsequently triggered extensive magmatism, mineralization, intraplate volcanism, and the widespread development of extensional structures, and the relative shear motion between the lithosphere and asthenosphere could induce the complex configuration of the lithosphere through extreme lithospheric thinning in the eastern Asian margin (e.g., Zheng et al., 2018; Yang et al., 2021). Beneath the asthenosphere, strong negative radial anisotropy areas indicate vertically oriented structures that can be assigned to specific tectonic events, for example, cold downwellings (subducting slabs, detached lithosphere removed by the shear asthenospheric flows, etc.) along active continental margins (e.g., Zhang, 2012; Ma et al., 2019).

3.5 Conclusions

This study provides new information on the radially anisotropic signature and dynamics of the lithosphere and asthenosphere utilizing high-resolution full-waveform tomographic images in the Asian region that is intended to improve our quantitative understanding of the regional tectonic evolution. The large-scale lithospheric deformation in the west of the NSGL characterized by particularly low velocities is dominated by the strong radial anisotropy with enhanced SH-wave speed and crustal thickening, potentially reflecting the prominent shear strain caused by compressional stresses that diverge from the India-Eurasia collision zone towards the stable Siberian Craton. The underthrusting Indian lithosphere has reached the Songpan Ganzi Fold Belt with a ramp-flat shape, down to ∼250-300 km. Lithospheric keels (Sichuan, Ordos, and Tarim basins) comprise deep cratonic roots (∼200-250 km), which encircle the northwest and east borders of the Tibetan Plateau and might play an important role in the internal deformation and tectonic escape of lithosphere in the Tibetan Plateau. In East and Southeast Asia, the lithospheric thickness exhibits significant variations underneath different tectonic units, and the presence of lamellar-like positive radial anisotropy within the asthenosphere indicates the asthenospheric flow field is dominated by horizontal movements. The lithospheric thinning and extension, magmatism, mineralization, and intraplate volcanism are probably related to the strong interaction between the lithosphere and asthenosphere in the eastern Asian margin.

3.6 Data Availability Statement

Data is available through Ma et al. (2022).

3.7 Acknowledgement

J. Ma acknowledges the financial support from the China Scholarship Council. S.-J. Chang was supported by the Korea Meteorological Administration Research and Development Program under Grant KMI 2022-00810, by the National Research Foundation of Korea (NRF) grant funded by the Korean government (MSIT) (2019R1A2C208506111), and by Basic Science Research Program through the NRF funded by the Ministry of Education (No. 2019R1A6A1A03033167). Y. Tian was supported by the grant from the National Natural Science Foundation of China (Grant No. 41874049 and 42274065). The authors are very grateful to Lucy Flesch (the Editor), Deborah Wehner, and an anonymous reviewer for their constructive comments and suggestions that improved the manuscript. Open Access funding enabled and organized by Projekt DEAL.

3.8 Authorship contribution statement

Jincheng Ma: Conceptualization, Investigation, Methodology, Visualization, Writing - Original draft.
Hans-Peter Bunge and Andreas Fichtner: Supervision, Writing - Review
Sung-Joon Chang and You Tian: Interpretations and Preparation of the manuscript

3.9 Appendix: Supplementary Figures

Contents of this file

Figures S1 - S26

Introduction

Figures S2-S12 present depth slices from 15 to 250 km for model parameters (V_S, V_{SV}, V_{SH}) and radial anisotropy (ξ).

V_S is the Voigt-Reuss-Hill average shear wave velocity, computed from the horizontally and vertically polarized shear wave velocities (V_{SH} and V_{SV}) as $V_S = \sqrt{\frac{(2V_{SV}^2+V_{SH}^2)}{3}}$.

The radial shear wave anisotropy $\xi = \frac{(V_{SH}-V_{SV})}{V_S}$ is the relative seismic wave velocity difference between vertically (SV) and horizontally (SH) polarized shear waves, which can be treated as a good indicator of lithospheric deformation in the crust and mantle or mantle flow in the asthenosphere in either the vertical direction (negative ξ, $V_{SV} > V_{SH}$) or horizontal direction (positive ξ, $V_{SH} > V_{SV}$).

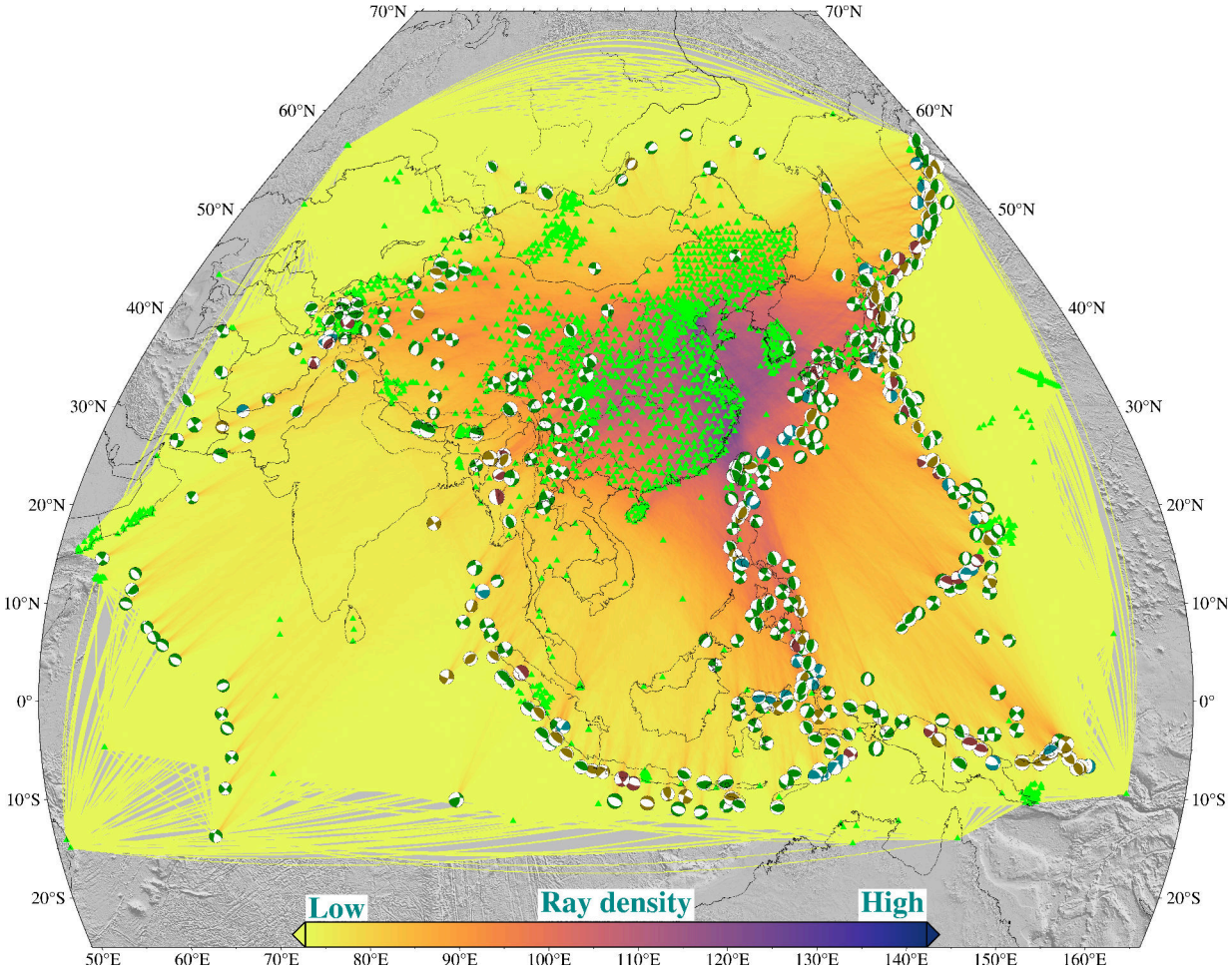

Figure 3.S1: Surface-projected ray density map of the events and stations used in this study, ranging from dark red (best data coverage) to light yellow (least data coverage). Earthquake locations and mechanisms are indicated by moment tensor beachballs and stations by green triangles. In total, 410 earthquakes were recorded at 2,427 unique stations, and the complete data set has 524,138 unique source-receiver pairs.

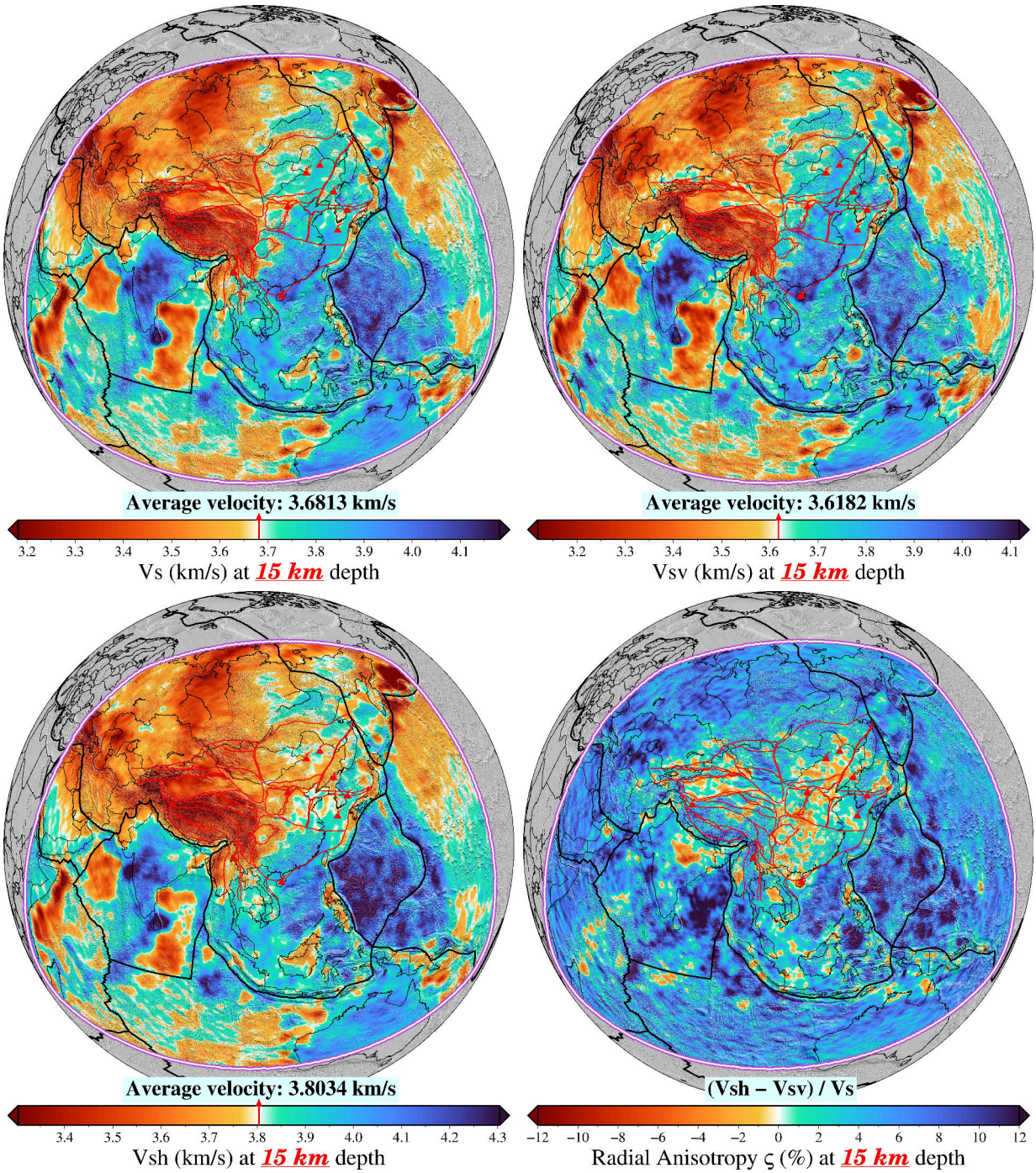

Figure 3.S2: Horizontal slices through ***SinoScope 1.0*** showing the absolute isotropic shear wave velocity (V_S), vertically and horizontally polarized S-wave velocities (V_{SV}, V_{SH}), and radial anisotropy (ξ) at **15** km depth. The dark bold lines delineate the major plate boundaries, and the red lines define main tectonic units, basins, and large fault zones.

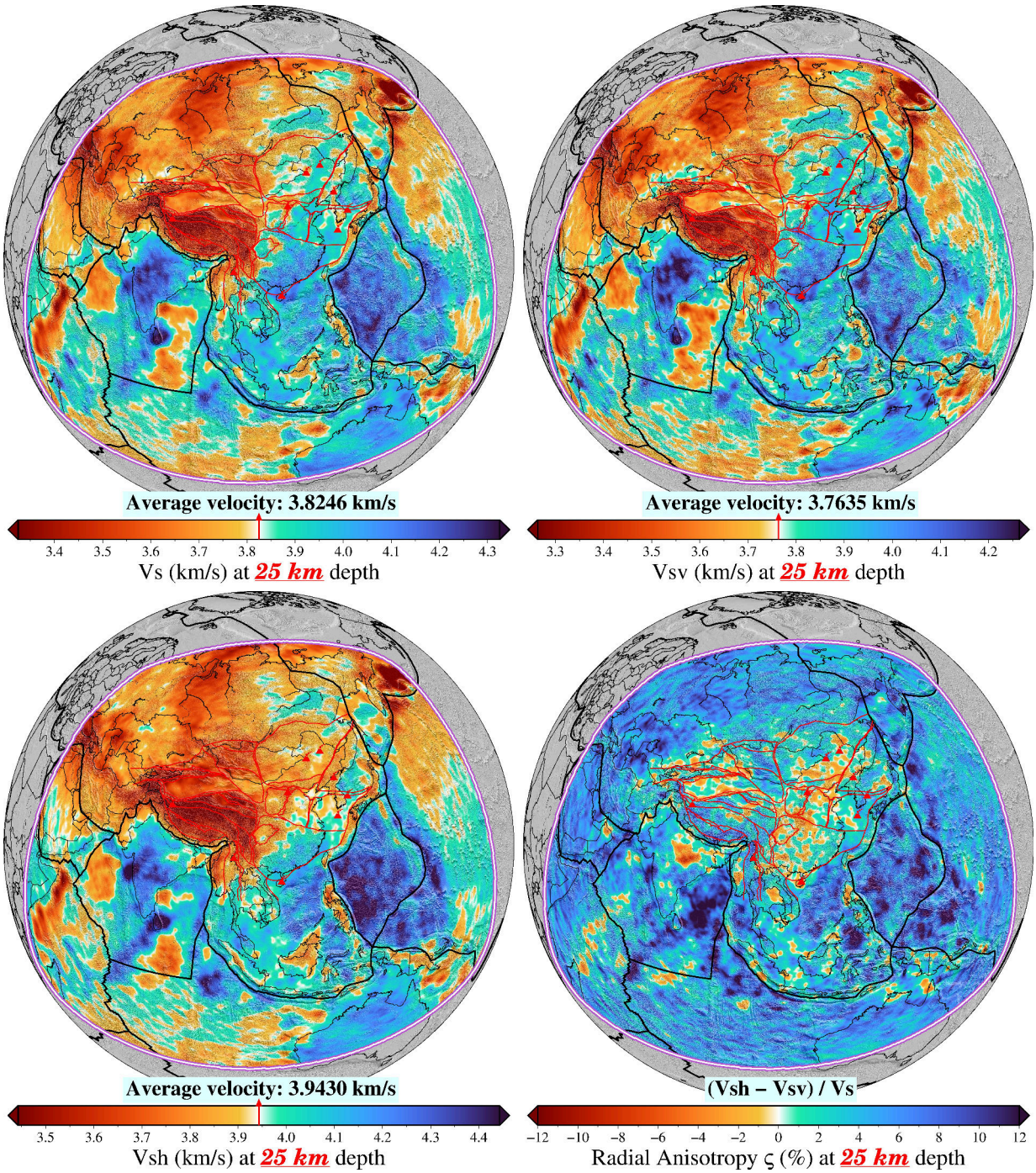

Figure 3.S3: Horizontal slices through ***SinoScope 1.0*** showing the absolute isotropic shear wave velocity (V_S), vertically and horizontally polarized S-wave velocities (V_{SV}, V_{SH}), and radial anisotropy (ξ) at **25** km depth. The dark bold lines delineate the major plate boundaries, and the red lines define main tectonic units, basins, and large fault zones.

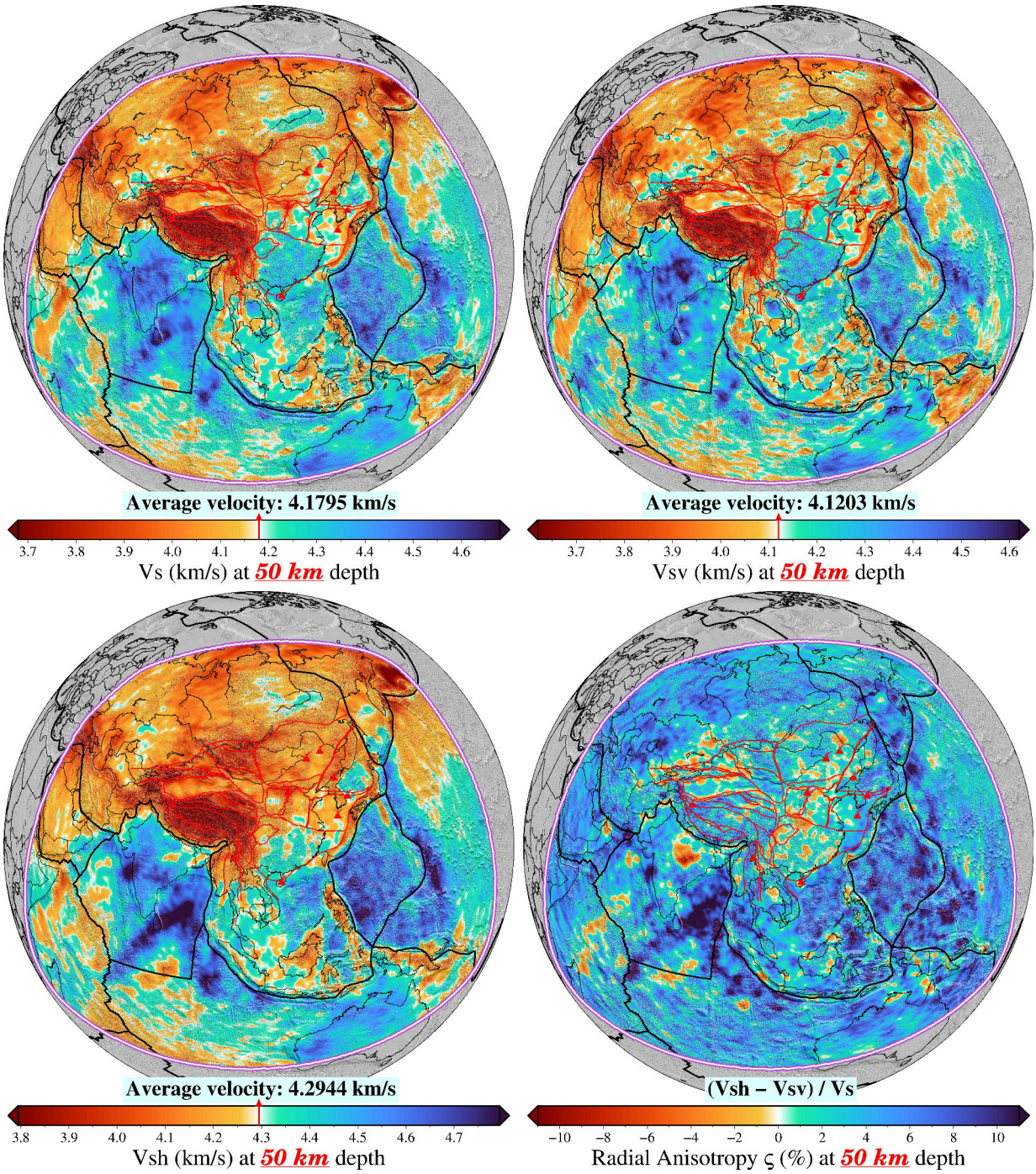

Figure 3.S4: Horizontal slices through ***SinoScope 1.0*** showing the absolute isotropic shear wave velocity (V_S), vertically and horizontally polarized S-wave velocities (V_{SV}, V_{SH}), and radial anisotropy (ξ) at **50** km depth. The dark bold lines delineate the major plate boundaries, and the red lines define main tectonic units, basins, and large fault zones.

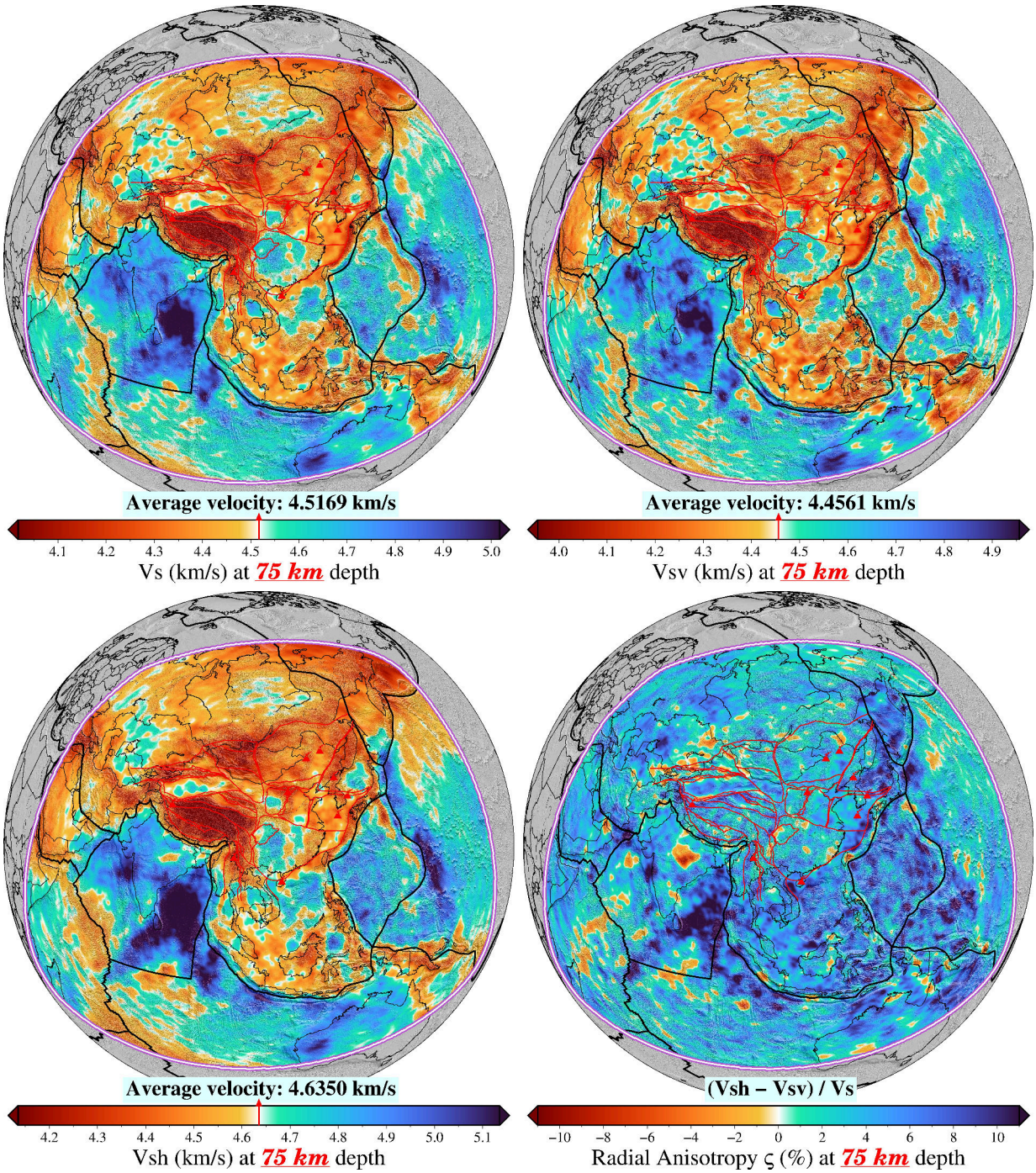

Figure 3.S5: Horizontal slices through ***SinoScope 1.0*** showing the absolute isotropic shear wave velocity (V_S), vertically and horizontally polarized S-wave velocities (V_{SV}, V_{SH}), and radial anisotropy (ξ) at **75** km depth. The dark bold lines delineate the major plate boundaries, and the red lines define main tectonic units, basins, and large fault zones.

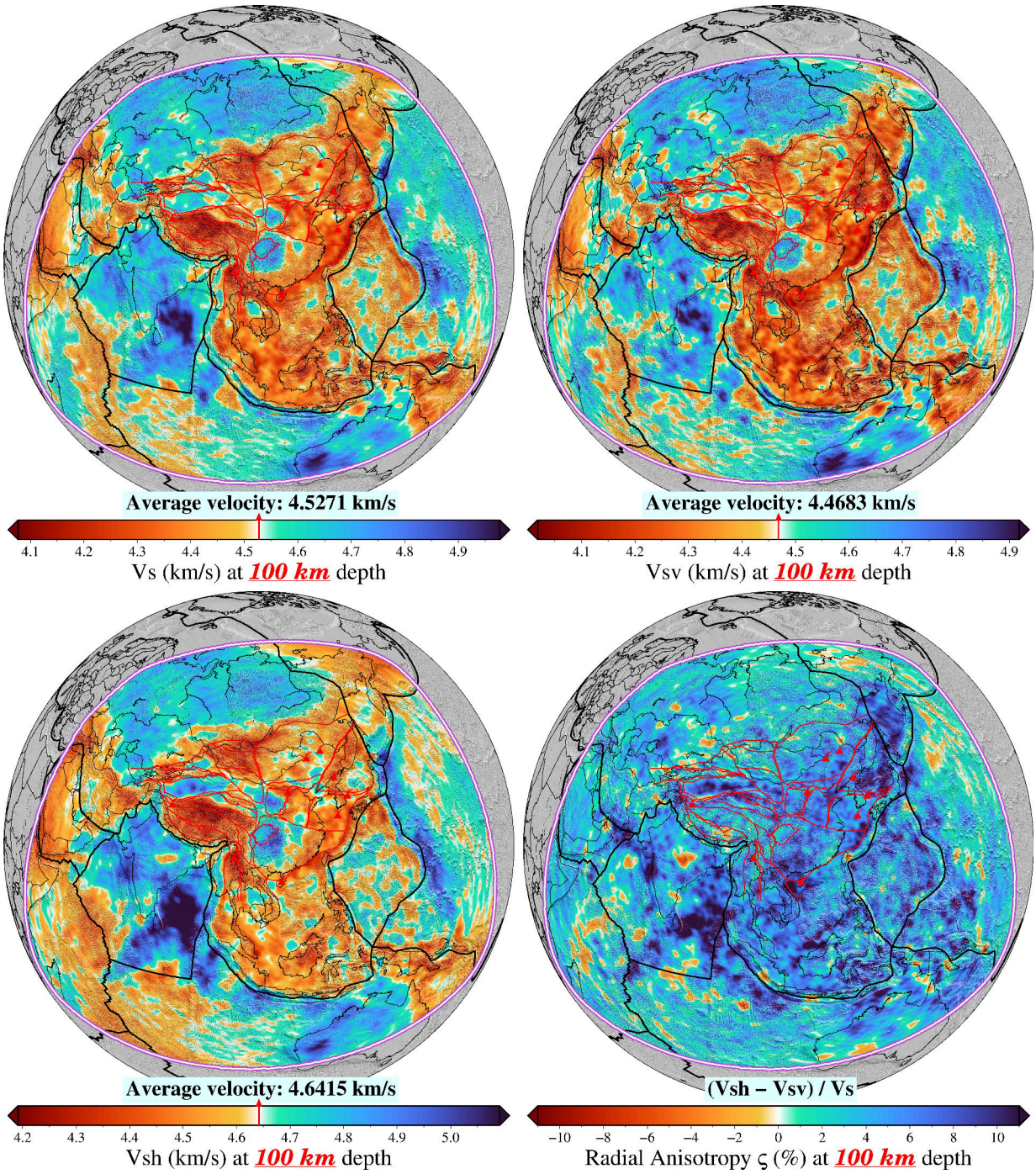

Figure 3.S6: Horizontal slices through ***SinoScope 1.0*** showing the absolute isotropic shear wave velocity (V_S), vertically and horizontally polarized S-wave velocities (V_{SV}, V_{SH}), and radial anisotropy (ξ) at **100** km depth. The dark bold lines delineate the major plate boundaries, and the red lines define main tectonic units, basins, and large fault zones.

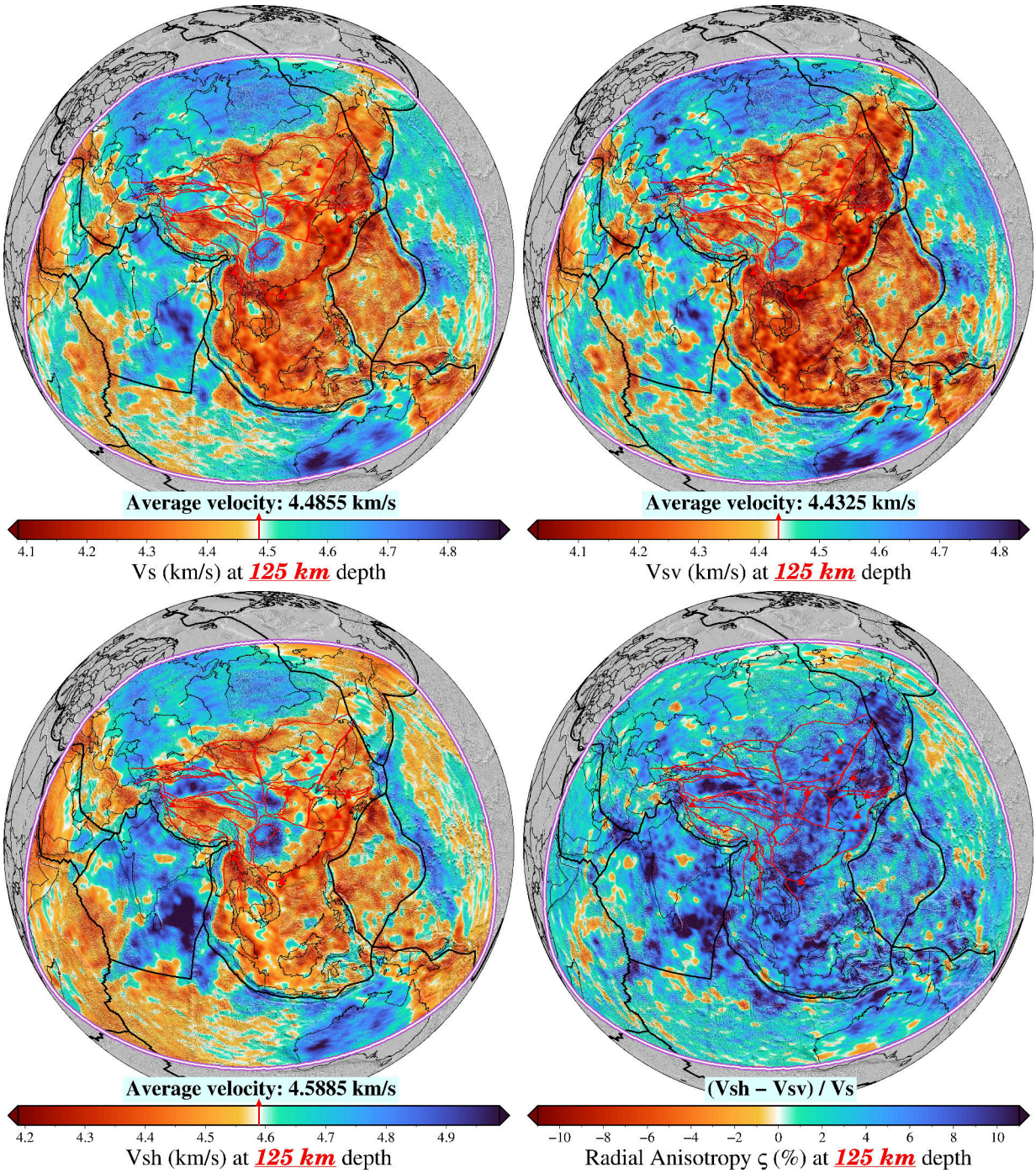

Figure 3.S7: Horizontal slices through ***SinoScope 1.0*** showing the absolute isotropic shear wave velocity (V_S), vertically and horizontally polarized S-wave velocities (V_{SV}, V_{SH}), and radial anisotropy (ξ) at **125** km depth. The dark bold lines delineate the major plate boundaries, and the red lines define main tectonic units, basins, and large fault zones.

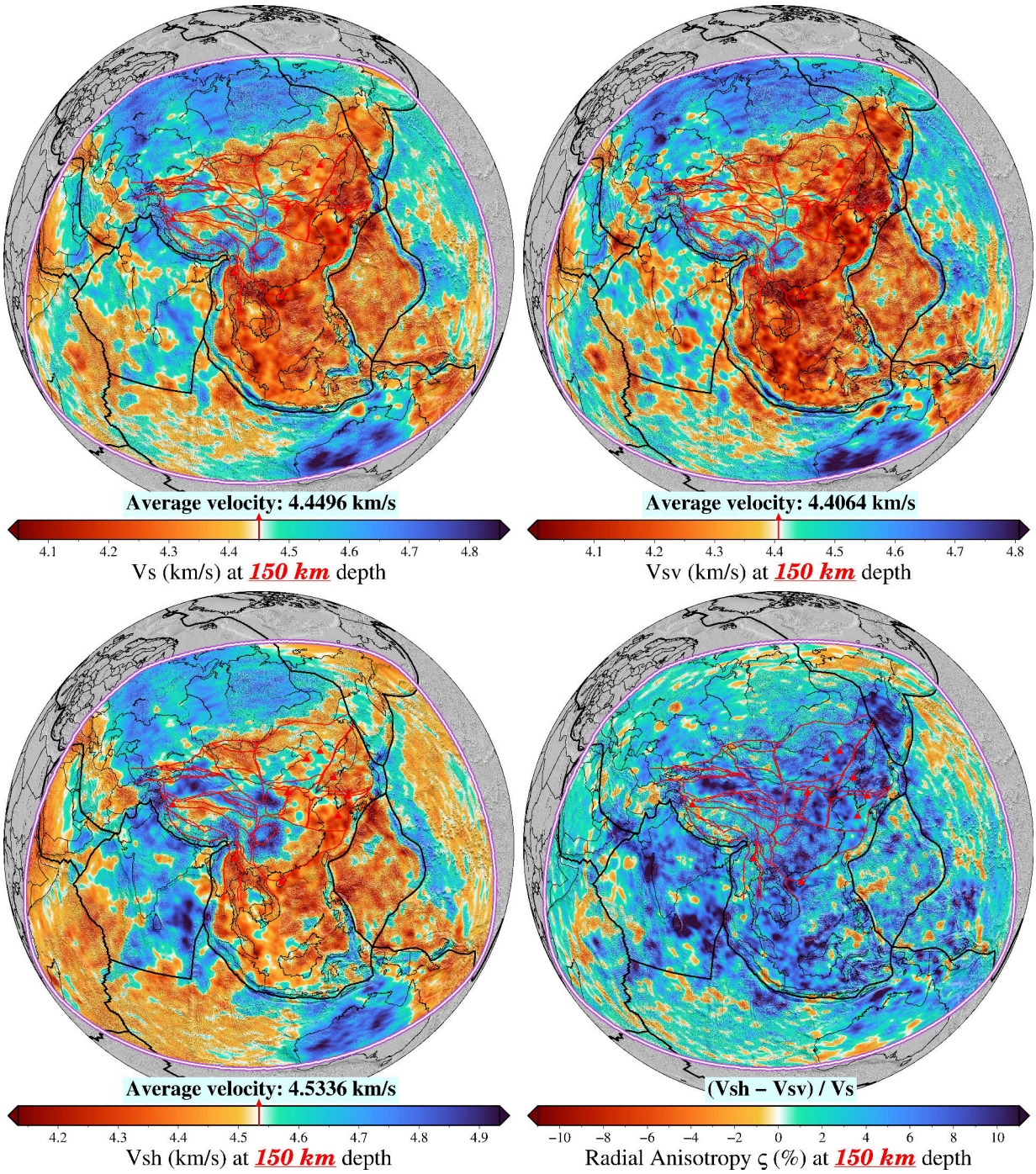

Figure 3.S8: Horizontal slices through ***SinoScope 1.0*** showing the absolute isotropic shear wave velocity (V_S), vertically and horizontally polarized S-wave velocities (V_{SV}, V_{SH}), and radial anisotropy (ξ) at **150** km depth. The dark bold lines delineate the major plate boundaries, and the red lines define main tectonic units, basins, and large fault zones.

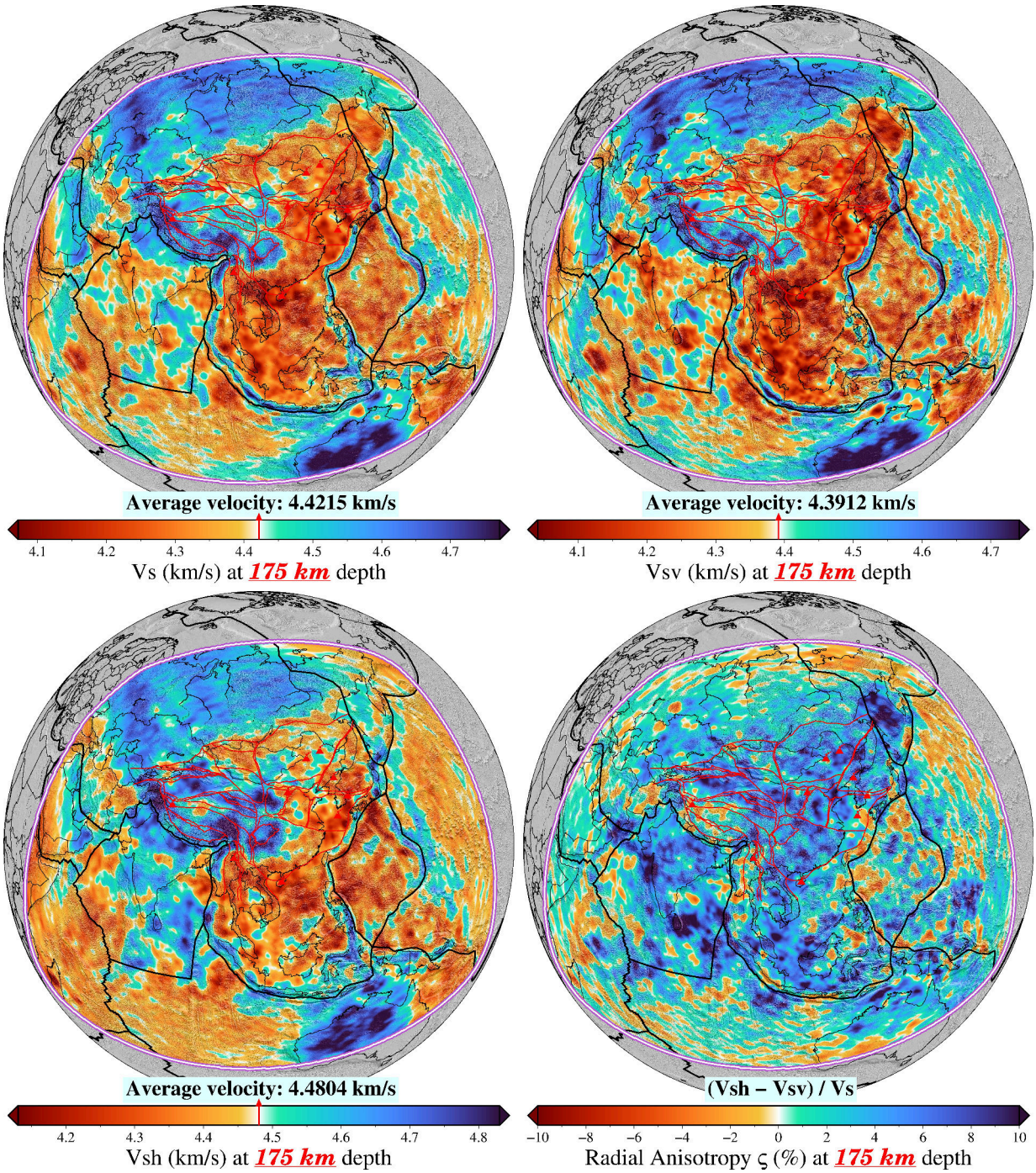

Figure 3.S9: Horizontal slices through ***SinoScope 1.0*** showing the absolute isotropic shear wave velocity (V_S), vertically and horizontally polarized S-wave velocities (V_{SV}, V_{SH}), and radial anisotropy (ξ) at **175** km depth. The dark bold lines delineate the major plate boundaries, and the red lines define main tectonic units, basins, and large fault zones.

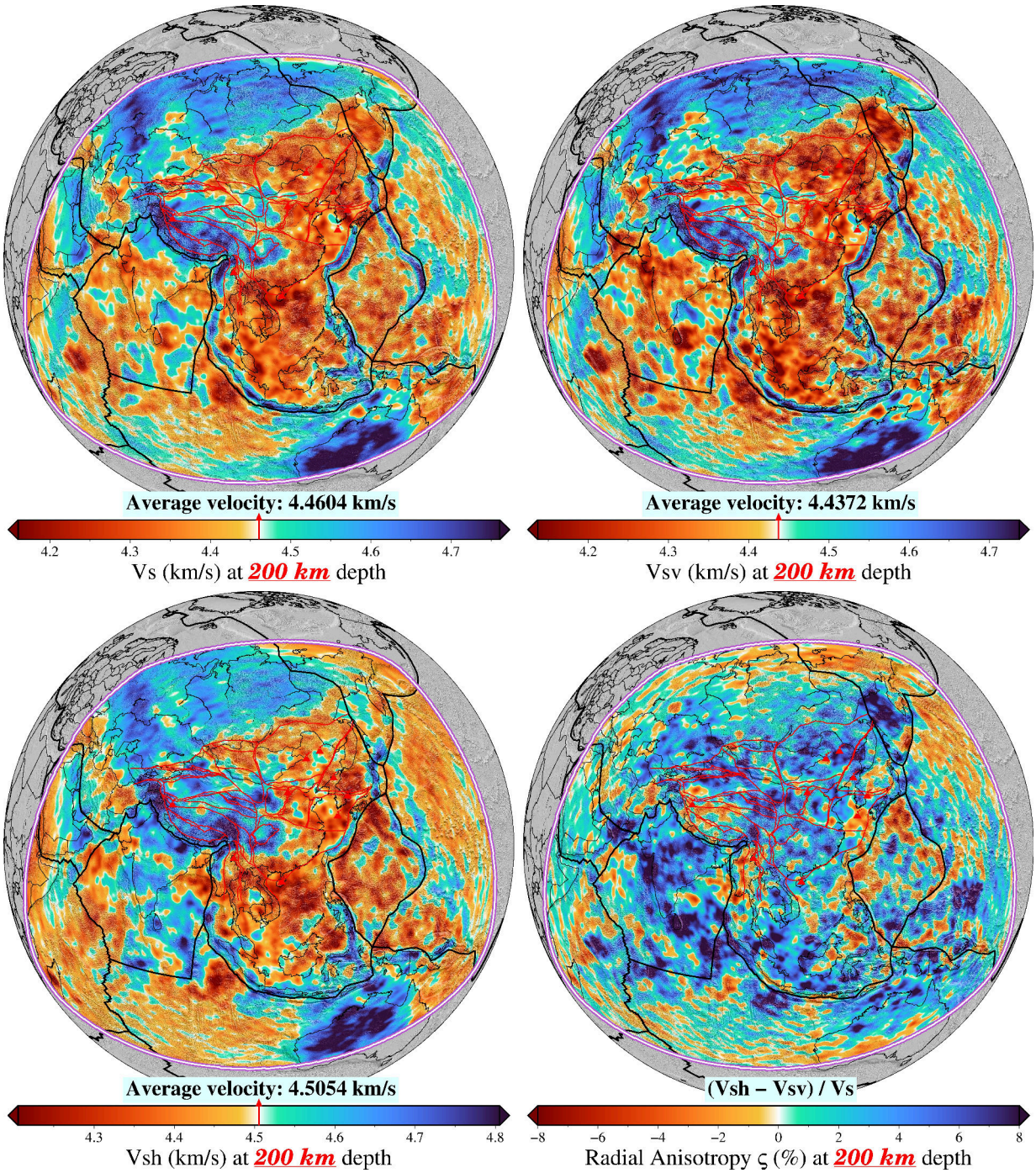

Figure 3.S10: Horizontal slices through ***SinoScope 1.0*** showing the absolute isotropic shear wave velocity (V_S), vertically and horizontally polarized S-wave velocities (V_{SV}, V_{SH}), and radial anisotropy (ξ) at **200** km depth. The dark bold lines delineate the major plate boundaries, and the red lines define main tectonic units, basins, and large fault zones.

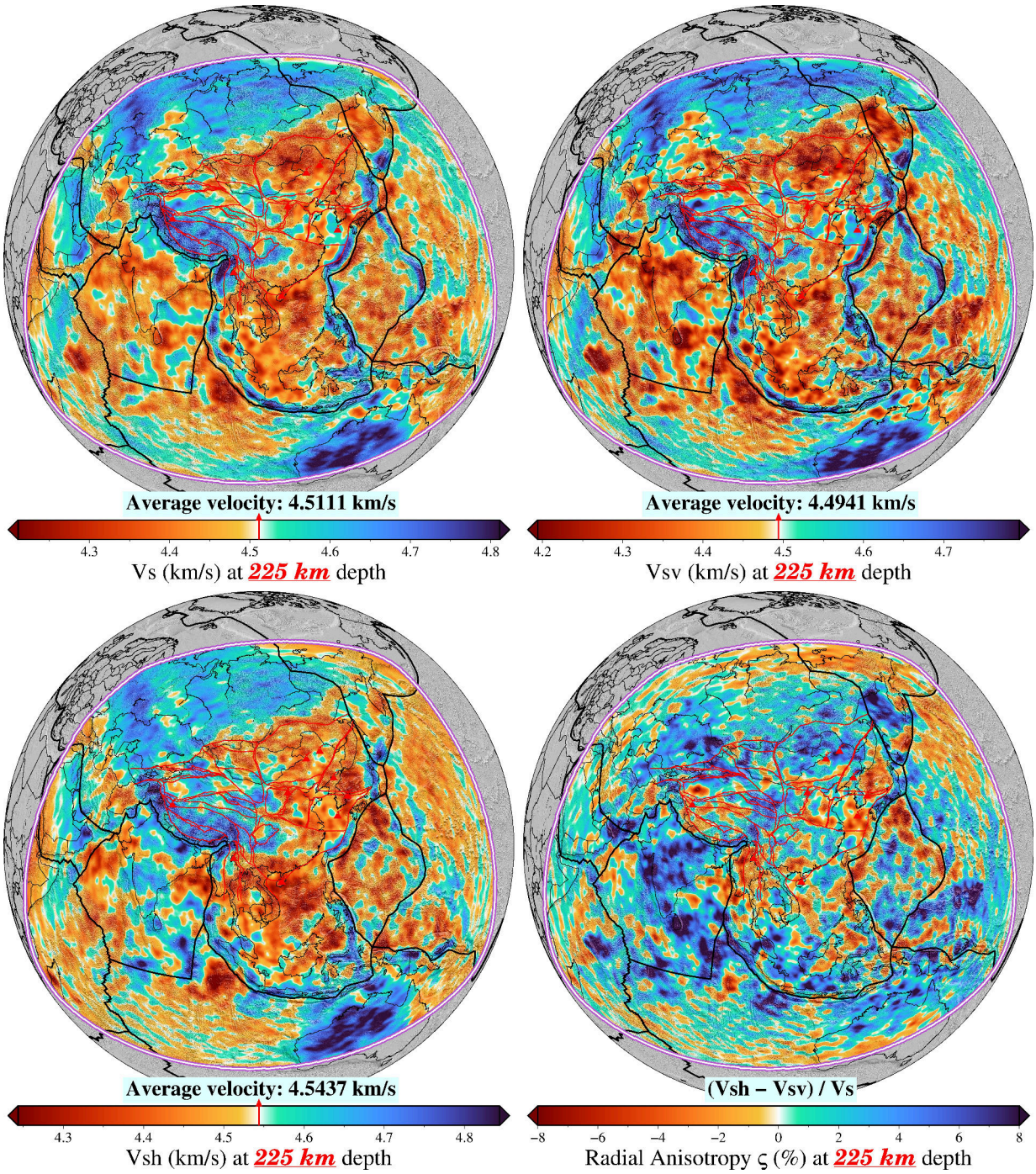

Figure 3.S11: Horizontal slices through ***SinoScope 1.0*** showing the absolute isotropic shear wave velocity (V_S), vertically and horizontally polarized S-wave velocities (V_{SV}, V_{SH}), and radial anisotropy (ξ) at **225** km depth. The dark bold lines delineate the major plate boundaries, and the red lines define main tectonic units, basins, and large fault zones.

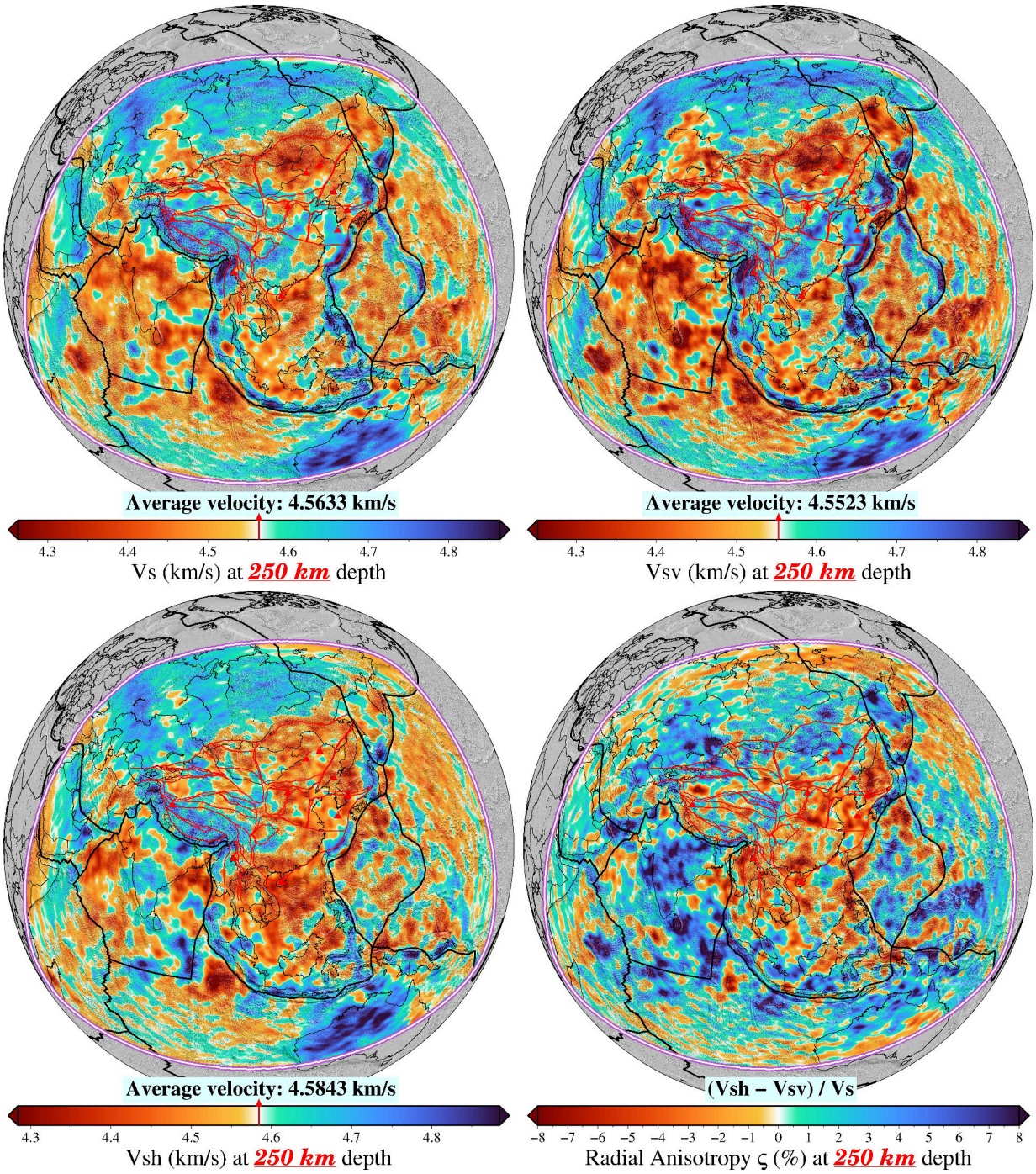

Figure 3.S12: Horizontal slices through ***SinoScope 1.0*** showing the absolute isotropic shear wave velocity (V_S), vertically and horizontally polarized S-wave velocities (V_{SV}, V_{SH}), and radial anisotropy (ξ) at **250** km depth. The dark bold lines delineate the major plate boundaries, and the red lines define main tectonic units, basins, and large fault zones.

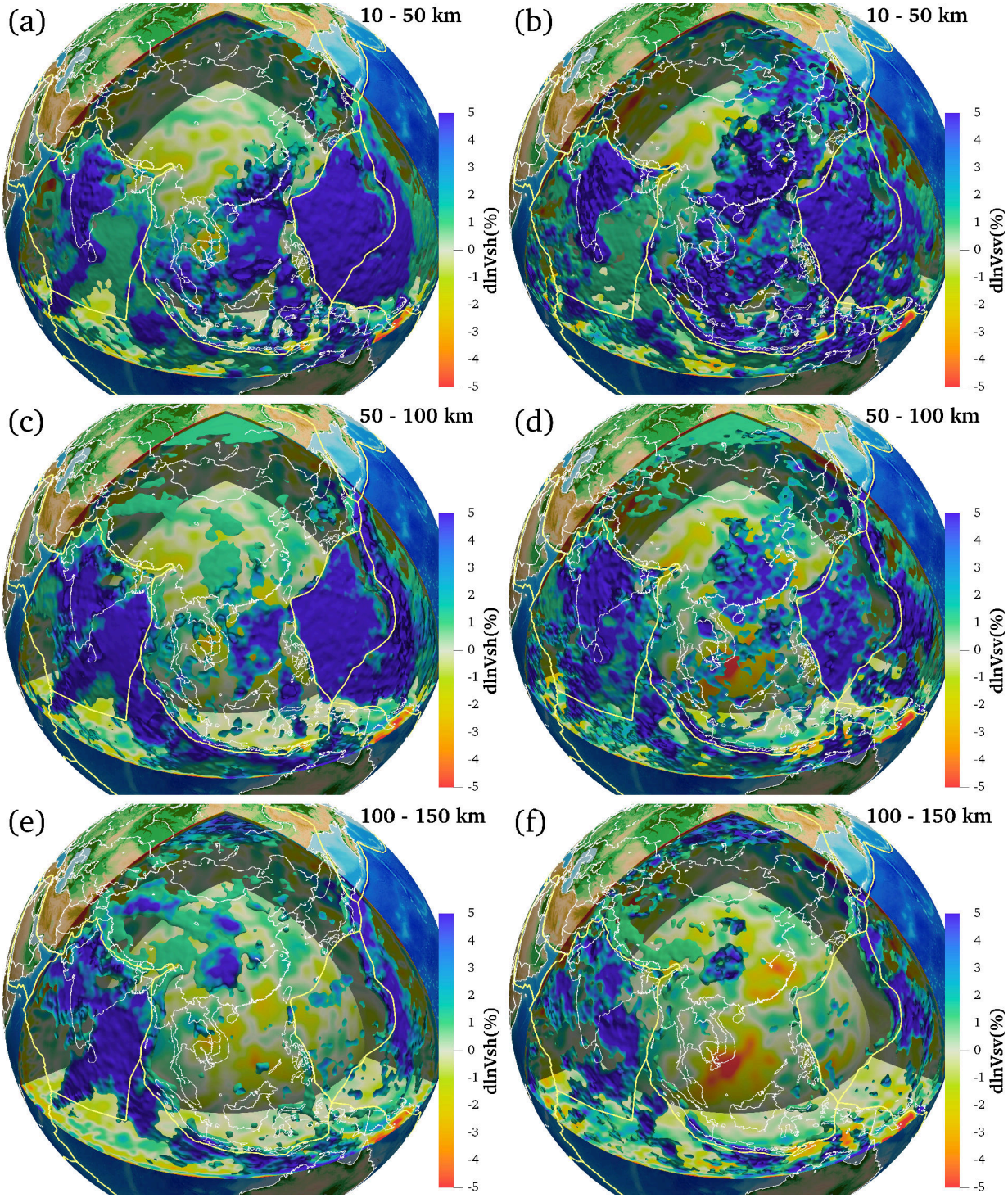

Figure 3.S13: 3-D visualizations of the fast horizontally (a, c, e) and vertically (b, d, f) polarized shear wave velocity structure (with V_{SH} and V_{SV} perturbations $\geq$ 1.25%) at depths of 10-150 km, with the spherical lower boundaries corresponding to 2,000 km depth.

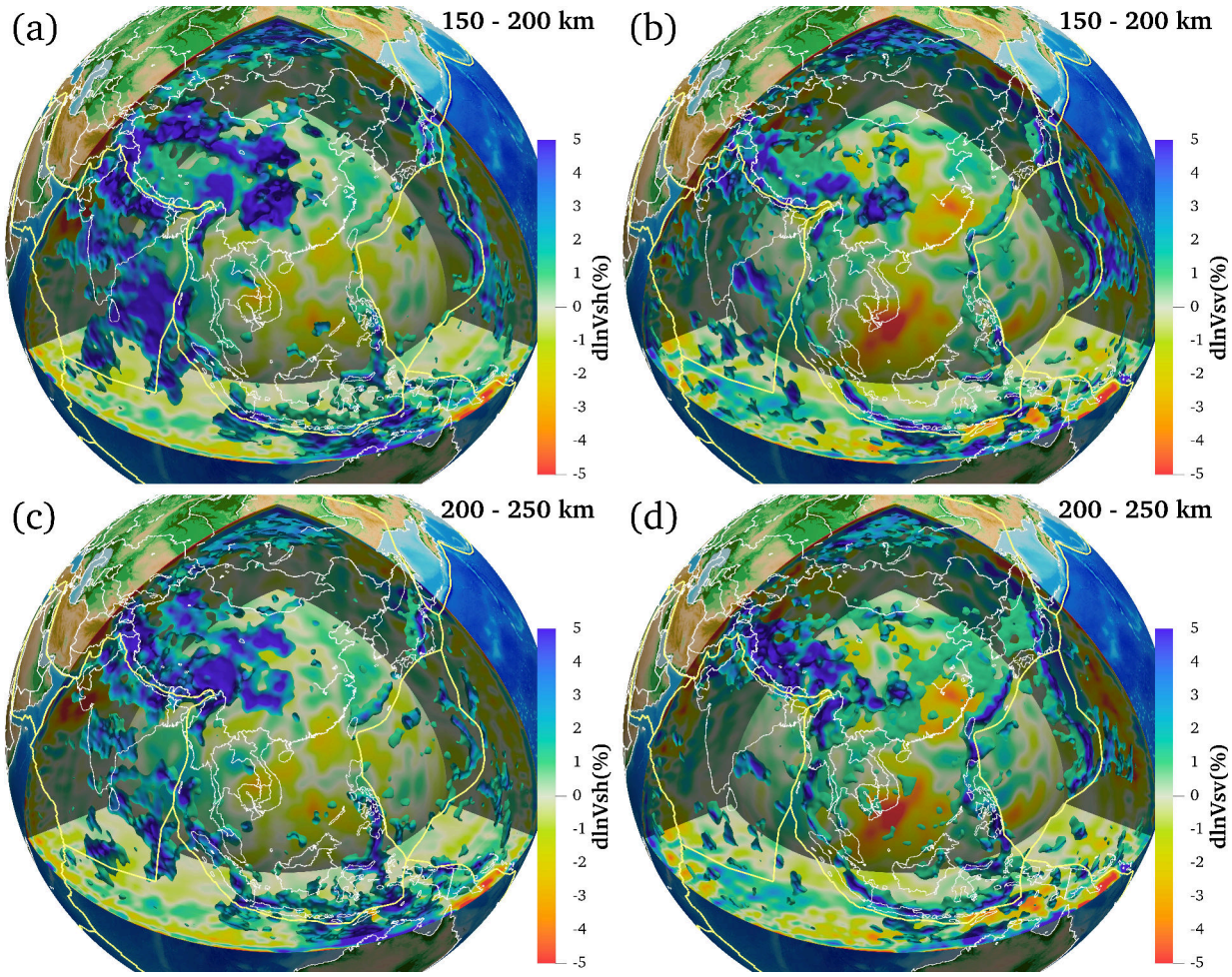

Figure 3.S14: 3-D visualizations of the fast horizontally (a, c) and vertically (b, d) polarized shear wave velocity structure (with V_{SH} and V_{SV} perturbations $\geq 1.25\%$) at depths of 150-250 km, with the spherical lower boundaries corresponding to 2,000 km depth.

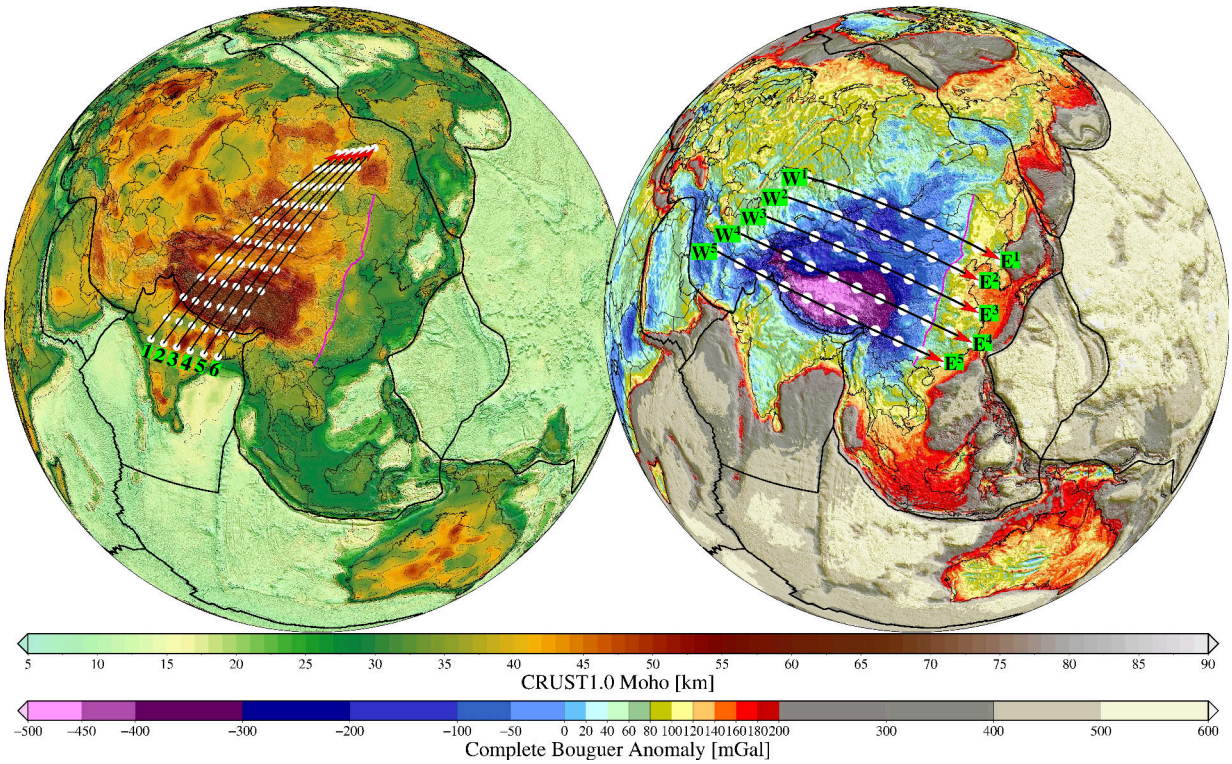

Figure 3.S15: Global map of the Moho depths from CRUST1.0 (left; Laske et al., 2013) and Bouguer gravity map from the WGM2012 model (right; Bonvalot et al., 2012). Locations of the north-south cross-sections are shown as black lines with white dots crossing the India-Eurasia collision zone in Figure 3.S16 - 3.S21. Locations of the west-east cross-sections are shown as black lines with white dots crossing the continental lithosphere in the eastern Eurasian Plate in Figure 3.S22 - 3.S26. The solid magenta line denotes the North-South Gravity Lineament. White dots along the lines are marked every 5°.

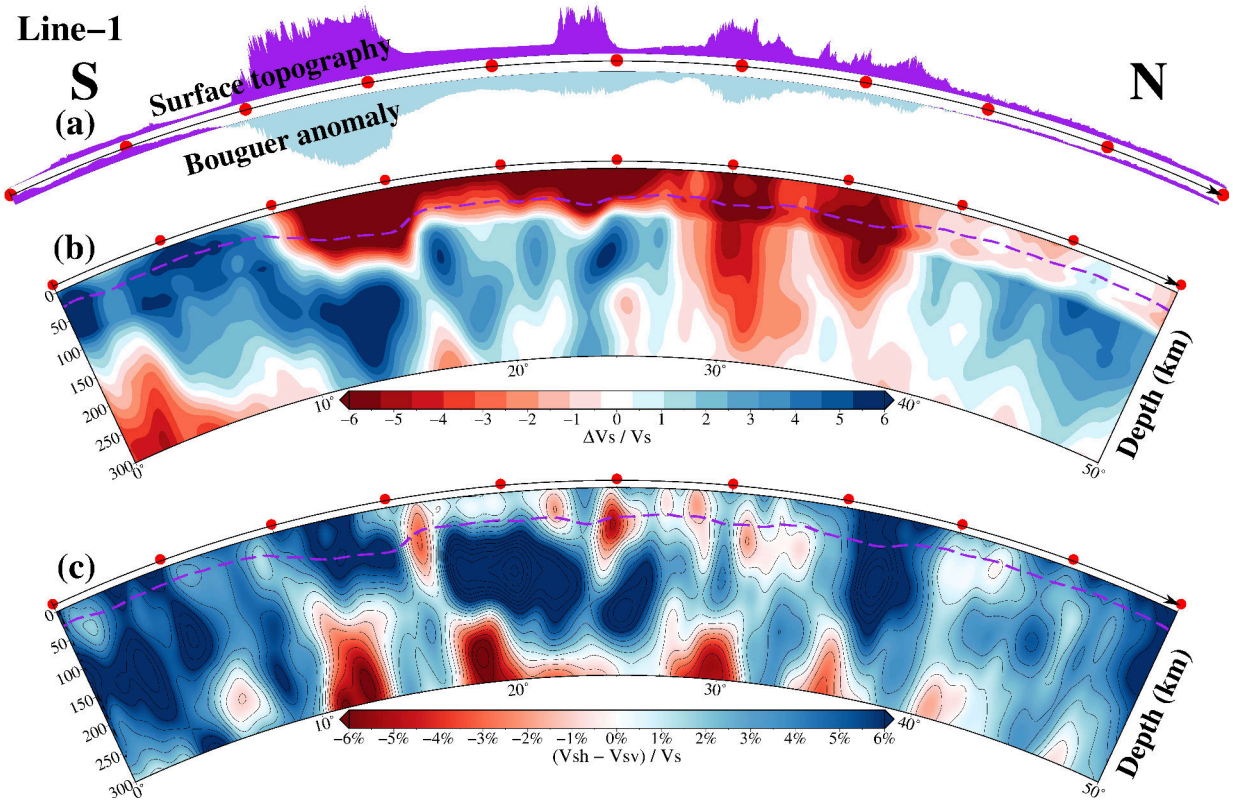

Figure 3.S16: (a) The surface topography (top) and the Bouguer gravity anomaly (bottom) from the WGM2012 model (Bonvalot et al., 2012) along the profile (Line: 1) shown in Figure 3.S15. Purple and light blue colors denote positive and negative values of the elevation and Bouguer anomaly, respectively. (b) - (c) Cross-sections are shown for the isotropic shear-wave velocity perturbation (δlnV_S) in % relative to the depth-average from ***SinoScope 1.0*** (Ma et al., 2022), and radial shear-wave anisotropy (ξ). The dashed magenta lines indicate the Moho depth estimated from ***SinoScope 1.0*** (Ma et al., 2022). Red dots on the frame of each cross-section are marked every 5°.

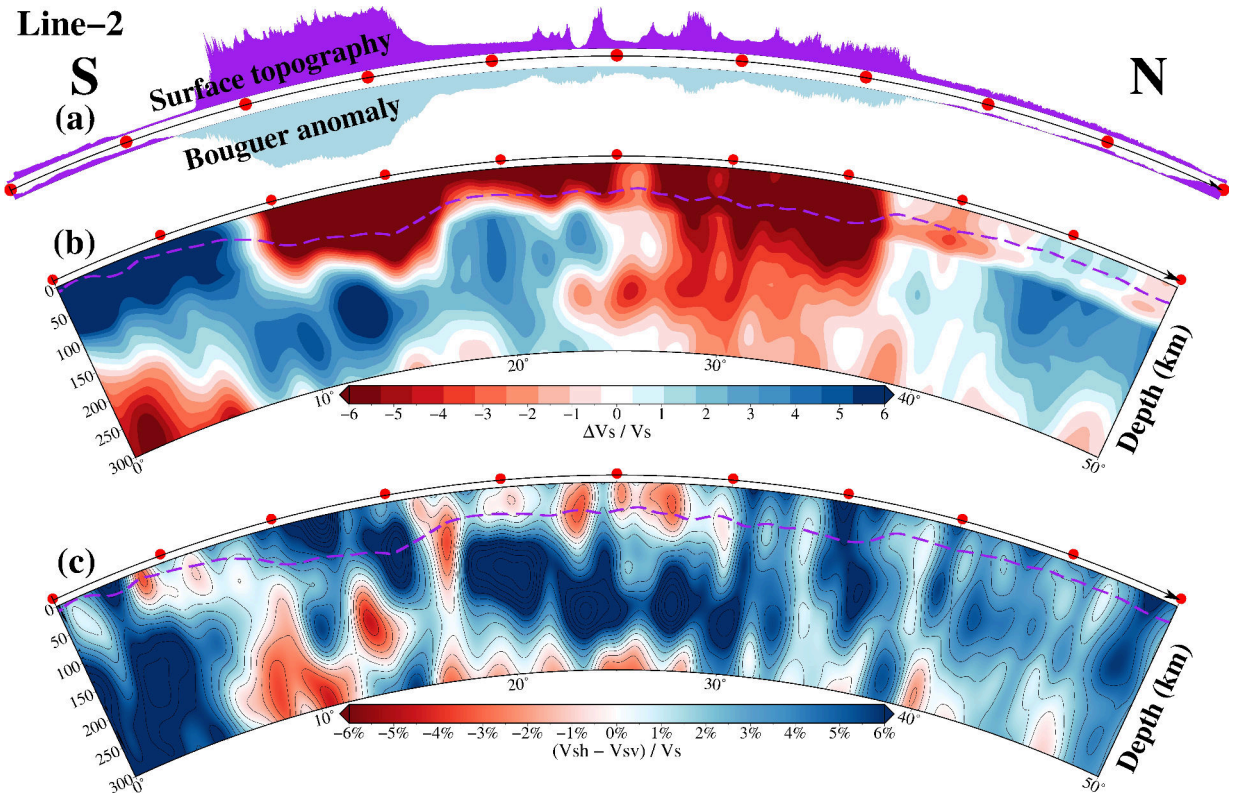

Figure 3.S17: (a) The surface topography (top) and the Bouguer gravity anomaly (bottom) from the WGM2012 model (Bonvalot et al., 2012) along the profile (Line: 2) shown in Figure 3.S15. Purple and light blue colors denote positive and negative values of the elevation and Bouguer anomaly, respectively. (b) - (c) Cross-sections are shown for the isotropic shear-wave velocity perturbation (δlnV_S) in % relative to the depth-average from ***SinoScope 1.0*** (Ma et al., 2022), and radial shear-wave anisotropy (ξ). The dashed magenta lines indicate the Moho depth estimated from ***SinoScope 1.0*** (Ma et al., 2022). Red dots on the frame of each cross-section are marked every 5°.

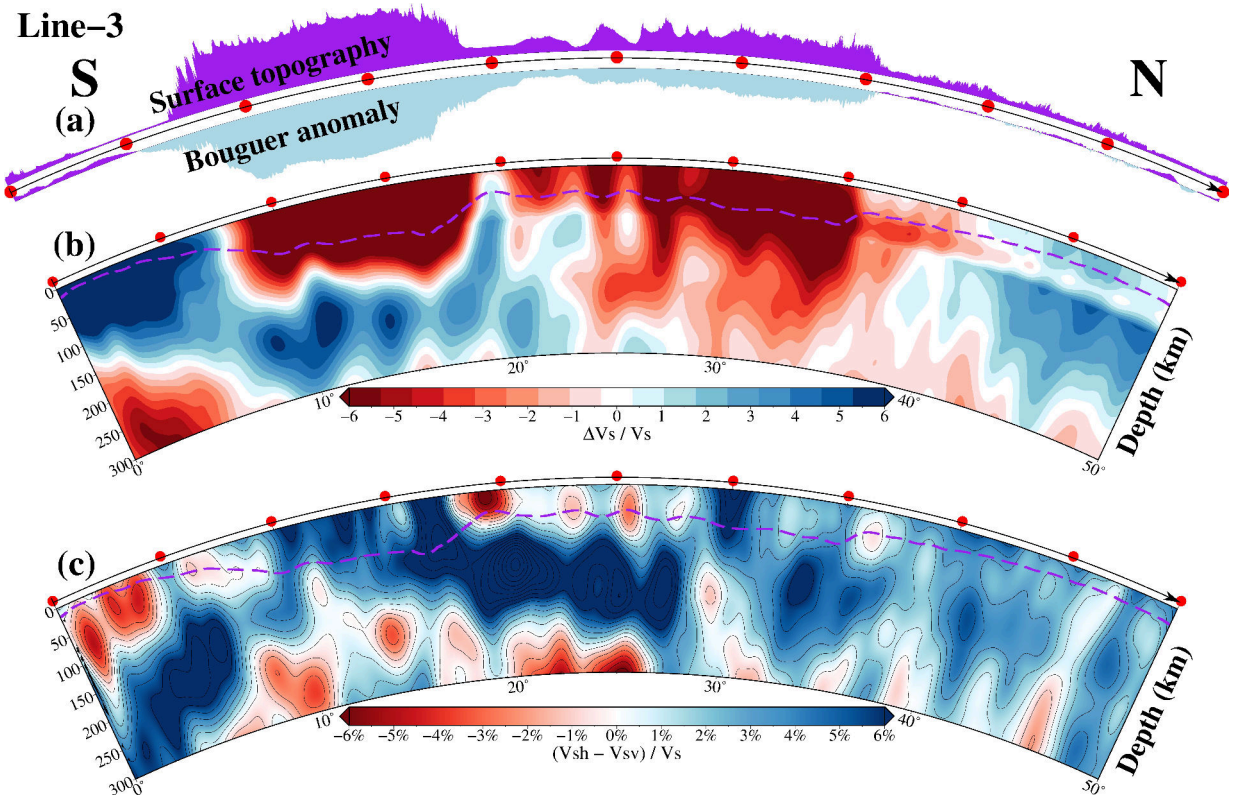

Figure 3.S18: (a) The surface topography (top) and the Bouguer gravity anomaly (bottom) from the WGM2012 model (Bonvalot et al., 2012) along the profile (Line: 3) shown in Figure 3.S15. Purple and light blue colors denote positive and negative values of the elevation and Bouguer anomaly, respectively. (b) - (c) Cross-sections are shown for the isotropic shear-wave velocity perturbation (δlnV_S) in % relative to the depth-average from ***SinoScope 1.0*** (Ma et al., 2022), and radial shear-wave anisotropy (ξ). The dashed magenta lines indicate the Moho depth estimated from ***SinoScope 1.0*** (Ma et al., 2022). Red dots on the frame of each cross-section are marked every 5°.

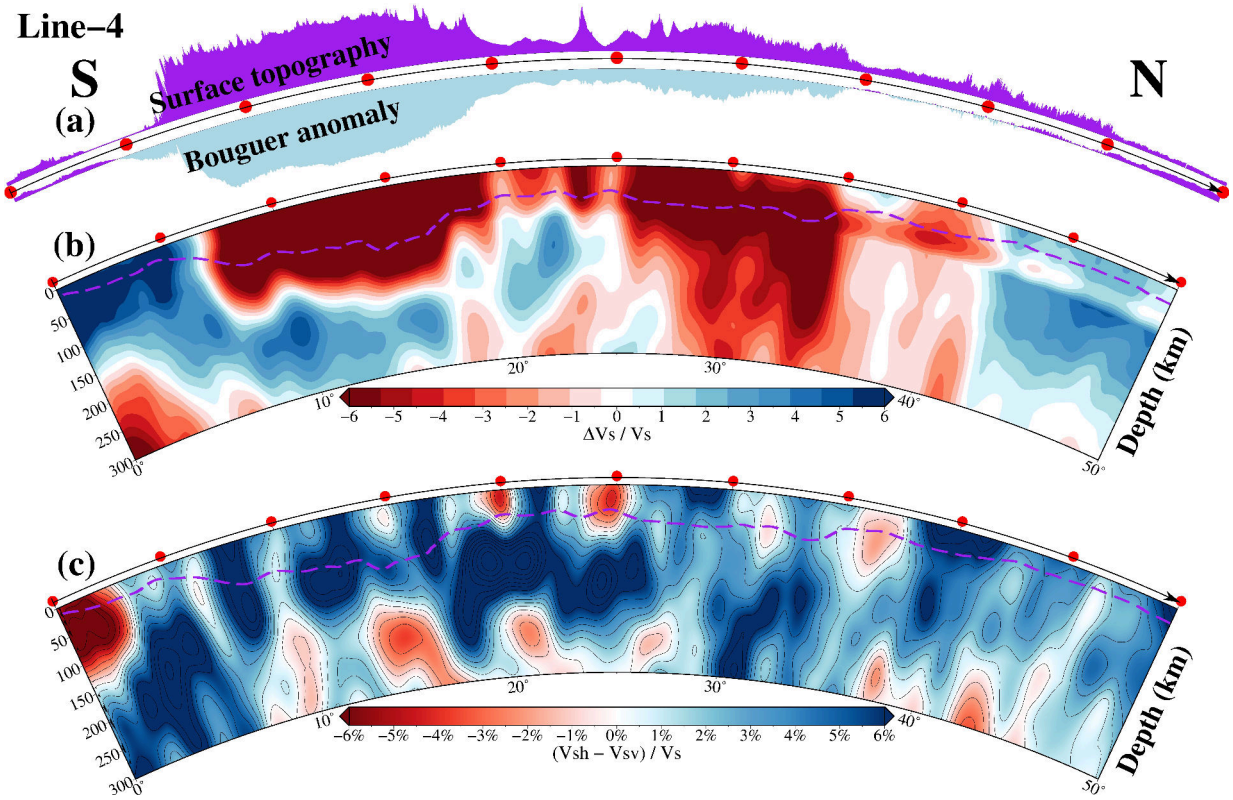

Figure 3.S19: (a) The surface topography (top) and the Bouguer gravity anomaly (bottom) from the WGM2012 model (Bonvalot et al., 2012) along the profile (Line: 4) shown in Figure 3.S15. Purple and light blue colors denote positive and negative values of the elevation and Bouguer anomaly, respectively. (b) - (c) Cross-sections are shown for the isotropic shear-wave velocity perturbation (δlnV_S) in % relative to the depth-average from ***SinoScope 1.0*** (Ma et al., 2022), and radial shear-wave anisotropy (ξ). The dashed magenta lines indicate the Moho depth estimated from ***SinoScope 1.0*** (Ma et al., 2022). Red dots on the frame of each cross-section are marked every 5°.

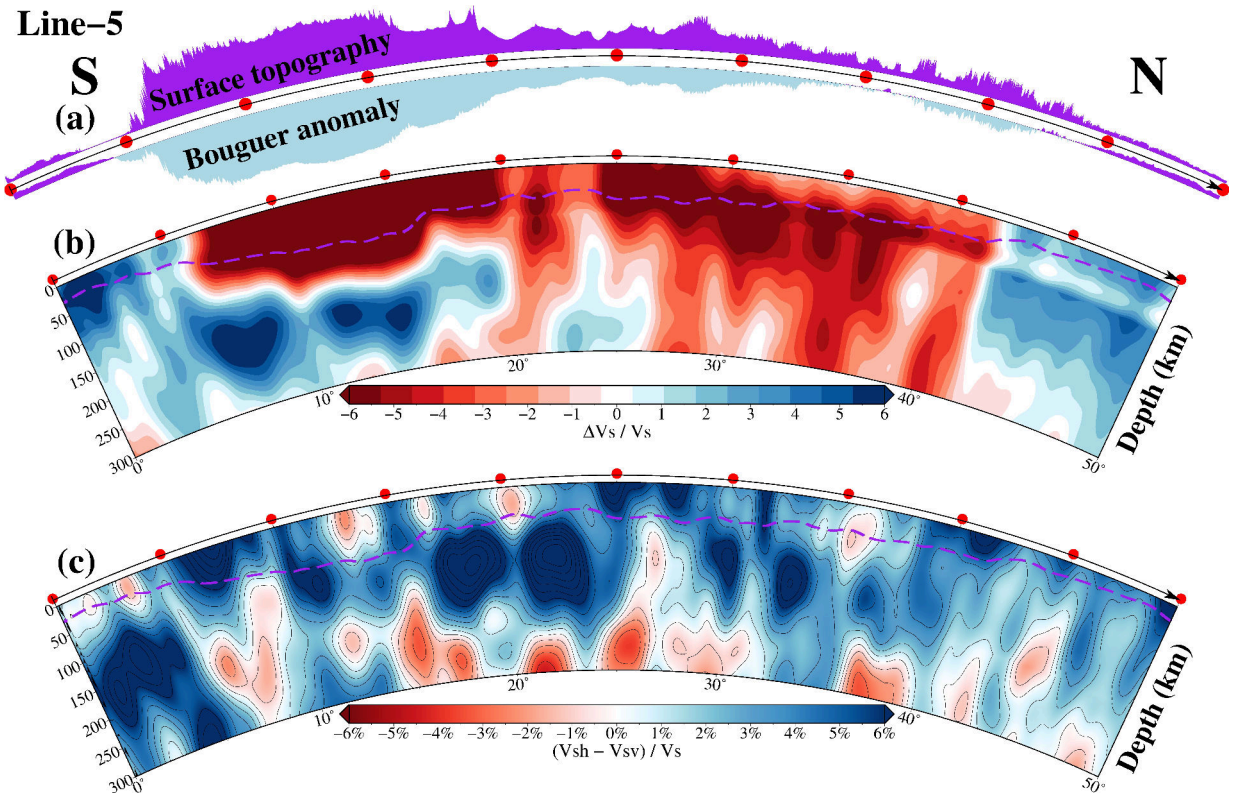

Figure 3.S20: (a) The surface topography (top) and the Bouguer gravity anomaly (bottom) from the WGM2012 model (Bonvalot et al., 2012) along the profile (Line: 5) shown in Figure 3.S15. Purple and light blue colors denote positive and negative values of the elevation and Bouguer anomaly, respectively. (b) - (c) Cross-sections are shown for the isotropic shear-wave velocity perturbation (δlnV_S) in % relative to the depth-average from ***SinoScope 1.0*** (Ma et al., 2022), and radial shear-wave anisotropy (ξ). The dashed magenta lines indicate the Moho depth estimated from ***SinoScope 1.0*** (Ma et al., 2022). Red dots on the frame of each cross-section are marked every 5°.

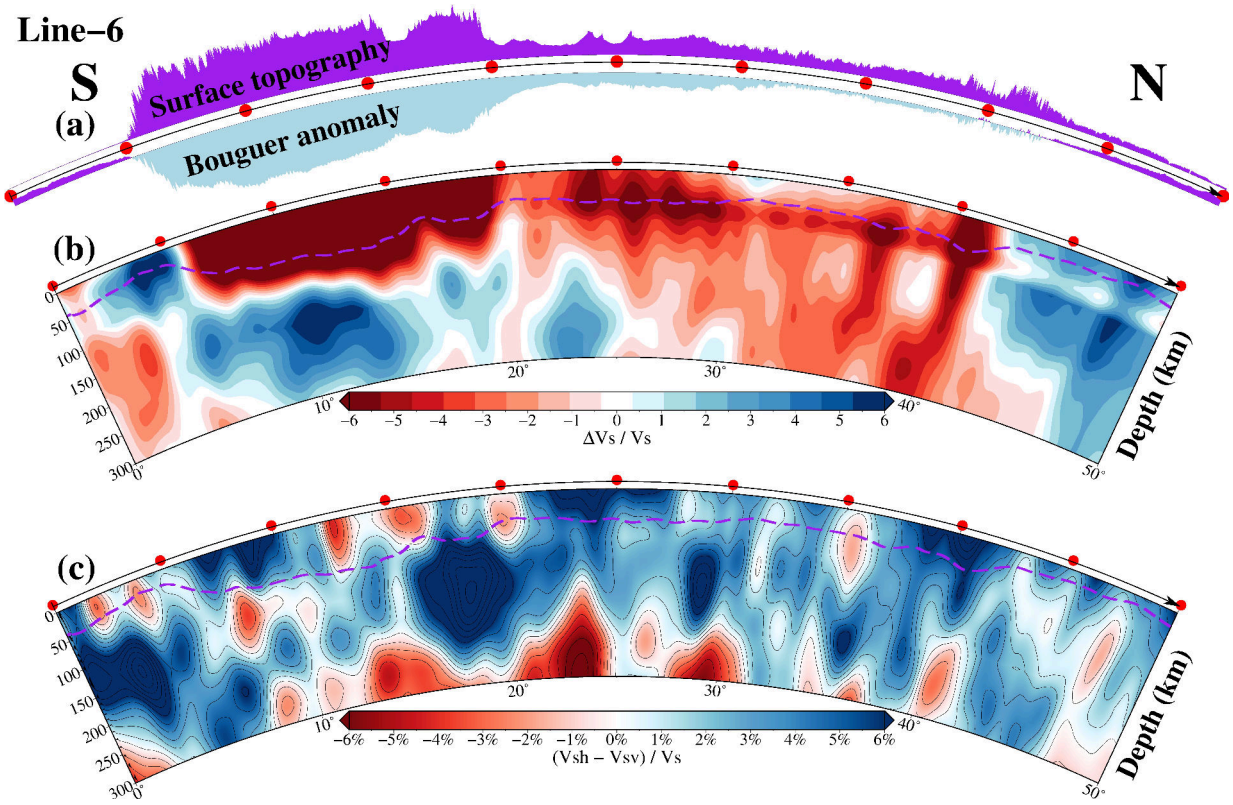

Figure 3.S21: (a) The surface topography (top) and the Bouguer gravity anomaly (bottom) from the WGM2012 model (Bonvalot et al., 2012) along the profile (Line: 6) shown in Figure 3.S15. Purple and light blue colors denote positive and negative values of the elevation and Bouguer anomaly, respectively. (b) - (c) Cross-sections are shown for the isotropic shear-wave velocity perturbation (δlnV_S) in % relative to the depth-average from ***SinoScope 1.0*** (Ma et al., 2022), and radial shear-wave anisotropy (ξ). The dashed magenta lines indicate the Moho depth estimated from ***SinoScope 1.0*** (Ma et al., 2022). Red dots on the frame of each cross-section are marked every 5°.

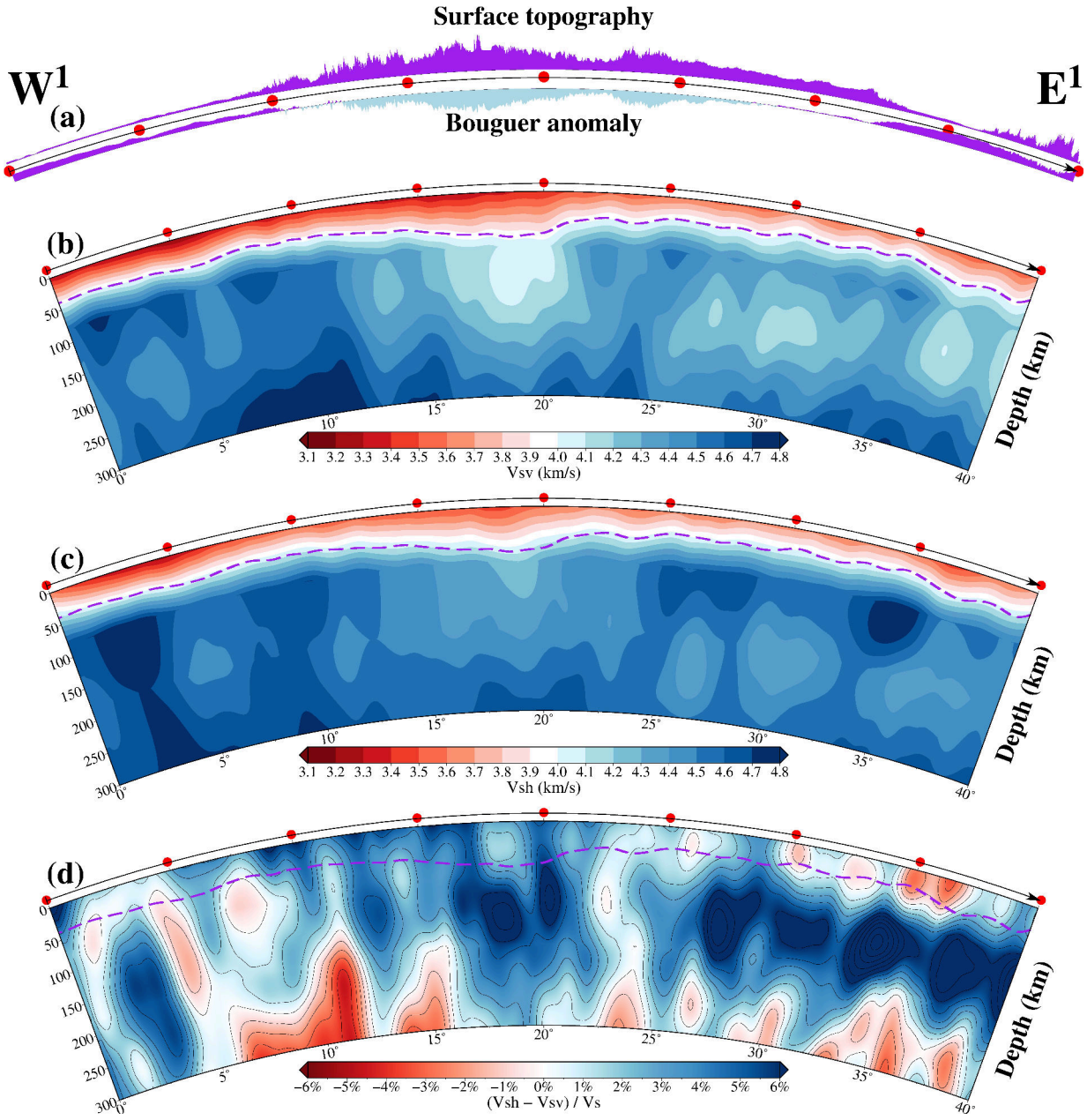

Figure 3.S22: (a) The surface topography (top) and the Bouguer gravity anomaly (bottom) from the WGM2012 model (Bonvalot et al., 2012) along the profile W1-E1 shown in Figure 3.S15. Purple and light blue colors denote positive and negative values of the elevation and Bouguer anomaly, respectively. (b) - (d) Cross sections are shown for the absolute vertically polarized shear-wave velocity (V_{SV}), the absolute horizontally polarized shear-wave velocity (V_{SH}), and radial shear-wave anisotropy (ξ). The dashed magenta lines indicate the Moho depth estimated from ***SinoScope 1.0*** (Ma et al., 2022). Red dots on the frame of each cross-section are marked every 5°.

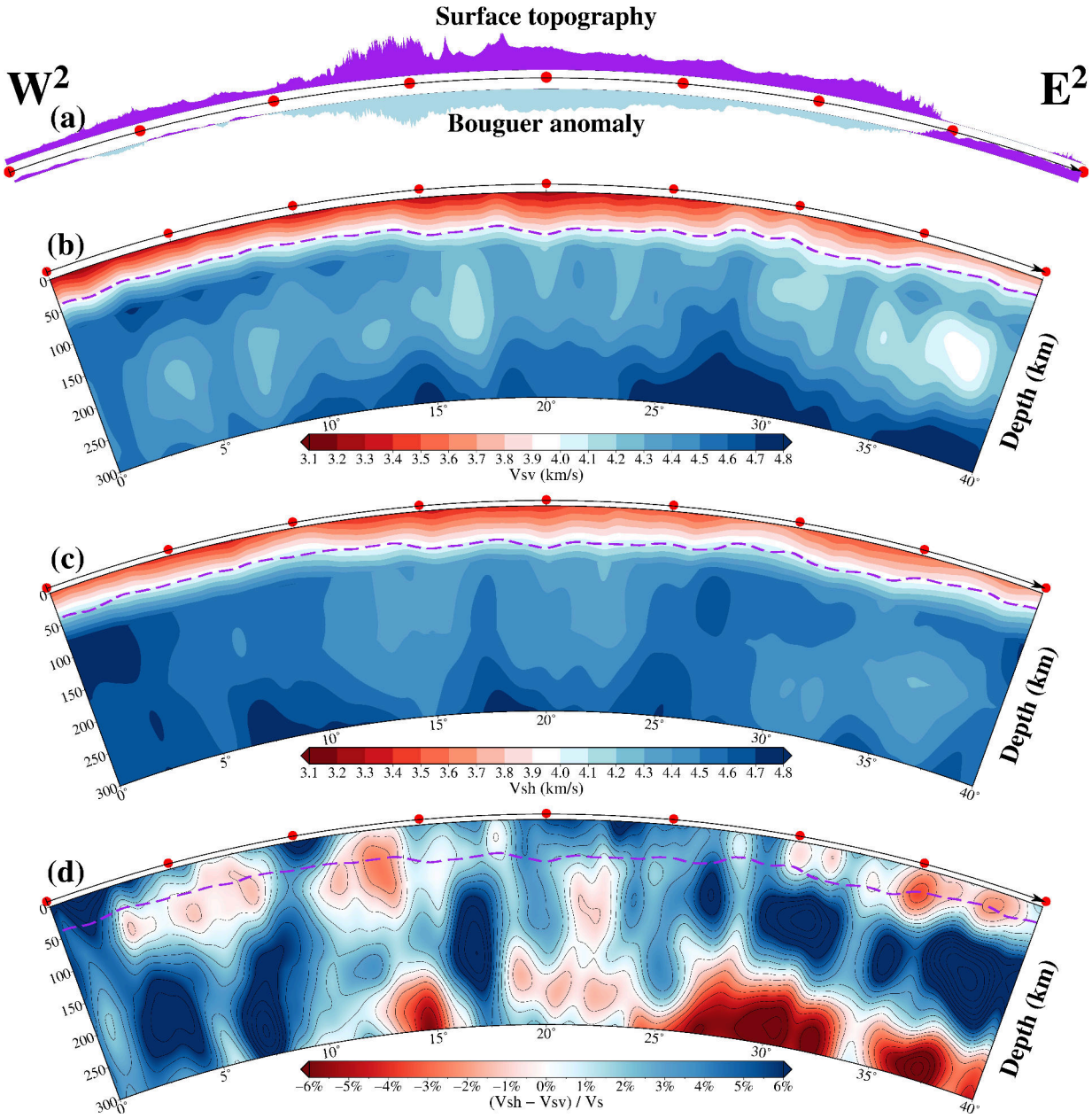

Figure 3.S23: (a) The surface topography (top) and the Bouguer gravity anomaly (bottom) from the WGM2012 model (Bonvalot et al., 2012) along the profile W2-E2 shown in Figure 3.S15. Purple and light blue colors denote positive and negative values of the elevation and Bouguer anomaly, respectively. (b) - (d) Cross sections are shown for the absolute vertically polarized shear-wave velocity (V_{SV}), the absolute horizontally polarized shear-wave velocity (V_{SH}), and radial shear-wave anisotropy (ξ). The dashed magenta lines indicate the Moho depth estimated from ***SinoScope 1.0*** (Ma et al., 2022). Red dots on the frame of each cross-section are marked every 5°.

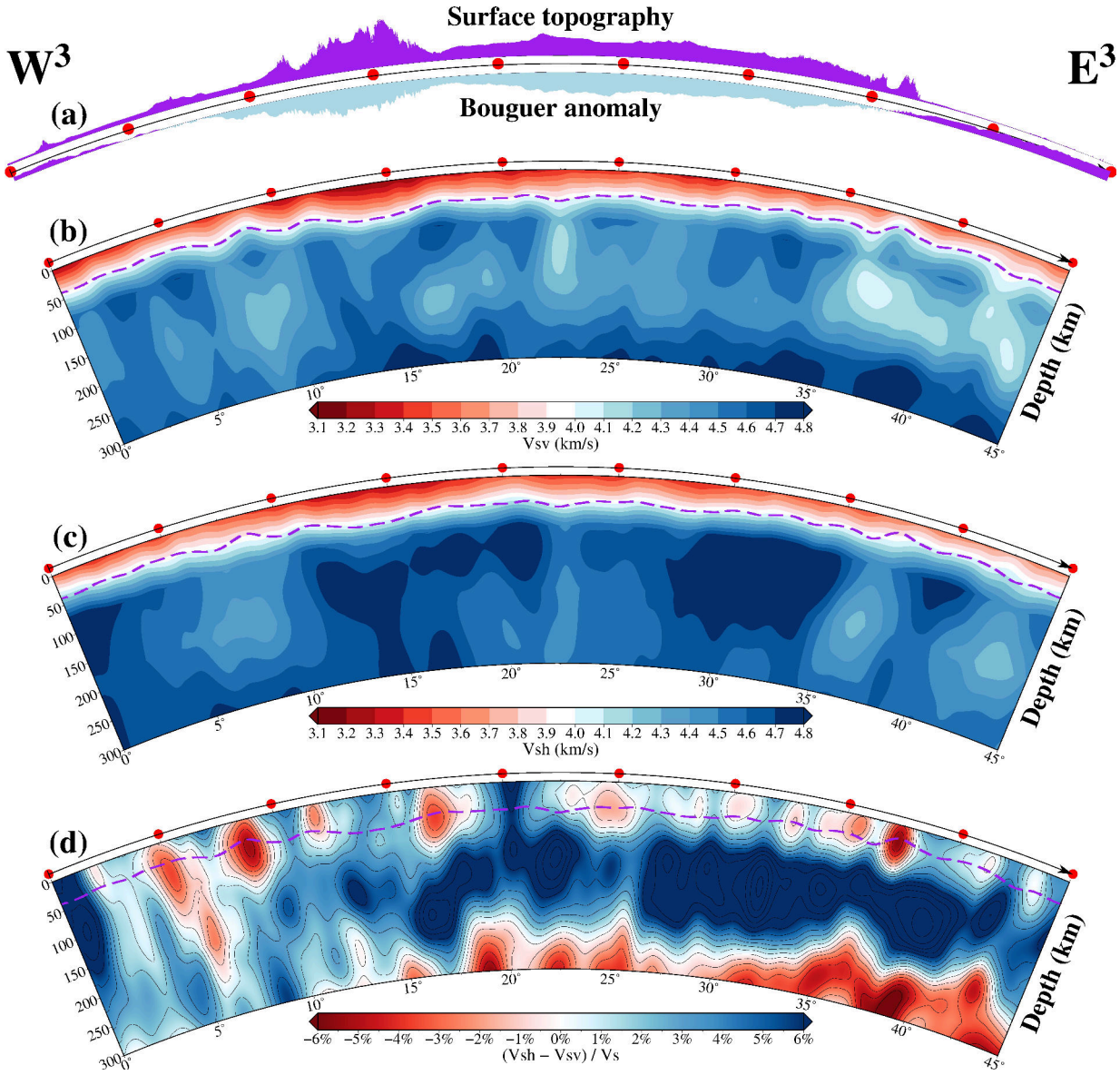

Figure 3.S24: (a) The surface topography (top) and the Bouguer gravity anomaly (bottom) from the WGM2012 model (Bonvalot et al., 2012) along the profile W3-E3 shown in Figure 3.S15. Purple and light blue colors denote positive and negative values of the elevation and Bouguer anomaly, respectively. (b) - (d) Cross sections are shown for the absolute vertically polarized shear-wave velocity (V_{SV}), the absolute horizontally polarized shear-wave velocity (V_{SH}), and radial shear-wave anisotropy (ξ). The dashed magenta lines indicate the Moho depth estimated from ***SinoScope 1.0*** (Ma et al., 2022). Red dots on the frame of each cross-section are marked every 5°.

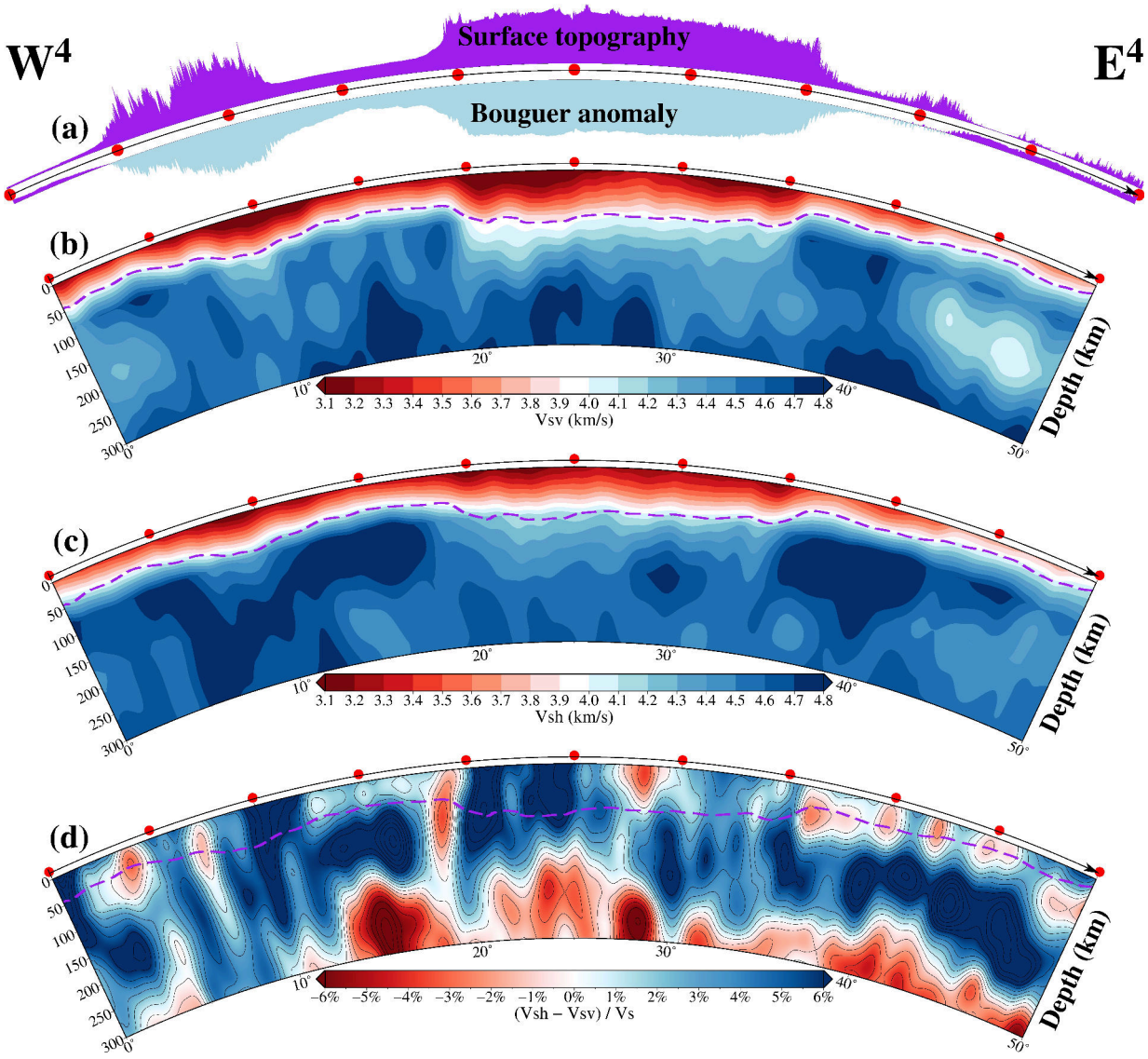

Figure 3.S25: (a) The surface topography (top) and the Bouguer gravity anomaly (bottom) from the WGM2012 model (Bonvalot et al., 2012) along the profile W4-E4 shown in Figure 3.S15. Purple and light blue colors denote positive and negative values of the elevation and Bouguer anomaly, respectively. (b) - (d) Cross sections are shown for the absolute vertically polarized shear-wave velocity (V_{SV}), the absolute horizontally polarized shear-wave velocity (V_{SH}), and radial shear-wave anisotropy (ξ). The dashed magenta lines indicate the Moho depth estimated from ***SinoScope 1.0*** (Ma et al., 2022). Red dots on the frame of each cross-section are marked every 5°.

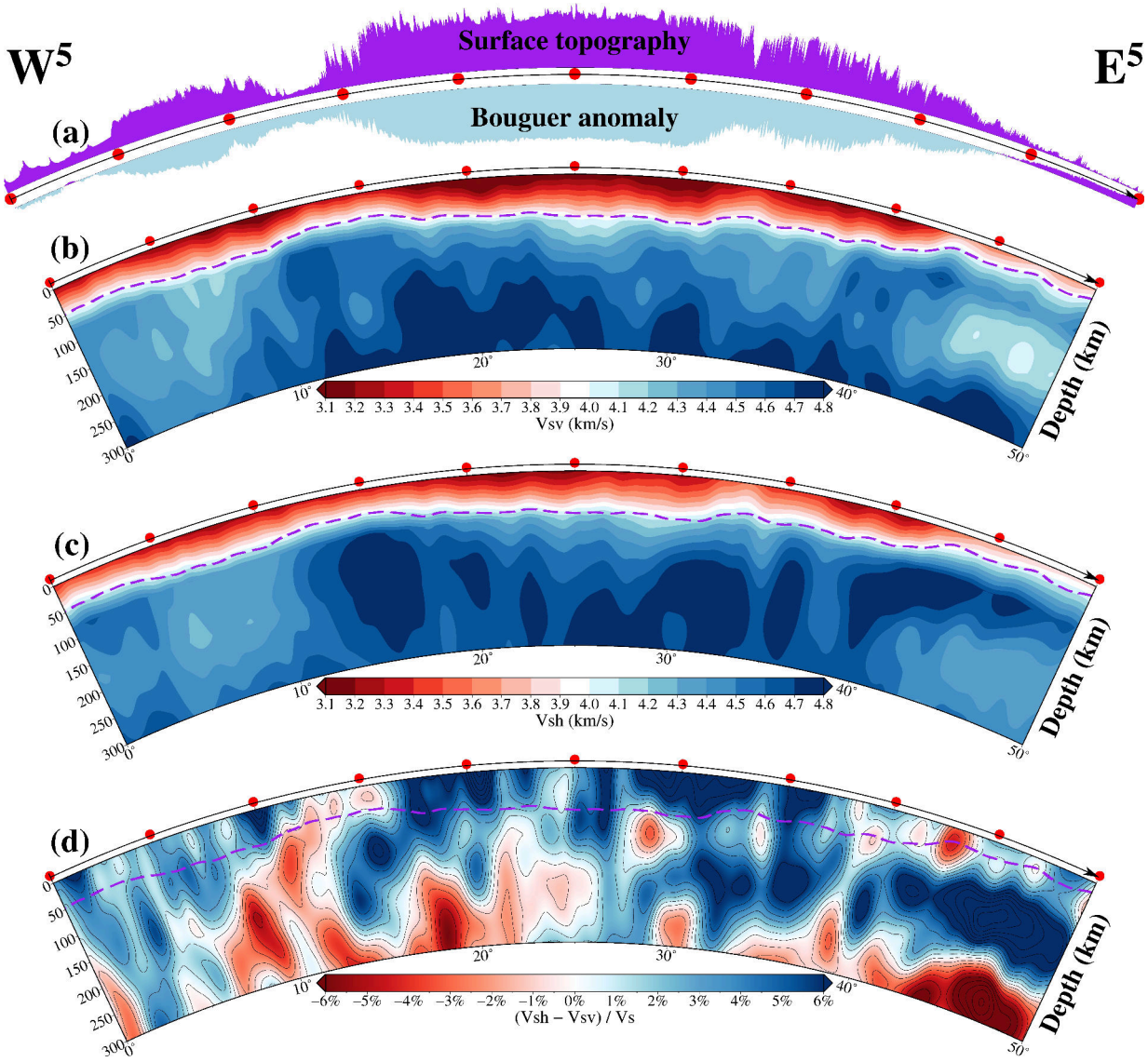

Figure 3.S26: (a) The surface topography (top) and the Bouguer gravity anomaly (bottom) from the WGM2012 model (Bonvalot et al., 2012) along the profile W5-E5 shown in Figure 3.S15. Purple and light blue colors denote positive and negative values of the elevation and Bouguer anomaly, respectively. (b) - (d) Cross sections are shown for the absolute vertically polarized shear-wave velocity (V_{SV}), the absolute horizontally polarized shear-wave velocity (V_{SH}), and radial shear-wave anisotropy (ξ). The dashed magenta lines indicate the Moho depth estimated from ***SinoScope 1.0*** (Ma et al., 2022). Red dots on the frame of each cross-section are marked every 5°.

Reference

Beaumont, C., Jamieson, R. A., Nguyen, M. and Lee, B. (2001). Himalayan tectonics explained by extrusion of a low-viscosity crustal channel coupled to focused surface denudation, *Nature* **414**(6865): 738–742.

Bird, P. (2003). An updated digital model of plate boundaries, *Geochemistry, Geophysics, Geosystems* **4**(3).

Bonvalot, S., Balmino, G., Briais, A., Kuhn, M., Peyrefitte, A., Vales, N., Biancale, R., Gabalda, G., Reinquin, F. and Sarrailh, M. (2012). World gravity map, *Commission for the Geological Map of the World* .

Burgos, G., Montagner, J.-P., Beucler, E., Capdeville, Y., Mocquet, A. and Drilleau, M. (2014). Oceanic lithosphere-asthenosphere boundary from surface wave dispersion data, *Journal of Geophysical Research: Solid Earth* **119**(2): 1079–1093.
URL: *https://agupubs.onlinelibrary.wiley.com/doi/abs/10.1002/2013JB010528*

Chang, C. and Zeng, X. (1973). Tectonic features of the mount jolmo lungma region in southern tibet, china, *Chinese Journal of Geology* **8**(1): 1–12.

Cheng, S., Xiao, X., Wu, J., Wang, W., Sun, L., Wang, X. and Wen, L. (2021). Crustal thickness and Vp/Vs variation beneath continental China revealed by receiver function analysis, *Geophysical Journal International* **228**(3): 1731–1749.
URL: *https://doi.org/10.1093/gji/ggab433*

DeCelles, P. G., Robinson, D. M. and Zandt, G. (2002). Implications of shortening in the himalayan fold-thrust belt for uplift of the tibetan plateau, *Tectonics* **21**(6): 12–1–12–25.
URL: *https://agupubs.onlinelibrary.wiley.com/doi/abs/10.1029/2001TC001322*

Dewey, J. (1989). Tectonic evolution of the india eurasia collision zone, *Eclogae Geol. Helv.* **82**: 717–734.

Eaton, D. W., Darbyshire, F., Evans, R. L., Grütter, H., Jones, A. G. and Yuan, X. (2009). The elusive lithosphere–asthenosphere boundary (lab) beneath cratons, *Lithos* **109**(1): 1–22. Continental Lithospheric Mantle: The Petro-Geophysical Approach.
URL: *https://www.sciencedirect.com/science/article/pii/S0024493708001096*

Fichtner, A. (2011). *Full Seismic Waveform Modelling and Inversion*, Springer, Berlin, Heidelberg.

Fichtner, A., Kennett, B. L. and Trampert, J. (2013). Separating intrinsic and apparent anisotropy, *Physics of the Earth and Planetary Interiors* **219**: 11–20.
URL: *https://www.sciencedirect.com/science/article/pii/S0031920113000368*

Gilder, S. A., Gill, J., Coe, R. S., Zhao, X., Liu, Z., Wang, G., Yuan, K., Liu, W., Kuang, G. and Wu, H. (1996). Isotopic and paleomagnetic constraints on the mesozoic tectonic evolution of south china, *Journal of Geophysical Research: Solid Earth* **101**(B7): 16137–16154.
URL: *https://agupubs.onlinelibrary.wiley.com/doi/abs/10.1029/96JB00662*

Hall, R. (2002). Cenozoic geological and plate tectonic evolution of se asia and the sw pacific: computer-based reconstructions, model and animations, *Journal of Asian Earth Sciences* **20**(4): 353–431.

Hall, R. and Spakman, W. (2015). Mantle structure and tectonic history of se asia, *Tectonophysics* **658**: 14–45.
URL: *https://www.sciencedirect.com/science/article/pii/S0040195115003698*

Hao, M., Li, Y. and Zhuang, W. (2019). Crustal movement and strain distribution in east asia revealed by gps observations, *Scientific reports* **9**(1): 1–11.

Harrison, T. M., Grove, M., Lovera, O. M. and Catlos, E. (1998). A model for the origin of himalayan anatexis and inverted metamorphism, *Journal of Geophysical Research: Solid Earth* **103**(B11): 27017–27032.

Hayes, G. P., Moore, G. L., Portner, D. E., Hearne, M., Flamme, H., Furtney, M. and Smoczyk, G. M. (2018). Slab2, a comprehensive subduction zone geometry model, *Science* **362**(6410): 58–61.

He, R., Shang, X., Yu, C., Zhang, H. and Van der Hilst, R. D. (2014). A unified map of Moho depth and Vp/Vs ratio of continental China by receiver function analysis, *Geophysical Journal International* **199**(3): 1910–1918.
URL: *https://doi.org/10.1093/gji/ggu365*

Hess, H. H. (1964). Seismic anisotropy of the uppermost mantle under oceans, *Nature* **203**(4945): 629–631.
URL: *https://doi.org/10.1038/203629a0*

Huang, W., van Hinsbergen, D. J. J., Lippert, P. C., Guo, Z. and Dupont-Nivet, G. (2015). Paleomagnetic tests of tectonic reconstructions of the india-asia collision zone, *Geophysical Research Letters* **42**(8): 2642–2649.
URL: *https://agupubs.onlinelibrary.wiley.com/doi/abs/10.1002/2015GL063749*

Jolivet, L., Faccenna, C., Becker, T., Tesauro, M., Sternai, P. and Bouilhol, P. (2018). Mantle flow and deforming continents: From india-asia convergence to pacific subduction, *Tectonics* **37**(9): 2887–2914.
URL: *https://agupubs.onlinelibrary.wiley.com/doi/abs/10.1029/2018TC005036*

Jolivet, L., Tamaki, K. and Fournier, M. (1994). Japan sea, opening history and mechanism: A synthesis, *Journal of Geophysical Research: Solid Earth* **99**(B11): 22237–22259.

Kennett, B. L. N. and Fichtner, A. (2020). *Exploiting Seismic Waveforms: Correlation, Heterogeneity and Inversion*, Cambridge University Press.

Laske, G., Masters, G., Ma, Z. and Pasyanos, M. (2013). Update on crust1. 0—a 1-degree global model of earth's crust, *Geophysical research abstracts*, Vol. 15, EGU General Assembly Vienna, Austria, p. 2658.

Li, Y., Wang, C., Dai, J., Xu, G., Hou, Y. and Li, X. (2015). Propagation of the deformation and growth of the tibetan–himalayan orogen: A review, *Earth-Science Reviews* **143**: 36–61.
URL: *https://www.sciencedirect.com/science/article/pii/S0012825215000100*

Ma, J., Bunge, H.-P., Thrastarson, S., Fichtner, A., Herwaarden, D.-P. v., Tian, Y., Chang, S.-J. and Liu, T. (2022). Seismic full-waveform inversion of the crust-mantle structure beneath china and adjacent regions, *Journal of Geophysical Research: Solid Earth* **127**(9): e2022JB024957. e2022JB024957 2022JB024957.
URL: *https://agupubs.onlinelibrary.wiley.com/doi/abs/10.1029/2022JB024957*

Ma, J., Tian, Y., Zhao, D., Liu, C. and Liu, T. (2019). Mantle dynamics of western pacific and east asia: New insights from p wave anisotropic tomography, *Geochemistry, Geophysics, Geosystems* **20**(7): 3628–3658.
URL: *https://agupubs.onlinelibrary.wiley.com/doi/abs/10.1029/2019GC008373*

Maurya, S., Montagner, J.-P., Kumar, M. R., Stutzmann, E., Kiselev, S., Burgos, G., Rao, N. P. and Srinagesh, D. (2016). Imaging the lithospheric structure beneath the indian continent, *Journal of Geophysical Research: Solid Earth* **121**(10): 7450–7468.
URL: *https://agupubs.onlinelibrary.wiley.com/doi/abs/10.1002/2016JB012948*

Molnar, P., England, P. and Martinod, J. (1993). Mantle dynamics, uplift of the tibetan plateau, and the indian monsoon, *Reviews of Geophysics* **31**(4): 357–396.

Molnar, P. and Tapponnier, P. (1975). Cenozoic tectonics of asia: Effects of a continental collision: Features of recent continental tectonics in asia can be interpreted as results of the india-eurasia collision, *science* **189**(4201): 419–426.

Montagner, J.-P. and Tanimoto, T. (1991). Global upper mantle tomography of seismic velocities and anisotropies, *Journal of Geophysical Research: Solid Earth* **96**(B12): 20337–20351.
URL: *https://doi.org/10.1029/91jb01890*

Müller, R. D., Seton, M., Zahirovic, S., Williams, S. E., Matthews, K. J., Wright, N. M., Shephard, G. E., Maloney, K. T., Barnett-Moore, N., Hosseinpour, M., Bower, D. J. and Cannon, J. (2016). Ocean basin evolution and global-scale plate reorganization events since pangea breakup, *Annual Review of Earth and Planetary Sciences* **44**(1): 107–138.
URL: *https://doi.org/10.1146/annurev-earth-060115-012211*

Nicolas, A. and Christensen, N. I. (1987). *Formation of Anisotropy in Upper Mantle Peridotites - A Review*, American Geophysical Union (AGU), pp. 111–123.
URL: *https://agupubs.onlinelibrary.wiley.com/doi/abs/10.1029/GD016p0111*

Northrup, C., Royden, L. and Burchfiel, B. (1995). Motion of the pacific plate relative to eurasia and its potential relation to cenozoic extension along the eastern margin of eurasia, *Geology* **23**(8): 719–722.

Panning, M. and Romanowicz, B. (2006). A three-dimensional radially anisotropic model of shear velocity in the whole mantle, *Geophysical Journal International* **167**(1): 361–379.
URL: *https://doi.org/10.1111/j.1365-246x.2006.03100.x*

Priestley, K. and MKenzie, D. (2006). The thermal structure of the lithosphere from shear wave velocities, *Earth and Planetary Science Letters* **244**(1): 285–301.
URL: *https://www.sciencedirect.com/science/article/pii/S0012821X06000331*

Reilinger, R., McClusky, S., Vernant, P., Lawrence, S., Ergintav, S., Cakmak, R., Ozener, H., Kadirov, F., Guliev, I., Stepanyan, R., Nadariya, M., Hahubia, G., Mahmoud, S., Sakr, K., ArRajehi, A., Paradissis, D., Al-Aydrus, A., Prilepin, M., Guseva, T., Evren, E., Dmitrotsa, A., Filikov, S. V., Gomez, F., Al-Ghazzi, R. and Karam, G. (2006). Gps constraints on continental deformation in the africa-arabia-eurasia continental collision zone and implications for the dynamics of plate interactions, *Journal of Geophysical Research: Solid Earth* **111**(B5).
URL: *https://agupubs.onlinelibrary.wiley.com/doi/abs/10.1029/2005JB004051*

Ren, J., Niu, B., Wang, J., Jin, X., Zhao, L. and Liu, R. (2013). Advances in research of asian geology—a summary of 1:5m international geological map of asia project, *Journal of Asian Earth Sciences* **72**: 3–11. Geological Evolution of Asia.
URL: *https://www.sciencedirect.com/science/article/pii/S1367912013000928*

Ribe, N. M. (1989). Seismic anisotropy and mantle flow, *Journal of Geophysical Research: Solid Earth* **94**(B4): 4213–4223.
URL: *https://agupubs.onlinelibrary.wiley.com/doi/abs/10.1029/JB094iB04p04213*

Royden, L. H., Burchfiel, B. C. and van der Hilst, R. D. (2008). The geological evolution of the tibetan plateau, *science* **321**(5892): 1054–1058.

Savage, M. K. (1999). Seismic anisotropy and mantle deformation: What have we learned from shear wave splitting?, *Reviews of Geophysics* **37**(1): 65–106.
URL: *https://doi.org/10.1029/98rg02075*

Schellart, W. P. and Lister, G. (2005). The role of the east asian active margin in widespread extensional and strike-slip deformation in east asia, *Journal of the Geological Society* **162**(6): 959–972.

Seton, M., Müller, R., Zahirovic, S., Gaina, C., Torsvik, T., Shephard, G., Talsma, A., Gurnis, M., Turner, M., Maus, S. and Chandler, M. (2012). Global continental and ocean basin reconstructions since 200ma, *Earth-Science Reviews* **113**(3): 212–270.
URL: *https://www.sciencedirect.com/science/article/pii/S0012825212000311*

Tapponnier, P. and Molnar, P. (1979). Active faulting and cenozoic tectonics of the tien shan, mongolia, and baykal regions, *Journal of Geophysical Research: Solid Earth* **84**(B7): 3425–3459.

Tapponnier, P., Peltzer, G., Le Dain, A. Y., Armijo, R. and Cobbold, P. (1982). Propagating extrusion tectonics in Asia: New insights from simple experiments with plasticine, *Geology* **10**(12): 611–616.
URL: *https://doi.org/10.1130/0091-7613(1982)10<611:PETIAN>2.0.CO;2*

Tapponnier, P., Xu, Z., Roger, F., Meyer, B., Arnaud, N., Wittlinger, G. and Jingsui, Y. (2001). Oblique stepwise rise and growth of the tibet plateau, *science* **294**(5547): 1671–1677.

Tromp, J. (2020). Seismic wavefield imaging of earth's interior across scales, *Nature Reviews Earth & Environment* **1**(1): 40–53.

Wang, M. and Shen, Z.-K. (2020). Present-day crustal deformation of continental china derived from gps and its tectonic implications, *Journal of Geophysical Research: Solid Earth* **125**(2): e2019JB018774. e2019JB018774 2019JB018774.
URL: *https://agupubs.onlinelibrary.wiley.com/doi/abs/10.1029/2019JB018774*

Wehner, D., Blom, N., Rawlinson, N., Daryono, Böhm, C., Miller, M. S., Supendi, P. and Widiyantoro, S. (2022). Sassy21: A 3-d seismic structural model of the lithosphere and underlying mantle beneath southeast asia from multi-scale adjoint waveform tomography, *Journal of Geophysical Research: Solid Earth* **127**(3): e2021JB022930. e2021JB022930 2021JB022930.
URL: *https://agupubs.onlinelibrary.wiley.com/doi/abs/10.1029/2021JB022930*

Wu, J., Suppe, J., Lu, R. and Kanda, R. (2016). Philippine sea and east asian plate tectonics since 52 ma constrained by new subducted slab reconstruction methods, *Journal of Geophysical Research: Solid Earth* **121**(6): 4670–4741.
URL: *https://doi.org/10.1002/2016jb012923*

Yang, J.-H., Xu, L., Sun, J.-F., Zeng, Q., Zhao, Y.-N., Wang, H. and Zhu, Y.-S. (2021). Geodynamics of decratonization and related magmatism and mineralization in the north china craton, *Science China Earth Sciences* **64**(9): 1409–1427.

Yin, A. (2000). Mode of cenozoic east-west extension in tibet suggesting a common origin of rifts in asia during the indo-asian collision, *Journal of Geophysical Research: Solid Earth* **105**(B9): 21745–21759.

Yin, A. (2006). Cenozoic tectonic evolution of the himalayan orogen as constrained by along-strike variation of structural geometry, exhumation history, and foreland sedimentation, *Earth-Science Reviews* **76**(1-2): 1–131.

Yin, A. (2010). Cenozoic tectonic evolution of asia: A preliminary synthesis, *Tectonophysics* **488**(1): 293–325. Extensional Tectonics in the Basin and Range, the Aegean, and Western Anatolia.
URL: *https://www.sciencedirect.com/science/article/pii/S0040195109003217*

Yin, A. and Harrison, T. M. (2000). Geologic evolution of the himalayan-tibetan orogen, *Annual review of earth and planetary sciences* **28**(1): 211–280.

Zhang, K.-J. (2012). Destruction of the north china craton: Lithosphere folding-induced removal of lithospheric mantle?, *Journal of Geodynamics* **53**: 8–17.
URL: *https://doi.org/10.1016/j.jog.2011.07.005*

Zhang, P., Deng, Q., Zhang, G., Ma, J., Gan, W., Min, W., Mao, F. and Wang, Q. (2003). Active tectonic blocks and strong earthquakes in the continent of china, *Science in China Series D: Earth Sciences* **46**(2): 13–24.

Zhang, S. and Karato, S.-i. (1995). Lattice preferred orientation of olivine aggregates deformed in simple shear, *Nature* **375**(6534): 774–777.

Zhao, D. (2021). Seismic imaging of northwest pacific and east asia: New insight into volcanism, seismogenesis and geodynamics, *Earth-Science Reviews* **214**: 103507.

Zheng, Y., Xu, Z., Zhao, Z. and Dai, L. (2018). Mesozoic mafic magmatism in north china: Implications for thinning and destruction of cratonic lithosphere, *Science China Earth Sciences* **61**(4): 353–385.

Chapter 4

Conclusion and Outlook

The physical properties of the Earth's interior can be indirectly detected through seismic waves excited by earthquakes. In this work, the state-of-the-art full-waveform inversion technique combined with ∼2 TB waveform dataset was used to construct the 3D reference seismic model of the Asian region (***SinoScope 1.0***) with the shortest period of 30 seconds, which required ∼10 million CPU hours. ***SinoScope 1.0*** not only confirms well-established features but also exhibits much sharper and more detailed shear wave velocity anomalies, which provides important new information on some fundamental problems of the earth sciences in Asia. The results of these efforts have the potential to enhance our understanding of the subsurface behavior of cold subducting slabs and hot mantle flows and their relation to the tectonic evolution of the overriding plates (intraplate seismogenesis and volcanism, India-Eurasia collision, lithospheric deformation and mountain building, etc.).

While an accurate numerical scheme based on the spectral-element method was employed to calculate forward and adjoint wavefields at the expense of huge computational costs, there are still a number of physical effects that were not accounted for in this work, such as the surface topography, ocean load, rotation, self-gravitation, and explicitly meshed internal discontinuities. Some could be safely negligible within the chosen period range (30-120 s). However, in future work, it is undoubtedly important to take the full physics of seismic wave propagation simulations properly into account in seismic imaging to avoid any approximations or corrections. Full-waveform inversion that quantifies the differences between synthetic and observed waveforms classically suffers from the cycle skipping problem at high frequencies. The recent proposed graph-space-optimal-transport misfit can efficiently measure the discrepancy between simulated and observed signals, which largely eliminates cycle skipping, alleviates the common need for either a good initial model and/or low-frequency data, and accelerate the iterative inversion to converge to a meaningful result. It probably offers the promise of marching into the higher frequency (∼1 Hz) to reveal the small-scale structure. In addition, the rapidly growing volume of seismological waveform data released by various international seismic networks and advances in computational power and numerical optimization routines have enabled the possibility of tackling finer-scale and more complex tomography problems in the coming future. This

will undoubtedly drive more work to produce the second-generation full-waveform tomographic model (***SinoScope 2.0***), especially motivated by the deployment of a large-scale broadband seismic array (ChinArray), which densely covers the entire mainland China and is spaced ∼35–40 km apart on average. Evident future work needs to assimilate the quick-growing earthquake database recorded by a few seismic networks not available now.

Tomographic images represent a snapshot of the convecting mantle. They hold key constraints on the history of mantle flow. Now it is possible to unlock this history through a new field of geodynamic modeling, where inverse theory allows one to retrodict past mantle states. Although expensive in computational terms, the geodynamic inverse approach in combination with detailed tomographic images allows one to link the surface tectonic evolution explicitly to deep earth processes in the mantle beneath. This coming future work, which connects seismic and geodynamic earth models, can help to advance our understanding of mantle rheology and buoyancy by linking geophysical and geologic constraints on present and past states of the Earth consistently through geodynamic mantle flow evolutions, yielding powerful synergies across different Earth sciences disciplines.

Acknowledgments

Rome was not built in a day, nor could it be accomplished by anyone alone. It would not have been possible to complete this thesis without the generous assistance and support of many people during the last four and half years I spent in München. First and foremost, I would like to express my deepest gratitude to my two excellent supervisors, Prof. Hans-Peter Bunge and Prof. Andreas Fichtner, for giving me the opportunity to work on such an interesting and challenging topic and for their supervision and encouragement all the way through. Peter is a geodynamicist with a unique talent in both theories and observations, who not only opened in front of me a vast world of global geodynamic simulations and innovative methods to explore the nature and evolution of the Earth through the dynamic flow models but also provided me with the ideal balance of freedom and guidance to pursue the ability to do research independently. Likewise, I heartily thank Andreas for your guidance in the world of seismic full-waveform inversion. The more I work with you, the more I realize you are such a talented, knowledgeable, and easy-going person. These four years of valuable experience have shaped and continue to shape the course of my academic career. If I can make any contribution to science in the future, it will undoubtedly come from the teaching and help you have given me today!

My thanks for the fruitful and insightful collaboration go to Sölvi Thrastarson, Christian Boehm, Lion Krischer, Dirk-Philip van Herwaarden, and many members of the Seismology and Wave Physics group, which finally gave birth to ***SinoScope 1.0***. I especially appreciate the impressively fast assistance from Sölvi when necessary, and daily e-mails were common (Although we have said countless cheers, we have not found the proper opportunity to drink Beer or Baijiu). Looking forward to working together again in the coming future to construct a more amazing new model ***SinoScope 2.0***.

Furthermore, I would like to thank all former and current members of our geodynamics group: Ayo, Berta, Eugenio, Ingo, Nicolas, Roman, and many others (Ayo, I cannot remember how much happines and laughs you brought into my daily life in the Room C417, München, and Zürich during the past five years ...). It was very interesting to be exposed to a wide range of research topics in our group meetings, and see the progress of each group member during these meetings. Many thousand thanks also to Jens for building an excellent computing infrastructure at the Institute of Geophysics at LMU München, without which it is impossible for me to perform one single numerical simulation. Most importantly, Jens, so many thanks for your delicious coffee (Honestly, coffee is not my flavor but quite like traditional Chinese medicine).

And, in the tradition of always keeping the sweetest heart of mooncake for last, I would like to express my deepest thanks to my beloved wife, Dr. Tingting Liu, who sacrificed a lot to take care of my life and academic career in the past seven years and always unconditionally supports me in literally everything I do. Without your continuous assistance and accompanies, I cannot move or promote further one step in this world. What I can do is make the world around you more beautiful and energetic ...

I deeply love my motherland with my pure heart, and I am willing to put my life into her long and great history, building greater times!

My doctoral work was supported by the China Scholarship Council (CSC, Grant Numbers: CSC201806170051). I also gratefully acknowledge the Gauss Center for Supercomputing e.V. (www.gauss-centre.eu) for funding this project by providing computing time on the GCS Supercomputer SuperMUC-NG at Leibniz Supercomputing Center (www.lrz.de) and support from the Swiss National Supercomputing Center (CSCS) in the form of computing time grants s1040.